



**AFRL-RX-WP-TR-2016-0027**

**INSTITUTE FOR SCIENCE AND ENGINEERING  
SIMULATION (ISES)**

**Rajarshi Banerjee, Alan Needleman, Thomas W. Scharf, and Angela Wilson**

**University of North Texas**

**18 DECEMBER 2015  
Final Report**

**Distribution Statement A. Approved for public release; distribution unlimited.**

*See additional restrictions described on inside pages*

**STINFO COPY**

**AIR FORCE RESEARCH LABORATORY  
MATERIALS AND MANUFACTURING DIRECTORATE  
WRIGHT-PATTERSON AIR FORCE BASE, OH 45433-7750  
AIR FORCE MATERIEL COMMAND  
UNITED STATES AIR FORCE**

## NOTICE AND SIGNATURE PAGE

Using Government drawings, specifications, or other data included in this document for any purpose other than Government procurement does not in any way obligate the U.S. Government. The fact that the Government formulated or supplied the drawings, specifications, or other data does not license the holder or any other person or corporation; or convey any rights or permission to manufacture, use, or sell any patented invention that may relate to them.

This report was cleared for public release by the USAF 88th Air Base Wing (88 ABW) Public Affairs Office (PAO) and is available to the general public, including foreign nationals.

Copies may be obtained from the Defense Technical Information Center (DTIC) (<http://www.dtic.mil>).

AFRL-RX-WP-TR-2016-0027 HAS BEEN REVIEWED AND IS APPROVED FOR PUBLICATION IN ACCORDANCE WITH ASSIGNED DISTRIBUTION STATEMENT.

---

//Signature//

MICHEAL E. BURBA, Project Engineer  
Metals Branch  
Structural Materials Division

---

//Signature//

DANIEL EVANS, Chief  
Metals Branch  
Structural Materials Division

---

//Signature//

ROBERT T. MARSHALL, Deputy Chief  
Structural Materials Division  
Materials and Manufacturing Directorate

This report is published in the interest of scientific and technical information exchange, and its publication does not constitute the Government's approval or disapproval of its ideas or findings.

# REPORT DOCUMENTATION PAGE

*Form Approved  
OMB No. 0704-0188*

The public reporting burden for this collection of information is estimated to average 1 hour per response, including the time for reviewing instructions, searching existing data sources, gathering and maintaining the data needed, and completing and reviewing the collection of information. Send comments regarding this burden estimate or any other aspect of this collection of information, including suggestions for reducing this burden, to Department of Defense, Washington Headquarters Services, Directorate for Information Operations and Reports (0704-0188), 1215 Jefferson Davis Highway, Suite 1204, Arlington, VA 22202-4302. Respondents should be aware that notwithstanding any other provision of law, no person shall be subject to any penalty for failing to comply with a collection of information if it does not display a currently valid OMB control number. **PLEASE DO NOT RETURN YOUR FORM TO THE ABOVE ADDRESS.**

<b>1. REPORT DATE (DD-MM-YY)</b> 18 December 2015			<b>2. REPORT TYPE</b> Final		<b>3. DATES COVERED (From - To)</b> 18 September 2008 – 18 November 2015	
<b>4. TITLE AND SUBTITLE</b>  INSTITUTE FOR SCIENCE AND ENGINEERING SIMULATION (ISES)			<b>5a. CONTRACT NUMBER</b> FA8650-08-C-5226			
			<b>5b. GRANT NUMBER</b>			
			<b>5c. PROGRAM ELEMENT NUMBER</b> 62102F			
<b>6. AUTHOR(S)</b>  Rajarshi Banerjee, Alan Needleman, Thomas W. Scharf, and Angela Wilson			<b>5d. PROJECT NUMBER</b> 4349			
			<b>5e. TASK NUMBER</b>			
			<b>5f. WORK UNIT NUMBER</b> X06B			
<b>7. PERFORMING ORGANIZATION NAME(S) AND ADDRESS(ES)</b>  University of North Texas 1155 Union Circle #305310 Denton, TX 76203-5017			<b>8. PERFORMING ORGANIZATION REPORT NUMBER</b>			
<b>9. SPONSORING/MONITORING AGENCY NAME(S) AND ADDRESS(ES)</b>  Air Force Research Laboratory Materials and Manufacturing Directorate Wright-Patterson Air Force Base, OH 45433-7750 Air Force Materiel Command United States Air Force			<b>10. SPONSORING/MONITORING AGENCY ACRONYM(S)</b> AFRL/RXCM			
			<b>11. SPONSORING/MONITORING AGENCY REPORT NUMBER(S)</b> AFRL-RX-WP-TR-2016-0027			
<b>12. DISTRIBUTION/AVAILABILITY STATEMENT</b> Distribution Statement A. Approved for public release; distribution unlimited.						
<b>13. SUPPLEMENTARY NOTES</b> PA Case Number: 88ABW-2016-1750; Clearance Date: 05 April 2016. This report contains color.						
<b>14. ABSTRACT (Maximum 200 words)</b> The Institute for Science and Engineering Simulation (ISES), at the University of North Texas, has developed and applied novel materials characterization, modeling, and simulation tools to aid in the future inspection, repair and design of improved materials and processes for aerospace applications. Specifically, the program has aided in establishing the fundamental understanding required to support safety engineers in their ability to upgrade and maintain the Air Force's aging fleet by predicting material performance and structural integrity using principles based on mechanics and deformation of materials. This multifunctionality necessitates a strong coupling between structural performance and other functionalities such as electrical, magnetic, optical, thermal, biological, chemical, and so forth. Structural integrity includes durability, survivability, reliability, and maintainability. ISES thus focused on developing new design and performance criteria involving material science, mechanics, physics, and chemistry to model and characterize the processing and performance of multifunctional materials and microsystems at multiple scales from atoms to the continuum. This large-scale multi-year project focused on three principal thrust areas, developed based on the interests of AFRL. The major accomplishments of each of these tasks have been described in detail in this report.						
<b>15. SUBJECT TERMS</b> metallic alloys, structural hybrid materials, microstructure-property relationships, characterization, modeling						
<b>16. SECURITY CLASSIFICATION OF:</b>		<b>17. LIMITATION OF ABSTRACT:</b>		<b>18. NUMBER OF PAGES</b>	<b>19a. NAME OF RESPONSIBLE PERSON (Monitor)</b> Micheal E. Burba	
<b>a. REPORT</b> Unclassified	<b>b. ABSTRACT</b> Unclassified	<b>c. THIS PAGE</b> Unclassified	SAR	118	<b>19b. TELEPHONE NUMBER (Include Area Code)</b> (937) 255-9795	

## Table of Contents

<u>Section</u>	<u>Page</u>
List of Figures .....	iv
List of Tables .....	vii
1. Summary .....	1
2. Introduction .....	7
3. Methods, Assumptions, and Procedures .....	9
4. Results and Discussion .....	10
4.1. Thrust Area I: Lifetime prediction of turbine blades.....	10
4.2. Thrust Area II: Influences of Microstructure and Chemistry on Mechanical Properties of Aerospace Material.....	12
4.2.1.Task A: Structure and chemistry across $\gamma/\gamma'$ interfaces in nickel-based superalloys.....	12
4.2.2. Task B: Three-dimensional characterization of nanoscale $\gamma'$ precipitates in nickel-based superalloys.....	15
4.2.3. Task C: Lattice parameters of $\gamma$ and $\gamma'$ phases and site occupancies in ordered $\gamma'$ phase.....	19
4.2.3.1 <i>Site Preference Energies for Co</i> .....	20
4.2.3.2. <i>Interaction between Co-Co atoms</i> .....	22
4.2.3.3. <i>Interaction between Cr-Cr atoms</i> .....	23
4.2.3.4. <i>Interaction between Cr-Co atoms</i> .....	24
4.2.4.Task D: Mechanisms of refined scale intra-granular precipitation in titanium alloys .....	25
4.2.4.1. <i>Non-classical Homogeneous Precipitation Mediated by Compositional Fluctuations in Titanium Alloys</i> .....	25
4.2.4.1.1. <i>Determination of the characteristics of the phase transformation</i> .....	25
4.2.4.1.2. <i>Temperature dependence of the transformation</i> .....	25
4.2.4.1.3. <i>Mechanism of intragranular <math>\gamma</math> precipitation in Ti-5553 during isothermal annealing</i> .....	27
4.2.4.2. <i>Pseudospinodal Mechanism for Fine <math>\alpha/\beta</math> Microstructures in <math>\beta</math>-Ti alloys</i> .....	31
4.2.4.2.1 <i>Model Development</i> .....	32
4.2.4.2.2. <i>Free energy model</i> .....	32
4.2.4.2.3. <i>Kinetic equations</i> .....	33
4.2.4.2.4. <i>Nucleation model</i> .....	33
4.2.4.2.5. <i>Results and Discussion</i> .....	34
4.2.4.2.6. <i>Conclusion</i> .....	38
4.2.5. Task E: Evaluation of the oxidation behavior of titanium alloys .....	38
4.2.5.1. <i>Influence of oxygen ingress on fine scale precipitation of <math>\alpha</math>-Ti during oxidation of Beta21S, <math>\beta</math>-Ti alloy.....</i>	38
4.2.5.1.1. <i>Results and Discussion</i> .....	39
4.2.5.1.2. <i>Conclusions</i> .....	42
4.2.6.Task F: Development of models of nucleation associated with solid-solid phase transformations in titanium and nickel base alloys .....	43
4.2.6.1. <i>Nucleation of second phases in Titanium Alloys</i> .....	43
4.2.6.1.1. <i>Results and Discussion</i> .....	43
4.2.6.2. <i>Nucleation of <math>\gamma'</math> in Nickel Base Alloys</i> .....	46
4.2.6.2.1. <i>Precipitate size and morphology</i> .....	47

4.2.6.2.2. <i>Overall size distribution</i> .....	48
4.2.6.2.3. <i>Compositional analysis of different generations of <math>\gamma'</math></i> .....	49
4.2.6.2.4. <i>Growth influenced Morphology and Chemical changes</i> .....	50
4.2.6.2.5. <i>Mechanism of multiple bursts of nucleation</i> .....	51
4.2.7. Task G: <i>Growth and coarsening of L12 precipitates in new generation Co based alloy</i> .....	54
4.2.7.1. <i>Water quenched condition prior to annealing</i> .....	54
4.2.7.2. <i>Morphological changes during isothermal annealing</i> .....	55
4.2.7.3. <i>Compositional changes across <math>\gamma/\gamma'</math> interface during isothermal annealing</i> .....	55
4.2.7.4. <i>Interfacial energy from the Cahn-Hilliard approximation</i> .....	57
4.2.7.5. <i>Coarsening rate constants based on LSW theory</i> .....	58
4.2.7.6. <i>Determination of the activation energy</i> .....	60
4.2.7.7. <i>Determination of <math>\gamma/\gamma'</math> interfacial energy and the gradient energy coefficient</i> .....	60
4.2.7.8. <i>Inter-precipitate distances and coalescence of <math>\gamma'</math> precipitates</i> .....	61
4.2.7.9. <i>Discussion</i> .....	62
4.2.8. Task H: <i>Mechanism of Nano-scale precipitation in soft magnetic alloys</i> .....	64
4.2.8.1. <i>Results</i> .....	64
4.2.8.2. <i>Discussion</i> .....	68
4.3. Thrust Area III: <i>Three-dimensional (3D) Functionally-graded Hybrid Materials for Aerospace Structural Applications</i> .....	70
4.3.1. Task A: <i>Metal-Ceramic Hybrids</i> .....	70
4.3.1.1. <i>Nickel-TiC-Graphite Hybrids</i> .....	70
4.3.1.1.1. <i>Laser Engineered Net Shaping (LENS<sup>TM</sup>)</i> .....	70
4.3.1.1.2. <i>Dual Beam FIB-SEM Serial Sectioning Methodology</i> .....	71
4.3.1.1.3. <i>Three Dimensional (3D) Reconstruction</i> .....	71
4.3.1.1.4. <i>Microhardness and Tribological Properties</i> .....	72
4.3.1.1.5. <i>Results</i> .....	72
4.3.1.1.6. <i>Conclusions</i> .....	75
4.3.2. Task B: <i>Ceramic-Ceramic Hybrids</i> .....	76
4.3.2.1. <i>Ceramic coating infiltrated Carbon-Carbon Composites</i> .....	76
4.3.2.1.2. <i>Theoretical and experimental investigations on the mechanism of carbothermal reduction of zirconia</i> .....	78
4.3.2.2. <i>Bulk diffusion of C in YSZ pellets</i> .....	80
4.3.2.2.1. <i>Discussion on mechanism of carbothermal reduction of zirconia</i> .....	81
4.3.2.2.2 <i>X-ray absorption spectroscopy (XAS) studies on the carbothermal reduction reaction products of 3 mol% yttria stabilized zirconia</i> .....	82
4.3.3. Task C: <i>Metal-Carbon Nanotube Hybrids</i> .....	83
4.3.3.1. <i>Nickel-Carbon Nanotube (CNT) hybrid materials</i> .....	83
4.3.3.1.1. <i>Microstructure of CNT/Ni composites</i> .....	83
4.3.3.1.2. <i>X-ray diffraction analysis</i> .....	84
4.3.3.1.3. <i>Micro Raman spectroscopy studies</i> .....	84
4.3.3.1.4. <i>Microhardness and Tensile behavior of CNT/Ni composites</i> .....	85
4.3.3.1.5. <i>Summary and Conclusions</i> .....	87
4.3.3.2. <i>Nickel-Graphite Nanoplatelet Hybrid Materials</i> .....	87
4.3.3.2.1. <i>Scanning Electron Microscopy (SEM) Analysis of GNP/Ni nanocomposites</i> .....	88
4.3.3.2.2. <i>X-ray Diffraction (XRD) Analysis of GNP/Ni nanocomposites</i> .....	89
4.3.3.2.3. <i>Micro-Raman Spectroscopy Analysis of GNP/Ni nanocomposites</i> .....	89

<i>4.3.3.2.4. Tensile Properties of GNP/Ni nanocomposites .....</i>	90
<i>4.3.3.2.5. Fractography Analysis of GNP/Ni nanocomposites .....</i>	93
<i>4.3.3.2.6. Transmission Electron Microscopy (TEM) Analysis of GNP/Ni nanocomposites .....</i>	93
<i>4.3.3.2.7. Summary and Conclusions.....</i>	94
5.Conclusion .....	95
6.References.....	100
LIST OF ACRONYMS, ABBREVIATIONS, AND SYMBOLS .....	105

## List of Figures

<u>Figure</u>	<u>Page</u>
1. (a) Al 10% (red) and Co 19% (blue) isosurfaces depicting morphology of the $\gamma'$ precipitate used in 3DAP analysis; the red area is indicative of the primary $\gamma'$ precipitate, (b) and (c) higher magnification views showing the stacking of alternate (002) Al planes within the $\gamma'$ , (d) Proximity Histogram depicting the compositional transition across the $\gamma$ / $\gamma'$ interface; the area used in the analysis is indicated by the arrow in the inset.....	13
2. (a) Dark field image of Ni-8Al-8Cr at% sample after isothermal aging at 600 °C for 256 hours, post continuous cooling b) SADP corresponding to the dark-field image c) 3-D reconstruction of 10 at% Al isoconcentration surface delineating d) proximity histogram for Al and Cr corresponding to 10 at% Al isosurface shown in c). ....	17
3. Low magnification SEM backscattered images of similar heat treatment at (a) 600°C and (b) 650°C with the annealing time being 30 minutes where similar high density of intragranular $\alpha$ precipitation is observed.....	26
4. Schematic Gibbs free energy versus composition (G-X) plots for the $\beta$ and $\alpha$ phases in case of the present study where at 600 °C the $c_0(T)$ point is close to the nominal alloy composition ( $X_0$ ). The red arrow indicators the range of possible compositional fluctuations. The green arrow indicates that, for fluctuations that cause the local composition to be less than the $c_0(T)$ point, transformation from the $\beta$ phase directly to the $\alpha$ phase would be favorable.....	28
5. Calculated $\alpha$ precipitates morphology with elastic energy at fixed temperature with different average composition $\Delta c=0.0, 0.02, 0.03$ ( $\Delta c = c - c_0$ ). (a) – (c) describe the composition field with different $\Delta c$ , black color describes the low composition. (a') – (c') describe the structure field with different $\Delta c$ , red, green and blue colors describe the three variants of $\alpha$ precipitate, dark blue color describes the $\beta$ phase. ....	37
6. 3D surface plots mapping concentration distributions for a) Oxygen and b) Aluminum across the oxide–alloy interface using Electron probe micro-analyzer. ....	39
7. (a) Schematic arrangement of atoms as seen from the $<110>\beta$ zone axis, corresponding to the $\beta$ and fully collapsed $\omega$ motifs. Small arrows show the shifts of atoms along $<111>\beta$ directions. (b) HRTEM image recorded along the $<011>\beta$ zone axis, in a 748 K/30 min aged Ti-9 at.% Mo sample, showing the collapse in atomic columns corresponding to the well-developed $\omega$ phase. (c) Proximity histogram using Ti = 93 at. % isosurface that shows substantial compositional partitioning between the $\beta$ and $\omega$ phases. The inset shows the corresponding 3DAP reconstruction of the Ti-rich regions.....	44

8. Nudged elastic band (NEB) results plotted for 24 atom supercell systems with 0at:%, 8.33at:%, and 16.66at:% Mo in Ti. E is relative energy of the system along the minimum energy path with $\beta$ phase taken as reference. On the x-axis we have average coordinate of the collapsing (111) planes normalized by their inter-planar spacing. ....	45
9. (a)-(c) Schematic illustrations of how multiple $\gamma'$ generations can form during slow cooling of Rene 88 DT alloy.....	52
10. Schematic illustrating the effect of cooling rate on the formation of different gamma prime generations in Rene 88 DT alloy. ....	53
11. Proxigrams corresponding to 9 at% W shows $\gamma/\gamma'$ interface with partitioning of Al and W in samples subjected to varying isothermal annealing periods at 800°C along with APT reconstructions as insets where 9 at % W isosurface (red) delineates $\gamma'$ precipitates.....	56
12. APT of Fe-Si-B-Cu-Nb after annealing at 550C for 15 minutes. (a) shows the APT reconstruction of the FINEMET alloy after this annealing and shows the higher number density of nucleated Fe <sub>3</sub> Si crystals as compared after 10 minutes. (b) and (c) shows clear examples of side nucleation of Fe <sub>3</sub> Si from Cu clusters supporting Hono's model. (d) shows a proxigram of the Fe <sub>3</sub> Si interface with the amorphous matrix and reveals a clear Nb pileup at the interface.....	66
13. (a) 3D reconstruction of Ni-10Ti-10C composites obtained from the 2D SEM image stack (b) Cropped version of 3D reconstructed volume of Ni-10Ti-10C showing primary and eutectic TiCs. ....	73
14. (a) Cross-sectional SEM and (b) corresponding EDS color map showing surface and subsurface atomic layer deposition (ALD) ZrO <sub>2</sub> coating infiltration of CCC. (c) Cross-sectional TEM image of 4 ALD ZnO/Al <sub>2</sub> O <sub>3</sub> /ZrO <sub>2</sub> trilayers (~220 nm overall thickness) showing excellent coating conformality/uniformity and infiltration (pore filling) of the CCC. The red rectangle shows the 4 trilayer sequence grown on the CCC with the brighter, white ~5 nm thick Al <sub>2</sub> O <sub>3</sub> layer serving as a useful marker to distinguish the trilayers. The dashed line represents the surface of the sample where the protective Pt was deposited.....	77
15. Low and high magnification cross-sectional TEM images of fretting wear surfaces and subsurfaces for (a+b) uncoated CCC, and (c+d) ALD coated ZnO/Al <sub>2</sub> O <sub>3</sub> /ZrO <sub>2</sub> trilayer showing mechanically mixed layers (MML) resulting from fretting wear contact. ....	78
16. Flowchart showing the methodology in XRD analysis of four pellets before and after carbothermal reduction heat treatment. Shrinkage seen in top half of MP2s and GPs is due to prior sintering of the YSZ pellet. The cloud shape represents powder formed from bottom halves as they decompose after heat treatment. Mole percentages determined by XRD Rietveld analysis are listed for ZrC formed on the top and bottom faces of MP, GP, MPs and GPs.....	79

17. Variation of carbon concentration as a function of diffusion distance (x) in YSZ at 1800 °C. Curves are plotted for various diffusion times of 1800, 3600 and 5400 seconds. Vertical dotted line shows maximum distance to which X-rays penetrated based on diffraction data acquired from bottom and top faces of MP, GP, MPs and GPs top halves. .....80

18. Raman spectra showing the D, G, and D' peaks from raw CNT, CNT/Ni ball milled powder, CNT/Ni Dry milled, and CNT/Ni molecular level mixed nanocomposites.....85

19. Micro-Raman spectra showing the D, G and D' peaks from raw GNP, ball milled Ni-GNP powder, and different content Ni-GNP nanocomposites..... 89

## List of Tables

<u>Table</u>	<u>Page</u>
1. Composition and interface width of $\gamma'$ .....	18
2. Site preference energies (eV) for Co substitution calculated from the standard defect formalism with different supercell sizes. .....	20
3. Site preference energies (eV) for Co substitution calculated from the anti-site formation based formalism with different supercell sizes. .....	21
4. Site preference energies (eV) for Co substitution calculated from the vacancy formation based formalism with different supercell sizes. .....	22
5. Equilibrium composition of $\gamma$ and $\gamma'$ measured from APT .....	57
6. Summary of observed mechanical properties .....	86
7. Microhardness, yield strength and elongation properties of pure nickel and GNP/Ni nanocomposites.....	91

## 1. Summary

The Institute for Science and Engineering Simulation (ISES) project was carried out primarily at the University of North Texas (UNT) in collaboration with the Air Force Research Laboratory (AFRL), the Ohio State University (OSU), and a few other collaborating institutions. This large-scale multi-year project focused on three principal thrust areas, developed based on the interests of AFRL. Under each of these thrust areas, multiple tasks were carried out and the major accomplishments of each of these tasks has been summarized below:

### Thrust Area I: Lifetime prediction of turbine blades

#### Task A: Effect Creep tests on Ni-based single-crystal superalloy

Creep tests on Ni-based single-crystal superalloy sheet specimens typically show greater creep strain rates and/or reduced strain or time to creep rupture for thinner specimens than predicted by current theories, which predict a size-independent creep strain rate and creep rupture strain. This size-dependent creep response is termed the thickness debit effect. To investigate the mechanism of the thickness debit effect, isothermal, constant nominal stress creep tests were performed on uncoated PWA1484 Ni-based single-crystal superalloy sheet specimens of thicknesses 3.18 and 0.51 mm under two test conditions: 760 °C/758 MPa and 982 °C/248 MPa. The specimens contained initial microvoids formed during the solidification and homogenization processes. The dependence of the creep response on specimen thickness differed under the two test conditions: at 760 °C/758 MPa there was a reduction in the creep strain and the time to rupture with decreasing section thickness, whereas at 982 °C/248 MPa a decreased thickness resulted in an increased creep rate even at low strain levels and a decreased time to rupture but with no systematic dependence of the creep strain to rupture on specimen thickness. For the specimens tested at 760 °C/758 MPa microscopic analyses revealed that the thick specimens exhibited a mixed failure mode of void growth and cleavage-like fracture while the predominant failure mode for the thin specimens was cleavage-like fracture. The creep specimens tested at 982 °C/248 MPa in air showed the development of surface oxides and a near surface precipitate-free zone. Finite-element analysis revealed that the presence of the alumina layer at the free surface imposes a constraint that locally increases the stress triaxiality and changes the value of the Lode parameter (a measure of the third stress invariant). The surface cracks formed in the oxide scale were arrested by further oxidation; for a thickness of 3.18 mm the failure mode was void nucleation, growth and coalescence, whereas for a thickness of 0.51 mm there was a mixed mode of ductile and cleavage-like fracture.

### Thrust Area II: Influences of Microstructure and Chemistry on Mechanical Properties of Aerospace Materials

#### Task A: Structure and chemistry across $\gamma/\gamma'$ interfaces in nickel-based superalloys

Through a combination of aberration-corrected high resolution scanning transmission electron microscopy (HRSTEM) and three-dimensional atom probe (3DAP) tomography, the true atomic scale structure and change in chemical composition across the complex order/disorder interface in a metallic alloy has been determined. The study reveals the presence of two interfacial widths, one corresponding to an order-disorder transition, and the other to the compositional transition across the interface, raising fundamental questions regarding the definition of the interfacial width in such systems.

### **Task B: Three-dimensional characterization of nanoscale $\gamma'$ precipitates in nickel-based superalloys**

The coupling of three characterization techniques spanning across multiple length scales, scanning electron microscopy (SEM), energy-filtered transmission electron microscopy (EFTEM), and 3D atom probe tomography (3DAP) techniques, has permitted characterizing and quantifying the multimodal size distribution of different generations of  $\gamma'$  precipitates formed during continuous cooling, followed by aging, in a commercial nickel-based superalloy, Rene' 88 DT. The size distributions of first, second, and third generation of  $\gamma'$  precipitates, in the same heat-treated condition, have been plotted as a function of equivalent diameter. The presence of tails in the precipitate size distribution suggests that the nucleation events occur over a range of temperatures within each nucleation burst, corresponding to each generation of  $\gamma'$  precipitates. The same techniques were applied to other nickel base alloys, including model Ni-Al-Cr and Ni-Al-Cr-Co alloys.

### **Task C: Lattice parameters of $\gamma$ and $\gamma'$ phases and site occupancies in ordered $\gamma'$ phase**

A methodology for determining the preferred site occupancy of various alloying elements within ordered  $\gamma'$  precipitates was developed and applied to the Rene88 alloy as well as model Ni-Al-Cr and Ni-Al-Cr-Co alloys. The method utilized atom probe tomography and X-ray diffraction techniques with controlled monochromated synchrotron beams to determine element positions. Samples were solutionized at 1423 K (1150 °C) for 30 minutes and cooled at 24 K/min with subsequent aging at 1033 K (760 °C). The synchrotron X-ray diffraction results indicate that niobium prefers to reside on the aluminum sublattice site of the  $\gamma'$  phase. Additionally, the results indicate that chromium prefers the nickel sublattice sites, while cobalt is likely to occupy both the aluminum and nickel sublattice sites. The X-ray results on the chromium occupancy disagree with atom probe results from the same alloy that indicate that chromium prefers the aluminum sublattice sites. These experimental results were also coupled with first-principle computations based on the density functional theory (DFT).

### **Task D: Mechanisms of refined scale intra-granular precipitation in titanium alloys**

Under this task, a novel intra-granular precipitation mechanism for  $\alpha$  in titanium alloys was discovered. The experimental evidence of homogeneous precipitation of fine scale  $\alpha$  precipitates within the  $\beta$  matrix of a titanium alloy occurs by a new, non-classical, mechanism involving compositional fluctuations, based on the pseudo-spinodal concept. This mechanism involves local compositional fluctuations of small amplitude which, when of a certain magnitude, can favor thermodynamically certain regions of the  $\beta$  matrix to transform congruently to the  $\alpha$  phase but with compositions far-from equilibrium. Subsequently, as measured experimentally using the tomographical atom probe, continuous diffusional partitioning between the parent  $\beta$  and product  $\alpha$  phases during isothermal annealing drives their compositions towards equilibrium. For a given alloy composition, the decomposition mechanism is strongly temperature dependent which would be expected for homogeneous precipitation via the compositional fluctuation-mediated mechanism but not necessarily for one based on classical nucleation theory. The applicability of this mechanism to phase transformations in general was noted.

### **Task E: Evaluation of the oxidation behavior of titanium alloys**

The formation of a surface oxide layer along with  $\alpha$  precipitation in the subsurface oxygen-enriched zone, during the oxidation of the TIMETAL 21S or  $\beta$ -21S alloy, was investigated using Scanning electron microscopy, Electron probe microanalysis, X-Ray diffraction, (Scanning) Transmission Electron Microscopy, 3D-Atom Probe studies and Nano-indentation. Immediately below the nanocrystalline oxide layer, a two-phase mixture consisting of nanoscale equiaxed  $\alpha$  grains and rutile grains is formed. With increasing depth, the  $\alpha$  morphology below the oxide layer varied from nanoscale equiaxed to lathlike, coupled with substantial changes in size-scale and nucleation density of  $\alpha$  precipitates. A distinct change in the lattice parameters of  $\alpha$  and  $\beta$  phases below the oxide layer and the overall micro hardness of the material is also noted. The role of oxygen ingress on the scale and morphology of  $\alpha$  precipitation has been discussed.

### **Task F: Development of models of nucleation associated with solid-solid phase transformations in titanium and nickel base alloys**

#### *Nucleation of second phases in Titanium Alloys*

This task led to direct experimental evidence of the formation of embryonic omega from competing compositional and structural instabilities arising in the body-centered cubic (*bcc*) lattice of titanium-molybdenum alloys during rapid quenching. The partial collapse of the {111} planes within phase-separated regions of the *bcc* phase, containing marginally lower amounts of molybdenum, forming embryos of the omega phase, has been conclusively shown by coupling aberration-corrected high-resolution scanning transmission electron microscopy with three-dimensional atom probe observations.

#### *Nucleation of $\gamma'$ in Nickel Base Alloys*

This task focused on developing a mechanistic understanding of the process of multiple nucleation bursts leading to the formation of multiple generations (or populations) of  $\gamma'$  precipitates with different size distributions, during the continuous cooling of a commercially used nickel base superalloy. This mechanistic understanding has been developed based on a number of critical experimental results; direct observation of the multiple nucleation bursts during *in situ* x-ray diffraction studies in the synchrotron, characterization of the size distributions associated with the different populations of  $\gamma'$  precipitates by coupling multiple imaging techniques at the appropriate length scale, and detailed compositional analysis of the  $\gamma'$  precipitates as well as the  $\gamma$  matrix using atom probe tomography. These analyses reveal that while local compositional equilibrium appears to have been achieved near the  $\gamma'/\gamma$  interface for the first-generation of precipitates, a non-equilibrium long range diffusion profile in the  $\gamma$  matrix is retained during the process of continuous cooling which is largely responsible for the subsequent nucleation bursts at larger undercooling (or lower temperatures) leading to the second and third generations of precipitates. Additionally, since these subsequent generations of precipitates are formed at larger undercoolings, they are typically finer in size scale, exhibit far-from equilibrium compositions, and also have very diffuse  $\gamma'/\gamma$  interfaces, indicating a non-classical precipitation mechanism associated with their formation.

A second thrust of this effort focused on precipitation under far-from equilibrium conditions (e.g. extremely rapid cooling). Under such conditions, the precipitation mechanism of ordered phases,

in metallic solid solutions, such as the  $\gamma'$  phase in Ni base alloys, has been a long-standing controversy due to the competing roles of chemical clustering (or phase separation) and chemical ordering. In the present study, this controversy has been resolved through the coupled use of aberration-corrected high-resolution scanning transmission electron microscopy and atom probe tomography. Thus, the experimental results, obtained at atomic resolution, can only be interpreted satisfactorily on the basis of phase separation via spinodal decomposition followed by chemical ordering.

#### **Task G: Growth and coarsening of L1<sub>2</sub> precipitates in new generation Co based alloy**

The expeditious development of novel cobalt base  $\gamma$ - $\gamma'$  alloys as possible next generation superalloys critically depends on achieving a comprehensive understanding of the coarsening kinetics of ordered  $\gamma'$  precipitates. This task focused on the coarsening of L1<sub>2</sub> ordered Co<sub>3</sub>(W,Al) precipitates in a model ternary Co-10Al-10W(at%) alloy during isothermal annealing at 800°C and 900°C. The experimentally determined temporal evolution of average size of the  $\gamma'$  precipitates suggests classical matrix diffusion limited LSW coarsening at both temperatures. The  $\gamma'$  coarsening rate constants have been determined using a modified coarsening rate equation for non-dilute solutions. Furthermore, using the Cahn-Hilliard formulation for interfacial energy, the  $\gamma/\gamma'$  interfacial energies at the respective annealing temperatures have been correlated to the concentration profile across the interface that has been experimentally determined using atom probe tomography (APT). The calculated interfacial energies are in comparable range with those observed in Nickel base superalloys. Additionally, this analysis has permitted, for the first time, the determination of the gradient energy coefficient for  $\gamma/\gamma'$  interfaces in Co-base alloys, a critical input for phase-field and other simulation models for microstructural evolution.

#### **Task H: Mechanism of Nano-scale precipitation in soft magnetic alloys**

The role of the solute elements, copper and niobium, on the different stages of de-vitrification or crystallization of two amorphous soft magnetic alloys, Fe<sub>73.5</sub>Si<sub>13.5</sub>B<sub>9</sub>Nb<sub>3</sub>Cu<sub>1</sub>, also referred to as FINEMET, and a Fe<sub>76.5</sub>Si<sub>13.5</sub>B<sub>9</sub>Cu<sub>1</sub> alloy, a model composition without Nb, has been investigated in detail by coupling atom probe tomography and transmission electron microscopy. The effects of copper clustering and niobium pile-up at the propagating interface between the  $\alpha$ -Fe<sub>3</sub>Si nanocrystals and the amorphous matrix, on the nucleation and growth kinetics has been addressed. The results demonstrate that while Cu clustering takes place in both alloys in the early stages, the added presence of Nb in FINEMET severely restricts the diffusivity of solute elements such as Cu, Si, and B. Therefore, the kinetics of solute partitioning and mobility of the nanocrystal/amorphous matrix interface is substantially slower in FINEMET as compared to the Fe<sub>76.5</sub>Si<sub>13.5</sub>B<sub>9</sub>Cu<sub>1</sub> alloy. Consequently, the presence of Nb limits the growth rate of the  $\alpha$ -Fe<sub>3</sub>Si nanocrystals in FINEMET and results in the activation of a larger number of nucleation sites, leading to a substantially more refined microstructure as compared to the Fe<sub>76.5</sub>Si<sub>13.5</sub>B<sub>9</sub>Cu<sub>1</sub> alloy.

## Thrust Area III: Three-dimensional (3D) Functionally-graded Hybrid Materials for Aerospace Structural Applications

### Task A: Metal-Ceramic Hybrids

#### Nickel-TiC-Graphite Hybrids

A new class of Ni-Ti-C based metal matrix composites has been developed using the laser engineered net shaping (LENS™) process. These composites consist of an in situ formed and homogeneously distributed titanium carbide (TiC) phase reinforcing the nickel matrix.

Additionally, by tailoring the Ti/C ratio in these composites, an additional graphitic phase can also be engineered into the microstructure. Serial-sectioning followed by three-dimensional reconstruction of the microstructure in these composites, reveals homogeneously distributed primary and eutectic titanium carbide precipitates as well as a graphitic phase encompassing the primary carbides, within the nickel matrix. The morphology and spatial distribution of these phases in three dimensions reveals that the eutectic carbides form a network linked by primary carbides or graphitic nodules at the nodes, suggesting interesting insights into the sequence of phase evolution. These three-phase Ni-TiC-C composites exhibit excellent tribological properties, in terms of an extremely low coefficient of friction while maintaining a relatively high hardness.

### Task B: Ceramic-Ceramic Hybrids

Thermodynamically stable protective oxide nanolaminates (ZnO/Al<sub>2</sub>O<sub>3</sub>/ZrO<sub>2</sub>) have been deposited by atomic layer deposition (ALD) to infiltrate porous CCC and graphite foams in order to improve their thermal stability and sliding wear resistance. The results indicate carbothermal reduction to be C driven as CO would be expected to be orders of magnitude faster than C and cause unlocalized diffusion (within the sample pores). Based on the above, carbothermal reduction of zirconia is more dependent on solid-solid reaction than gas-solid reaction, which is in disagreement with previous research findings that suggest carbothermal reduction of zirconia to be only a CO driven reaction mechanism.

### Task C: Metal-Carbon Nanotube Hybrids

#### Nickel-Carbon Nanotube (CNT) hybrid materials:

Two types of carbon nanotube reinforced nickel (CNT/Ni) nanocomposites were processed, both involving spark plasma sintering (SPS) of precursor powders consisting of nickel and carbon nanotubes. The first type involved simple mechanical dry milling (DM) of nickel and CNT powders, followed by sintering using SPS, resulting in nanocomposites exhibiting a tensile yield strength of 350 MPa (about two times that of SPS processed monolithic nickel with a strength of 160 MPa) and about 30% elongation to failure. In contrast, the nanocomposites processed by spark plasma sintering of powders prepared by molecular-level mixing (MLM) exhibited substantially higher tensile yield strength of 690 MPa but limited ductility with a 8% elongation to failure. While the former type of processing involving dry-milling is expected to be lower in cost as well as easy to scale-up, the latter processing technique involving molecular-level mixing

leads to a more homogeneous distribution of nanotubes leading to extraordinarily high strength levels.

*Nickel-Graphite Nanoplatelet Hybrid Materials:*

While multiple recent reports have demonstrated enormous enhancements in yield strength in metal matrix nanocomposites reinforced with carbon nanotubes and graphite nanoplatelets (GNP), such composites typically exhibit drastic reductions in tensile ductility. Mechanical mixing of nickel (Ni) powders and GNP powders, followed by spark plasma sintering (SPS), has been used to develop a new class of GNP/Ni nanocomposites that exhibit huge enhancements in tensile yield strength while preserving good ductility. Thus, a Ni-1GNP (1 vol.% GNP) nanocomposite exhibited a tensile yield strength of 370 MPa (about 2.5 times of SPS processed monolithic nickel ~ 160 MPa) and an elongation to failure ~ 40%. Interestingly, while a higher volume fraction of GNPs, such as Ni-2.5GNP (2.5 vol.% GNP) exhibited an enhancement in tensile yield strength due to grain refinement, there was a significant reduction in ductility ~ 10%, primarily due to agglomeration of GNPs. The enhancement in the tensile strength and ductility of the Ni-1GNP nanocomposite can be attributed to combined effect of homogeneous dispersion of GNPs and grain refinement, the relative influence of each of these effects has been quantitatively assessed in this paper. Additionally, the strong metal-GNP interfacial bonding helps effectively transfer load across the GNP/metal interface during tensile deformation.

## 2. Introduction

The program under the Institute for Science and Engineering Simulation (ISES), was established at the University of North Texas, to develop and apply novel materials characterization, modeling, and simulation tools to aid in the future inspection, repair and design of improved materials and processes for aerospace applications. Specifically, the program focused on developing the fundamental understanding required to support safety engineers in their ability to upgrade and maintain the Air Force's aging fleet by predicting material performance and structural integrity using principles based on mechanics and deformation of materials. This multifunctionality necessitates a strong coupling between structural performance and other functionalities such as electrical, magnetic, optical, thermal, biological, chemical, and so forth. Structural integrity includes durability, survivability, reliability, and maintainability. ISES thus focused on developing new design and performance criteria involving material science, mechanics, physics, and chemistry to model and characterize the processing and performance of multifunctional materials and microsystems at multiple scales from atoms to the continuum.

Projected Air Force applications require material systems and devices capable of sustained performance in complex or hostile loading environments. Such systems and devices often consist of different materials with different functionalities, and as such intrinsically involve heterogeneous interfaces between often chemically and mechanically incompatible materials. Examples include high temperature metallic materials, hybrid structural materials, multi-directionally reinforced composites, reactive multi-constituent materials, three-dimensional functionally graded material systems, and a variety of micro- and nano-systems.

The work carried out under the ISES has led to the development of a leading edge facility for research, education and training on novel characterization and simulation techniques and tools. It has led to a multi-disciplinary hub to connect simulation and activities on collaborative projects both at the University of North Texas and off-site. ISES has provided a unique platform for researchers in materials characterization, computational materials science, as well as computational chemistry to work in a symbiotic fashion for addressing critical and relevant problems of direct interest to the Air Force and other DOD agencies.

The activities carried out under the ISES program heavily leveraged the recent investments made by the federal government to expand the University of North Texas' capabilities in both characterization and modeling. This included a state-of-the-art materials characterization facility in the Center for Advanced Research and Technology (CART) and the advanced computational and simulation facilities in the Center for Advanced Scientific Computing and Modeling (CASCaM). Furthermore, as a direct outcome of the activities carried out under ISES, the investigators working on this program have subsequently developed individual and/or joint research projects currently funded by the National Science Foundation, U.S. Department of Education, U.S. Department of Energy, and Texas Advanced Research Program. The three primary thrust areas that were addressed under the ISES program umbrella were:

1. Lifetime Prediction of Turbine Blades
2. Influences of Microstructure and Chemistry on the Mechanical Properties of Advanced Aerospace Alloys

### 3. Three-dimensional Functionally-graded Hybrid Materials for Aerospace Structural Applications

Under each of the above mentioned thrust areas, there were multiple tasks that were carried out, the details of which have been described in the section on Results and Discussion.

### 3. Methods, Assumptions, and Procedures

- SEM - SEM was the first experiment done for most of the samples and was used frequently for imaging in secondary electron (SE) and back-scattered electron detection (BSED) in FEI-Quanta NovaSEM 230. This SEM was also used for EDS and EBSD. FEI Nova 200 NanoLab FIB/SEM was used extensively for TEM and APT sample preparation.
- XRD - X-ray diffraction analysis of nanocomposites was performed using (1.54 Cu  $\alpha$ ) line of Rigaku Ultima III X-Ray diffractometer. High energy XRD was performed in the ANL in Chicago.
- TEM - TEM samples analyzed on a FEI Tecnai G2 F20 field emission gun transmission electron microscope, operated at 200 kV. HRSTEM was performed on a FEI Titan 80-300 microscope, operated at 300 kV, equipped with a CEOS probe aberration corrector.
- APT - APT experiments were conducted using a CAMECA local electrode atom probe 3000X HR instrument. APT experiments were carried out in the voltage or laser evaporation mode at a set temperature and target evaporation. Data analyses were carried out using CAMECA IVAS<sup>TM</sup> 3.6 software.
- XPS - PHI 5000 Versaprobe Scanning XPS Microprobe with UPS was used for surface analysis and surface chemistry quantification. The main utility of this instrument was for depth profiling of interstitial elements.
- Density functional theory based ab-initio calculations were carried out using Vienna ab initio Simulation Package (VASP). In the electronic structure calculations, a plane wave basis set with a kinetic energy cutoff of 400 eV with Projected Augmented Wave (PAW) pseudopotentials were used in the simulations. The generalized gradient approximation (GGA) with the Perdew-Burke-Ernzerhof (PBE) form was used for the exchange and correlation functions and all the calculations performed were spin polarized. The initial structures were fully relaxed until the forces acting on each of the atoms were less than 0.01 eV/Å.
- Phase-field modeling was performed using in-house codes based on Fortran programming language, which uses finite-difference method for numerically solving differential equations. Such equations have been described in detail Task D.

## 4. Results and Discussion

### 4.1 Thrust Area I: Lifetime prediction of turbine blades

Single crystal Ni-based superalloys used in turbine aerofoils of jet engines are exposed to long dwell times at very high temperatures. In particular, the understanding of creep in single crystal superalloy turbine blades is of importance for designing more reliable and fuel efficient aircraft engines. Creep tests on Ni-based single-crystal superalloy sheet specimens typically show greater creep strain rates and/or reduced strain or time to creep rupture for thinner specimens than predicted by current theories, which predict a size-independent creep strain rate and creep rupture strain. This size dependent creep response is termed the thickness debit effect. To investigate the mechanism of the thickness debit effect, isothermal, constant nominal stress creep tests were performed on uncoated PWA1484 Ni-based single-crystal superalloy sheet specimens of thicknesses 3.18 and 0.51 mm under two test conditions: 760 °C/758 MPa and 982 °C/248 MPa. The microscopic analysis revealed that the specimens contained initial micro-voids formed during the solidification and homogenization processes. For the specimens tested at 760 °C/758 MPa, microscopic analyses revealed that the thick specimens exhibited a mixed failure mode of void growth and cleavage-like fracture while the predominant failure mode for the thin specimens is cleavage-like fracture. The creep specimens tested at 982 °C/248 MPa in air showed the development of surface oxides and a near-surface precipitate-free zone. Further analysis of the precipitate-free zone revealed signs of recrystallization. A simple finite-element analysis of the near surface layered structure formed during high temperature creep, revealed that the presence of the alumina layer at the free surface imposes a constraint that locally increases the stress triaxiality and changes the value of the Lode parameter (a measure of the third stress invariant). The surface cracks formed in the oxide layers were found to be arrested by further oxidation and hence did not play a major role in the final failure. For the specimens with thickness of 3.18 mm the failure mode was predominantly void nucleation, growth and coalescence, whereas for the specimens with thickness of 0.51 mm a mixed mode of ductile and cleavage-like fracture was observed.

In order to quantify the role of void growth in single crystals under creep loading conditions, three dimensional finite deformation finite element analyses of unit cells containing a single initially spherical void was carried out. The materials were characterized by a rate dependent crystal plasticity constitutive relation accounting for both primary and secondary creep. Two types of imposed loading were considered: an applied true stress (force/current area) that is time independent; and an applied nominal stress (force/initial area) that is time independent. Isothermal conditions were assumed. The evolution of porosity was calculated for various values of the stress triaxiality and of the Lode parameter. The evolution of porosity with time is sensitive to whether constant true stress or constant nominal stress loading is applied. However, the evolution of porosity with the overall unit cell strain is insensitive to the mode of loading. At

high values of stress triaxiality, the response is essentially independent of the value of the Lode parameter. At sufficiently low values of the stress triaxiality, the porosity evolution depends on the value of the Lode parameter and void collapse can occur. Also, rather large stress concentrations can develop which could play a role in the observed thickness dependence.

Following the observation that depending on the stress state the voids can either grow and coalesce or collapse and close up. A further investigation of the possible transition between void collapse for well separated voids to coalescence for sufficiently close voids in a nonlinearly viscous single crystal subject to creep loading was carried out. For a fixed value of stress triaxiality of 1/3 and three values of the Lode parameter 1, 0 and -1 three dimensional unit cell calculations were carried out for two initial void volume fractions and, for each initial void volume fraction, a range of inter void spacing were considered. The materials were characterized by a rate power law viscous crystal plasticity constitutive relation and three values of the power law creep exponent were considered. The results show that, for sufficiently closely spaced voids, void coalescence occurs while for widely spaced voids void collapse can occur. Whether void coalescence, void collapse or neither occurs mainly depends on the value of the Lode parameter. The calculations also showed that as the void coalesces or collapses, a stress concentration develops which can then trigger cracking as seen in the experiments.

The effect of crystal orientation on porosity evolution in a face centered cubic (fcc) single crystal subject to tensile creep loading was also carried out. Here as well the matrix material was characterized by a rate power law viscous crystal plasticity constitutive relation. Three dimensional finite deformation finite element analyses of initially cubic unit cells containing a single initially spherical void were carried out for three crystal orientations of the main loading direction together with two other cases were analyzed to study the effect of secondary orientations. The calculations were carried out for three values of the stress triaxiality and for each stress triaxiality value three values of the Lode parameter were considered. Two of the crystal orientations considered were significantly anisotropic orientations. Symmetry boundary conditions were imposed consistent with the crystal symmetry; the sides of the unit cell were not constrained to remain straight. It was found that for an anisotropic orientation, the Lode parameter can have a significant effect on the evolution of creep strain and porosity even at relatively high values of the stress triaxiality. It was shown that for certain orientations enhanced creep rate can occur without any void growth or even when void collapse takes place. Also, whether or not a stress concentration greater than the elastic stress concentration develops was found to depend on crystal orientation.

Based on the experimental observations and detailed finite element calculations a mechanistic model for the observed thickness debit effect in the creep response of Ni-based single crystal super alloys was proposed. The phenomenological model is a nonlinear parallel spring model for uniaxial creep with springs representing the bulk and possible surface damage layers. The nonlinear spring constitutive relations model both material creep and evolving damage. The

number of springs and the spring creep and damage parameters were based, as much as possible, on the experimental observations of thickness debit effect. The bulk damage mechanisms accounted for were the nucleation of cleavage-like cracks from preexisting voids and, at the higher temperature, void nucleation. The surface damage mechanisms modeled at the higher temperature were an oxidation layer, a  $\gamma'$ -precipitate free layer and a  $\gamma'$ -precipitate reduced layer. Model results for the creep response and for the thickness debit effect were in close quantitative agreement with the experimental results. In addition, the model predicted qualitative features of the failure process that were in good agreement with experimental observations. The simplicity of the model also allowed parametric studies to explore the relative roles of bulk and surface damage as well as the relative roles of cleavage-like cracking and void nucleation in the bulk.

## **4.2. Thrust Area II: Influences of Microstructure and Chemistry on Mechanical Properties of Aerospace Materials**

### **4.2.1. Task A: Structure and chemistry across $\gamma/\gamma'$ interfaces in nickel-based superalloys**

Through a combination of aberration-corrected high resolution scanning transmission electron microscopy (HRSTEM) and three-dimensional atom probe (3DAP) tomography, the true atomic scale structure and change in chemical composition across the complex order/disorder interface in a metallic alloy has been determined. The study reveals the presence of two interfacial widths, one corresponding to an order-disorder transition, and the other to the compositional transition across the interface, raising fundamental questions regarding the definition of the interfacial width in such systems.

This work was carried out on the nickel base superalloy Rene' 88 DT (nominal composition 55.63Ni-18.02Cr-13.00Co-4.74Ti-4.45Al-2.48Mo-1.21W-0.46Nb (in at%)), with superior creep and fatigue properties for turbine disk applications [Krueger et.al. (1990), Krueger et.al. (1992), Wlodek et.al. (1996)], The typical microstructure consists of a disordered *fcc*  $\gamma$  matrix with ordered  $L1_2$   $\gamma'$  precipitates of varying sizes depending upon processing history [Wlodek et.al. (1996)]. Bore and rim specimens from a turbine disk [DSO Engine Systems Prognosis] were subjected to a supersolvus anneal (30 min. at 1150  $^{\circ}$ C), in the single  $\gamma$  phase field, followed by cooling at 24  $^{\circ}$ C/min to room temperature, and subsequent aging for 50 hours at 760  $^{\circ}$ C (to achieve a near-equilibrium condition), resulting in the formation of larger ( $> 200$  nm) primary  $\gamma'$  and smaller ( $< 50$  nm) secondary  $\gamma'$  precipitates. Samples for EFTEM and HRSTEM studies were prepared by machining of 3 mm discs, followed by  $Ar^+$  ion milling on Fischione Model 1010 and Model 1040 systems. EFTEM studies were carried out using the Cr M-edge (at 42 eV) in the electron energy loss spectrum to enhance contrast between the Cr-depleted  $\gamma'$  precipitates and the Cr-enriched  $\gamma$  matrix [Saros et.al. (2005)].

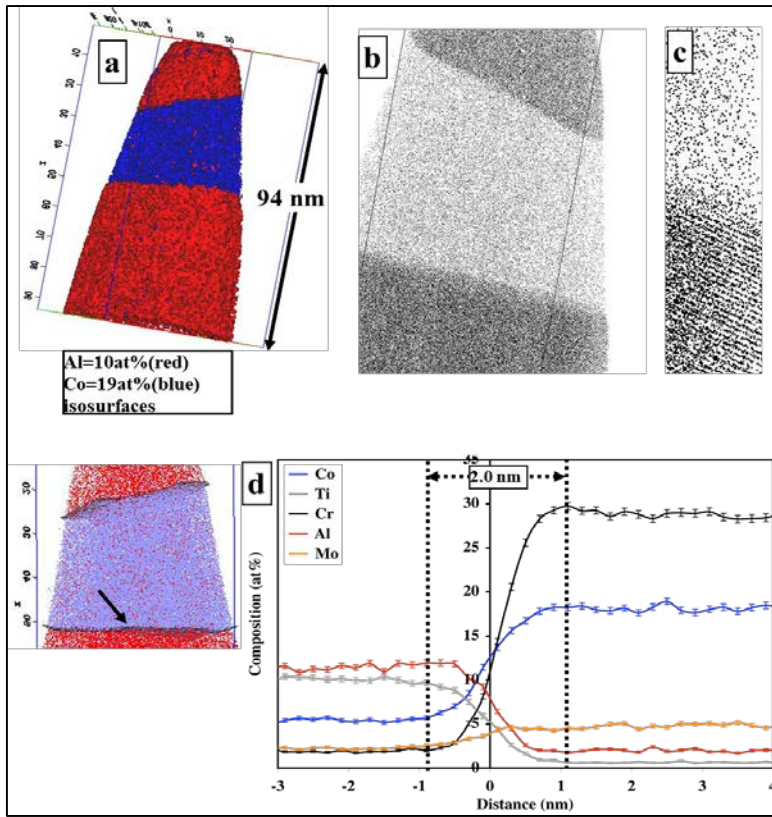


**Figure 1:** (a) Al 10% (red) and Co 19% (blue) isosurfaces depicting morphology of the  $\gamma'$  precipitate used in 3DAP analysis; the red area is indicative of the primary  $\gamma'$  precipitate, (b) and (c) higher magnification views showing the stacking of alternate (002) Al planes within the  $\gamma'$ , (d) Proximity Histogram depicting the compositional transition across the  $\gamma$  /  $\gamma'$  interface; the area used in the analysis is indicated by the arrow in the inset.

Atomic resolution, Z-contrast, imaging (through High Angle Annular Dark Field (HAADF)-HRSTEM) was performed on a FEI Titan 80-300 microscope, operated at 300 kV, equipped with a CEOS probe aberration corrector. Primary  $\gamma'$  precipitates were chosen to ensure a planar interface parallel to the beam direction, across the foil thickness. To ensure consistency between the HRSTEM and 3DAP analyses, a  $\gamma/\gamma'$  interface parallel to the {002} planes was specifically chosen. The ordered  $L1_2$ ,  $Ni_3Al$ -based, structure of the  $\gamma'$  phase consists of two distinct sublattices, the Ni sublattice corresponding to the face-center positions and the Al sublattice corresponding to the corner positions of the cubic unit cell. This yields alternating {002} planes of pure Ni and 50% Ni and 50% Al atoms, respectively, when viewed along the  $\langle 100 \rangle$  direction. In case of Rene'88 DT (with several alloying elements), the  $\gamma'$  phase exhibits alternating heavier Ni-rich (with other substitutional atoms such as Co) and lighter Al-rich (with other atoms such as Ti) {002} planes, presenting direct evidence of the  $L1_2$  superlattice structure. A clear order-disorder transition zone can be defined at the  $\gamma/\gamma'$  interface where the long-range order decreases roughly over 6-8 atomic {002} planes (approximately 1 to 1.3 nm). Similarly a compositional

transition zone (measuring 2.7 nm) can be defined. Measurements of the interface width, as determined through HRSTEM studies, were made by calculating the average and standard deviation of the peak intensities representing the Ni and (Ni+Al/Ti) planes respectively in the  $\gamma'$ , and the intensity peaks in the  $\gamma$  phase. The interface width for each measurement was defined as the minimum interval (in integral {002} plane spacings) between the 95% CI values separating the  $\gamma$  and  $\gamma'$ . An average value of approximately 2.2 nm (between 12-14 {002} planes), with a standard deviation of approximately 0.5 nm, was obtained over several measurements of the interface width. Note that due to the small lattice mismatch between the  $\gamma$  matrix and  $\gamma'$  precipitates in this alloy (< 0.05%), the elastic strains at the interface are small; consequently, any thin-foil relaxation effects on the experimentally observed compositional gradients, are expected to be relatively low.

The above HRSTEM studies have been complemented with 3DAP experiments for quantitatively probing the compositional gradients across the  $\gamma/\gamma'$  interface. Needle-shaped 3DAP specimens with a tip radius  $\sim 50$  nm were prepared (from the same Rene' 88 DT sample) by a combination of electro-discharge machining (EDM), electropolishing and focused ion beam (FIB) techniques [Hwang et.al. (2009)]. 3DAP experiments were conducted on a LEAP<sup>TM</sup> 3000 microscope manufactured by Imago Scientific Instruments, Inc. Fig.1(a) shows a 3D reconstruction depicting iso-concentration surfaces for Co (19 at%), corresponding to the  $\gamma$ , and Al (10 at%), corresponding to the  $\gamma'$ . From the size scale, it is apparent that these are sections of primary  $\gamma'$  precipitates separated by a  $\gamma$  channel. A 3DAP reconstruction of only Al atoms (black dots), exhibiting the higher concentration of Al within the  $\gamma'$  phase, is shown in Fig.1(b). Fig.1(c) is a magnified view of the lower  $\gamma/\gamma'$  interface from Fig.1(b), showing ordered planes of Al atoms with a plane spacing of  $\sim 0.36$  nm, corresponding to the alternate Al-rich {002} planes in the ordered  $\gamma'$  phase, confirming that the  $\gamma/\gamma'$  interface is perpendicular to the (z) axis of the sample. Note that Fig.1(c) exhibits an order-disorder transition zone  $\sim 4$ -6 {002} planes wide (0.7-1 nm), in good agreement with the HAADF-HRSTEM results. For a statistically relevant quantitative analysis of the compositional gradient across this interface (indicated by an arrow in Fig.1(d)), compositional profiles for the primary alloying elements have been plotted in the form of a proximity histogram [Hellman et.al. (2000)] in Fig.1(d). While heavier Cr and Co partition preferentially to the  $\gamma$ , the lighter Al and Ti partition to the  $\gamma'$  with a clear gradient across the interface, consistent with the HRSTEM observations. Based on the Cr and Co profiles, the width of the compositional gradient across the interface shown can be measured to be  $\sim 2.0$  nm (average value  $\sim 2.4$  nm), in excellent agreement with the HAADF-HRSTEM observations.

Recent results on atomistic modeling of the  $\gamma/\gamma'$  interface in the binary Ni-Al system by Mishin [Mishin (2004)] and Ardell and Ozolins [Ardell and Ozolins (2005)] predict that the order-disorder interface is not atomically abrupt. Mishin's results on Ni/Ni<sub>3</sub>Al interfaces [Mishin (2004)] indicate that the decay in long-range order across the interface (measured through variation in the Al-sublattice occupancy across the interface) can occur over 4-6 atomic layers or

~ 0.7 – 1.0 nm. This *predicted* value is in excellent agreement with our experimentally observed width of the order-disorder transition zone at the interface. Furthermore, the HAADF-HRSTEM and 3DAP observations indicate significant tolerance to compositional off-stoichiometry within the  $\gamma'$  phase.

Coupling of HAADF-HRSTEM Z-contrast atomic resolution imaging with 3DAP Tomography serves to illustrate that the order/disorder interface in a nickel base alloy is not atomically abrupt but has a transition width, in agreement with prior atomistic simulations [Mishin 2004, Ardell 2005]. Furthermore, two transition “zones” can be defined, with the width of the order-disorder transition zone being smaller than the width of the compositional gradient. These results thus raise fundamental questions regarding the basic definition of an interface between an ordered phase and the surrounding disordered matrix and in general between two structurally and compositionally distinct phases. The structural and compositional diffuseness of the interface impacts the microstructural stability and mechanical properties of these metallic alloys, as it influences key parameters such as lattice misfit and coherency strains, which in turn directly impact the strengthening mechanisms and deformation behavior at elevated temperatures. The atomic-scale knowledge of structure and chemical composition is essential for a fundamental physically-based understanding of such complex interfaces.

#### **4.2.2. Task B: Three-dimensional characterization of nanoscale $\gamma'$ precipitates in nickel-based superalloys**

The present study investigates the influence of alloy composition on  $\gamma'$  precipitation in Ni-8Al-8Cr at% and Ni-10Al-10Cr at% during continuous cooling from a supersolvus temperature. When subjected to the same cooling rate, Ni-8Al-8Cr develops a monomodal population whereas Ni-10Al-10Cr develops a multimodal (primarily bimodal) population of  $\gamma'$  precipitates. The bimodal  $\gamma'$  precipitate size distribution in Ni-10Al-10Cr alloy can be attributed to two successive nucleation bursts during continuous cooling while the monomodal  $\gamma'$  size distribution in Ni-8Al-8Cr results from a single nucleation burst followed by a longer time – wider temperature window for nucleation resulting in a larger number density of precipitates. Three-dimensional atom probe investigations reveal that while local equilibrium is achieved across the  $\gamma/\gamma'$  interface, far-field  $\gamma$  compositions still retain an excess of Al and a depletion of Cr with respect to equilibrium, thus giving direct experimental evidence of the driving force for subsequent nucleation bursts during continuous cooling in case of Ni-10Al-10Cr. Contrastingly, in case of the Ni-8Al-8Cr alloy, while the  $\gamma$  phase retains an excess of Al and a depletion of Cr with respect to equilibrium after continuous cooling to room temperature, the additional driving force is consumed during subsequent isothermal annealing by growth of the large number of  $\gamma'$  precipitates without any new nucleation.

A partial ternary phase diagram of Ni-8Al-8Cr and Ni-10Al-10Cr at 600 °C, generated based on solution thermodynamic models using the PANDAT™ software, predicts the equilibrium volume fraction of  $\gamma'$  precipitates to be 15.1% and 51.5% with corresponding  $\gamma'$  solvus temperatures of 725.9 °C and 938.3 °C, respectively for the Ni-8Al-8Cr and Ni-10Al-10Cr compositions. A calculated end point composition of  $\gamma'$  phase for both alloys are Ni-18Al-6Cr whereas the end points of  $\gamma$  matrix are Ni-6Al-10Cr and Ni-4Al-15Cr for Ni-8Al-8Cr and Ni-10Al-10Cr alloy, respectively.

A comparison of the microstructures of the Ni-8Al-8Cr and Ni-10Al-10Cr alloys, continuously-cooled at the same nominal rate after solution-treatment, were done by SEM and TEM. In the Ni-8Al-8Cr sample the  $\gamma'$  precipitates exhibit a monomodal size distribution with an average size  $\sim$ 10 nm whereas the Ni-10Al-10Cr sample shows multiple populations of  $\gamma'$  precipitates. A relatively low density of nucleation sites and larger size scale of primary  $\gamma'$  precipitates in Ni-10Al-10Cr sample suggest that they formed at a higher temperature as compared to Ni-8Al-8Cr, while experiencing the same cooling rate. The size distribution of primary  $\gamma'$  precipitates in Ni-10Al-10Cr alloy has been measured based on multiple SEM images. Based on these measurements, primary  $\gamma'$  precipitates range in size from 40 to 140 nm with an average  $\sim$  95 nm. Smaller size secondary  $\gamma'$ , measured from different EFTEM images recorded at different TEM sample locations have sizes ranging from 3 to 17 nm with an average diameter  $\sim$ 10nm.

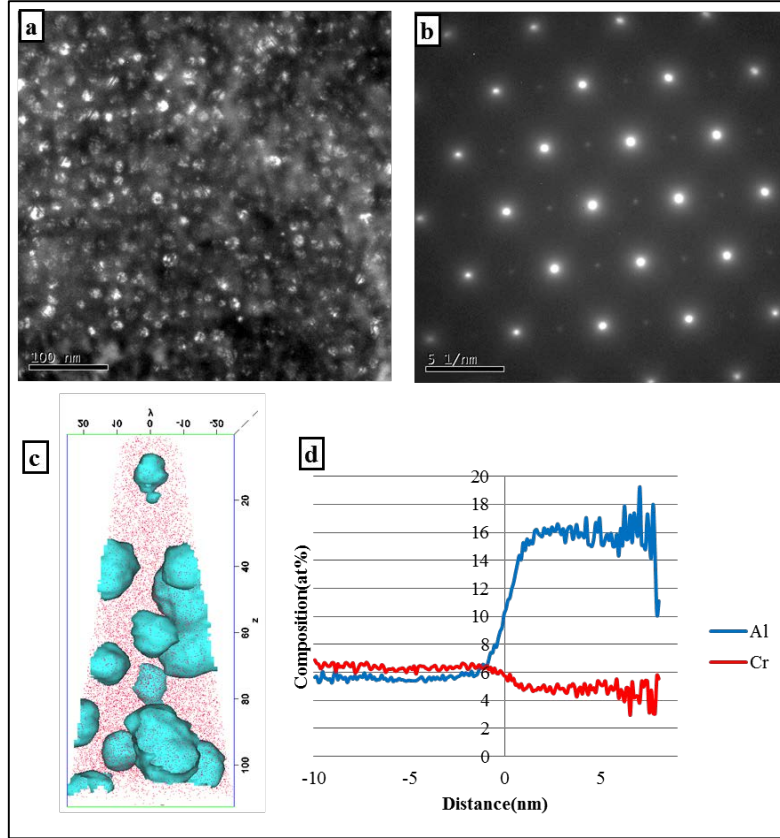


**Figure 2:** a) Dark field image of Ni-8Al-8Cr at% sample after isothermal aging at 600 °C for 256 hours, post continuous cooling b) SADP corresponding to the dark-field image c) 3-D reconstruction of 10 at% Al isoconcentration surface delineating d) proximity histogram for Al and Cr corresponding to 10 at% Al isosurface shown in c).

Three-dimensional atom probe (3DAP) were performed for both Ni-8Al-8Cr and Ni-10Al-10Cr alloys. For both alloy compositions,  $\gamma'$  precipitates exhibit a near-equilibrium composition  $\sim$  Ni-16.4Al-6Cr [Caron (2000), Saunders et.al. (1996), Dupin et.al. (2001)], suggesting  $\gamma'$  precipitation via a classical nucleation and growth mechanism. It was evident that while local equilibrium has been established near the  $\gamma/\gamma'$  interface, there is a far-field departure from equilibrium in the  $\gamma$  matrix, involving an excess of Al and a depletion content of Cr. This effect appears to be more pronounced in case of the primary and secondary  $\gamma'$  precipitates in the Ni-10Al-10Cr alloy. The interface width has been determined based on the difference of the local  $\gamma$  and  $\gamma'$  compositions. The  $\gamma/\gamma'$  interface width is greater than 4 nm for Al and  $\sim$ 3 nm for Cr, in case of the Ni-8Al-8Cr alloy. While the  $\gamma/\gamma'$  compositional width is  $\sim$ 4 nm for Al, the value appears to be substantially larger for Cr ( $\sim$ 5 nm) in case of Ni-10Al-10Cr. The rather diffuse nature of the Cr profile in case of this alloy needs further investigation.

Fig. 3 shows the microstructure of the Ni-8Al-8Cr alloy after isothermal annealing at 600 °C for 256 hours, post continuous cooling. The growth and coarsening of the monomodal  $\gamma'$  distribution

is clearly visible in the dark-field TEM image shown in Fig. 3(a). The corresponding <011> zone axis diffraction pattern is shown in Fig. 3(b). The larger  $\gamma'$  precipitate size is also confirmed by the 3DAP reconstruction (Fig. 3(c)). The Al and Cr proxigram composition profiles, shown in Fig. 3(d), clearly exhibit that  $\gamma'$  composition remains the same as in case of the continuously cooled sample. In contrast, the average  $\gamma$  matrix composition after isothermal annealing increases in Cr content while decreasing in Al content, as compared to the continuously cooled condition due to the growth of the large number of  $\gamma'$  precipitates. Furthermore, the differences between the  $\gamma$  compositions near and far from the  $\gamma/\gamma'$  interface has also substantially reduced after isothermal annealing. Interestingly, the compositional width of the interface (for both Al and Cr profiles) decreases after isothermal annealing.

The  $\gamma'$  and local as well as far-field  $\gamma$  compositions together with the corresponding interface widths are summarized in Table 1.

Table 1: Composition and interface width of  $\gamma'$

Condition		Proximity histogram composition				Interface width (nm)	
		Adjacent gamma Matrix		Gamma Prime		Al	Cr
		Al	Cr	Al	Cr		
<b>Ni-8Al-8Cr</b>	Continuous cooling	7.4	8	16.4	6	> 4	3.0
	Continuous cooling+ 600C 256 h	5.8	6.6	16	5.1	3.2	2.5
<b>Ni-10Al-10Cr</b>	Continuous cooling : Primary $\gamma'$	4	15.1	16.3	7	3.9	4.9
	Continuous cooling : Secondary $\gamma'$	4.5	15.1	17.8	7	3.85	4.8

Based on these experimental observations, the nucleation and growth of  $\gamma'$  precipitates during the continuous cooling of both Ni-10Al-10Cr and Ni-8Al-8Cr alloys can be compared and contrasted. In case of Ni-10Al-10Cr, the primary  $\gamma'$  results from the first nucleation burst at higher temperatures near the solvus temperature, at a critical undercooling. Consequently, a low nucleation rate resulting in a low number density of precipitates is observed. These primary  $\gamma'$  precipitates grow rather rapidly due to the fast diffusion rates at these high temperatures and thereby reduce the supersaturation of the  $\gamma$  matrix. However, it should be noted that only local near-field equilibrium is established between the  $\gamma$  and  $\gamma'$  phases across the interface. The far-

field  $\gamma$  composition still retains a super-saturation of Al and an under-saturation of Cr. Nucleation of precipitates can continue as long as there is no overlap of the long-range diffusion fields from adjacent primary  $\gamma'$  precipitates, also referred to as soft impingement. However, as soon as soft impingement takes place, nucleation of primary precipitates is shut down, as discussed by Radis et. al. [Radis et.al. (2009)] and Wen et. al. [Wen et.al. (2003)]. The growth of the primary  $\gamma'$  precipitates is also slowed down due to a soft impingement. Further continuous cooling, eventually leads to increased supersaturation within the retained  $\gamma$  matrix, resulting in sufficient driving force for a second nucleation burst at lower temperatures [Wen et.al. (2003), Wen et.al. (2006), Payton et.al. (2010), Babu et.al. (2001)]. This second burst leads to the formation of secondary  $\gamma'$  precipitates. While the secondary nucleation burst occurs at lower temperature, it should be noted that the  $\gamma$  matrix composition has changed due to the precipitation of primary  $\gamma'$ . Hence, the critical undercooling corresponding to this secondary burst is still similar to that for the primary burst. However, due to the lower temperatures, the diffusion is severely restricted leading to a longer time period before soft impingement can take place. Consequently, the secondary  $\gamma'$  nucleation burst persists over a wider temperature range. This larger temperature range results in a broader size distribution of fine scale precipitates, and an effectively larger nucleation rate.

In case of the Ni-8Al-8Cr alloy, the substantially lower  $\gamma'$  solvus temperature as compared with Ni-10Al-10Cr, leads to a much lower temperature at which the primary  $\gamma'$  nucleation burst takes place. The lower nucleation temperature results in substantially reduced diffusivities leading to longer time periods to soft impingement, consequently allowing nucleation to continue for a longer time period (or wider temperature window). Therefore, in principle the primary  $\gamma'$  nucleation burst in case of Ni-8Al-8Cr mimics the features reflected by the secondary  $\gamma'$  nucleation burst in case of Ni-10Al-10Cr. The higher number density of  $\gamma'$  precipitates in this case eventually leads to shorter inter-precipitate separation allowing for the intervening  $\gamma$  matrix to achieve a composition closer to equilibrium. This prevents the development of any substantial supersaturation within the  $\gamma$  matrix thus preventing a second nucleation burst. Additionally, the lower temperatures and diffusivities also kinetically hinder any second nucleation burst. This also explains the monomodal  $\gamma'$  size distribution in case of the Ni-8Al-8Cr alloy.

#### **4.2.3. Task C: Lattice parameters of $\gamma$ and $\gamma'$ phases and site occupancies in ordered $\gamma'$ phase**

Nickel based superalloys have been critical for aerospace and power applications due to excellent high temperature properties. These high temperature properties have been attributed to the coherently precipitated gamma prime phase in the gamma matrix. The segregation of alloying elements between the matrix and gamma prime phase drives precipitate misfit strains and impacts material strength. This study aims at understanding the site preference of Co and Cr within the ordered gamma prime phase. The study also calculates the interaction energy between alloying additions within the ternary systems Ni-Al-Cr and Ni-Al-Co, and the quaternary system

Ni-Al-Cr-Co. Results show that the Co shows a mixed substitution behavior between the Al and Ni sites in the gamma prime phase. The results from Ni-Al-Cr ternary system shows that two Cr atoms favor being close to each other, with the most stable configuration of first nearest neighbors of Al-Al site. The interaction energies calculated from the Ni-Al-Co system show that the initial distance between two Co atoms will decide if the two Co atoms prefer Ni-Ni or Ni-Al configuration. The study on the quaternary system Ni-Al-Cr-Co reveals that the initial configuration of Cr and Co atoms will affect the final most stable configuration. The results were found to be consistent with our previous findings.

#### 4.2.3.1 Site Preference Energies for Co

Site preference for the Co atom has been studied through three formalisms similar to the Cr and Ti [Wu and Li (2012)] atom i.e. standard defect formation formalism, anti-site formation based formalism [Jiang and Gleeson (2006)] and vacancy formation based formalism.

Standard defect formation formalism [C. Booth-Morrison et.al. (2008)] based calculations suggested that Co shows a very strong preference for Ni site in both the cases of 2x2x2 and 3x3x3 supercells owing to the lower defect formation energy. The formation energies have been calculated using the following equation,

$$\begin{aligned} E_{Co_{Ni}} &= [(E(Ni_{(X-1)}CoAl_Y) + \mu_{Ni}) - (E(Ni_XAl_Y) + \mu_{Co})] \\ E_{Co_{Al}} &= [(E(Ni_X(Al_{(Y-1)}Co)) + \mu_{Al}) - (E(Ni_XAl_Y) + \mu_{Co})] \end{aligned} \quad (1)$$

Table 2 Site preference energies (eV) for Co substitution calculated from the standard defect formalism with different supercell sizes.

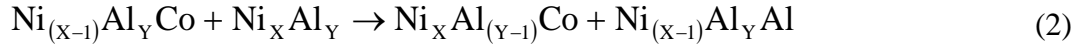
Standard defect formation formalism –Co	This work		Other studies
	2x2x2	3x3x3	
$E_{Co}^{Al}$	2.047	1.921	2.65 [ Q. Wu 2012]
$E_{Co}^{Ni}$	0.037	0.701	0.40 [ Q. Wu 2012]

Table 2 shows that the value of  $E_{Co}^{Ni}$  is significantly lower than the value of  $E_{Co}^{Al}$ .

The calculated energies for 2x2x2 supercell show a good consistency with the results obtained by Wu and Li [Wu and Li (2012)]. The energies obtained with the 3x3x3 supercell show slightly different numbers than those obtained from 2x2x2 super cell and those from the reference [Wu and Li (2012)]. This difference of the site preference energies from standard defect energy

formation of two super cell sizes was also observed in the anti-site and vacancy based mechanisms. These differences might be due to the interactions between substituted atoms in neighboring cells.

Anti-site based substitution formalism confirms with the study done by several researchers including Jiang and Gleeson [Jiang and Gleeson (2006)] and [Wu and Li (2012)] The value of the energy required to move the Co atom from Ni site to an Al site was calculated by using the following equation,



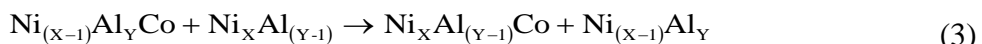
$$E_{\text{Ti}}^{\text{Ni} \rightarrow \text{Al}} = E(\text{Ni}_X\text{Al}_{(Y-1)}\text{Co}) + E(\text{Ni}_{(X-1)}\text{Al}_Y\text{Al}) - E(\text{Ni}_{(X-1)}\text{Al}_Y\text{Co}) - E(\text{Ni}_X\text{Al}_Y)$$

Table 3 Site preference energies (eV) for Co substitution calculated from the anti-site formation based formalism with different supercell sizes.

Anti-site based formalism -Co	This work		Other studies
	2x2x2	3x3x3	
$E_{\text{Co}}^{\text{Ni} \rightarrow \text{Al}}$	0.953	0.381	1.10 [ C. Jiang, script. 2006], 1.25 [ Q. Wu 2012]

As can be seen from Table 3, the value of  $E_{\text{Co}}^{\text{Ni} \rightarrow \text{Al}}$  falls between zero and the exchange defect energy i.e. 1.1 eV [Chaudhari et.al. (2012)], implying that the Co atom has a compositionally dependent site substitution behavior. The calculations on the effect of size of the supercell show that the value of  $E_{\text{Co}}^{\text{Ni} \rightarrow \text{Al}}$  is nearer to the Ni site preference value in the compositionally dependent behavior where as in the case of 3x3x3 supercell, it is nearer to the Al site. However, both values are in the compositionally dependent range. The results compare very well with other studies [Jiang and Gleeson (2006)].

The energy required to move the Co atom from a Ni site to an Al site is calculated in vacancy formation based formalism [M. Chaudhari 2012] by using the following equation,



$$E_{\text{Ti}}^{\text{Ni} \rightarrow \text{Al}} = E(\text{Ni}_X\text{Al}_{(Y-1)}\text{Co}) + E(\text{Ni}_{(X-1)}\text{Al}_Y) - E(\text{Ni}_{(X-1)}\text{Al}_Y\text{Co}) - E(\text{Ni}_X\text{Al}_{(Y-1)})$$

Vacancy based substitution formalism shows a contrasting behavior when it comes to the site preference. Table 4 shows that Co prefers to go to Al site irrespective of the size of the supercell i.e. 2x2x2 and 3x3x3 supercells, owing to the negative value of vacancy energy formation. The result of the vacancy based substitutional formalism totally contradicts with the results from the

anti-site based substitution formalism. The results clearly indicate that in the case of Co, there is a different way by which the substitution takes place through the mediation of anti-sites and vacancies. Through the mediation of anti-sites, Co shows a compositionally dependent behavior, whereas through the mediation of vacancies, Co shows a strong preference for the Al site. As the defect formation energy of antisite defects is much lower than that for vacancies [Chaudhari et.al. (2012)], the concentration of vacancy on either lattice sites is much lower than that of antisite so the antisite based on site substitution mechanism will dominate the preference of site occupancy of Co.

Table 4 Site preference energies (eV) for Co substitution calculated from the vacancy formation based formalism with different supercell sizes.

Vacancy-based formalism-Co	Vacancy based formalism	
	2x2x2	3x3x3
$E_{Co}^{Ni \rightarrow Al}$	-0.078	-0.286

#### 4.2.3.2. Interaction between Co-Co atoms

The effect of increasing the Co concentration on the site preference in the  $\gamma'$  phase of  $Ni_3Al$  was investigated in a similar way as in our previous work [Chaudhari et.al. (2012)] using a 3x3x3 supercell. Two Co atoms were substituted for the three possible combinations of sites i.e. Ni-Ni, Al-Al or Ni-Al. The parameter of the distance between the two Co sites represented by nearest neighbors (NN) is also taken into consideration. The total relaxed energies versus the NN distance of all the nine possible configurations clearly indicate that the energies are the lowest for the first nearest neighbors of all the three combinations of sites, suggesting potential segregation of Co atoms in the  $\gamma'$  phase.

The energy to move the Co atoms from one configuration to another was calculated in order to calculate the interaction between two Co atoms. The two Co atoms if sitting in Ni-Ni sites in first, second or third nearest neighbors, prefer to stay there because of the greater than zero energy required to move to any other configuration.

Similar calculations were done to calculate the energy to move the Co atoms from initial configuration of Ni-Al sites to final configuration of Al-Al or Ni-Ni sites. If the two Co atoms are sitting on the first nearest neighbors of Ni-Al site configuration, they would stay there owing to greater than zero value of the factor needed to move to any other configuration. Whereas, if

the two Co atoms are sitting on second or greater nearest neighbors of Ni-Al sites, then the Co would move to Ni-Ni site configuration because of the negative value of the factor.

Similar calculations were done to evaluate the energy to move the Co atoms from initial configuration of Al-Al sites to Ni-Ni or Ni-Al sites. If the two Co atoms are sitting on the Al-Al sites, then it would move to Ni-Al site preferably to first nearest neighbors because of the negative value of the factor. Contrastingly, the final configuration of Ni-Ni site will not be possible due to the greater than zero value of the factor.

If the two Co atoms are on first nearest neighbors i.e. 2.525 Å apart, then the initial configuration of Ni-Ni or Ni-Al sites are the most stable configurations, because of the positive energy required to move to any other configuration from these. Whereas, if the two Co atoms are sitting on Al-Al sites, then it has the tendency to go to first nearest neighbors of the Ni-Al site because of the negative value of the energy.

If the two Co atoms are second or third nearest neighbors i.e. more than 3.57 Å apart, then any initial site configuration will lead to final configuration of Ni-Ni sites. The initial configuration of two Co atoms in Ni-Al sites, will prefer to move to Ni-Ni sites. If the two Co atoms are in the initial configuration of Al-Al sites, then it will prefer to move to a configuration of Ni-Al sites first and then to Ni-Ni sites. One interesting observation from the calculations is that the two Co atoms in Al-Al sites cannot go directly into a final configuration of Ni-Ni in spite of being a low energy stable configuration, but have to go through an intermediate step of Ni-Al sites, which leads to Ni-Ni sites as the final configuration.

#### *4.2.3.3. Interaction between Cr-Cr atoms*

The effect of increasing the Cr concentration on the site preference in the  $\gamma'$  phase of Ni<sub>3</sub>Al was investigated in our previous work [Chaudhari et.al. 2012] using a 3x3x3 supercell. The results showed that the two Cr atoms preferred to stay close to each other on Al-Al sites.

Similar to the calculations done to study the interactions between two Co atoms in previous section, similar calculations have been performed to evaluate the effect of a Cr atom on another Cr atom in the immediate surroundings. The possible configuration includes first, second and third nearest neighbors of Ni-Ni, Ni-Al or Al-Al sites.

If the two Cr atoms are placed on Ni-Ni sites, then the Cr atoms will prefer to go to Al-Al sites and Ni-Al sites because of the negative energy to move to those configurations. Final configuration of Al-Al shows a higher negative value than that of Ni-Al, so Al-Al is the most favored final configuration.

To move the Cr atoms placed initially on Ni-Al sites to move to Al-Al or Ni-Ni sites, it is observed that the final configuration of Al-Al sites is favored, whereas Ni-Ni sites are not

favored because of the positive energy required. It is observed that if the two Cr atoms are initially sitting on Al-Al sites, they will prefer to stay there as the energy value needed to move to Ni-Ni or Ni-Al configurations are positive.

It can be concluded that the two Cr atoms favor to sit as close as possible on two Al sites. Any different configuration can lead to the final configuration of two Cr atoms sitting on first nearest neighbors of Al sites from the initial sites of two Ni sites or an adjacent Ni and Al sites.

#### 4.2.3.4. Interaction between Cr-Co atoms

The interaction energy between two dissimilar elements was calculated by substituting Cr and Co atom in the  $\text{Ni}_3\text{Al}$  3x3x3 supercell. Cr and Co were substituted in the Ni and Al sites in order to make all four possible combinations of sites (i.e. Ni-Ni, Ni-Al, Al-Ni and Al-Al). The atoms were substituted in the first, second and third nearest neighbors of the sites. When the Cr and Co were substituted in Al-Al sites, they prefer to stay away from each other. When the Cr and Co were substituted in any other site combination of Ni-Ni, Ni-Al or Al-Ni, they prefer to stay as close to each other as possible.

The interaction energy between Cr and Co substitutions in  $\text{Ni}_3\text{Al}$  is investigated by calculating the energy required to move the Cr and Co from its initial configuration of Ni-Ni, Ni-Al, Al-Ni and Al-Al sites to similar final configuration. The final configuration of Al-Ni site looks the most stable owing to the negative value of the factor. Whereas, the greater than zero value of factor for Al-Al and Ni-Al sites will not be possible for final configuration.

The energy to move the Cr and Co atoms from initial configuration of Ni-Al site to final configuration suggests that the initial configuration of first nearest neighbors in Ni-Al site leads to first nearest neighbors of Cr in Al and Co in Ni site or both elements in second nearest neighbors in Al site as final configuration, owing to the negative value of factor. Initial configuration of Ni-Al is the most unstable configuration as all other final configurations of Ni-Ni, Al-Al or Al-Ni site show negative value of factors. The energy to move the Cr and Co atom from initial configuration of Al-Al and Al-Ni sites to final configurations suggests if the initial site of Cr and Co is Al-Al sites, then it is the most stable configuration due to the greater than zero value of factor for all other final configurations. The initial site of Cr and Co in Al-Ni is also the most stable configuration as all other final configurations show greater than zero value of factor.

More details of the work can be found in [Chaudhari et.al. (2013)]

#### 4.2.4. Task D: Mechanisms of refined scale intra-granular precipitation in titanium alloys

##### 4.2.4.1. Non-classical Homogeneous Precipitation Mediated by Compositional Fluctuations in Titanium Alloys

This work presents experimental evidence of homogeneous precipitation of the  $\alpha$  phase within the  $\beta$  matrix of a titanium alloy, in this case commercial T-5553 (Ti-8.8Al-2.4Mo-4.7V-2.7Cr-0.4Fe in wt%), and then accounts for this phase transformation by a new, non-classical, mechanism involving compositional fluctuations, based on the pseudo-spinodal concept [Ni and Khachaturyan (2009)]. This mechanism involves local compositional fluctuations of small amplitude which, when of a certain magnitude, can favor thermodynamically certain regions of the  $\beta$  matrix to transform congruently to the  $\alpha$  phase but with compositions far-from equilibrium. Subsequently, as measured experimentally using the tomographical atom probe, continuous diffusional partitioning between the parent  $\beta$  and product  $\alpha$  phases during isothermal annealing drives their compositions towards equilibrium. For a given alloy composition, the decomposition mechanism is strongly temperature dependent which would be expected for homogeneous precipitation via the compositional fluctuation-mediated mechanism but not necessarily for one based on classical nucleation theory. The applicability of this mechanism to phase transformations in general is noted.

###### 4.2.4.1.1. Determination of the characteristics of the phase transformation

Given the fact that a refined dispersion of the  $\alpha$  phase can form in a matrix of  $\beta$  in the absence of previously claimed heterogeneous nucleating agents, it is necessary to fully characterize the observed transformation. This is done in the following.

###### 4.2.4.1.2. Temperature dependence of the transformation

In samples that have been step-quenched and annealed at 700 °C for 30 minutes, the microstructure consists of precipitation of grain boundary  $\alpha$  allotriomorphs at the  $\beta$  grain boundaries with some Widmanstätten  $\alpha$  laths growing from the grain boundary allotriomorphs into the adjacent  $\beta$  grains. It was found that these  $\alpha$  laths do not always grow on both sides of the grain boundary. Such preferential nucleation and growth of Widmanstätten  $\alpha$  laths, and their corresponding orientation relationships with the  $\beta$  grains has been discussed previously in case of  $\alpha/\beta$  Titanium alloys [Bhattacharyya et.al. (2003)]. In samples milled orthogonal to the sample surface using a DB-FIB instrument, it has been revealed that these laths do not connect with grain boundaries existing beneath the sample surface, suggesting that the precipitates are intragranular in nature.

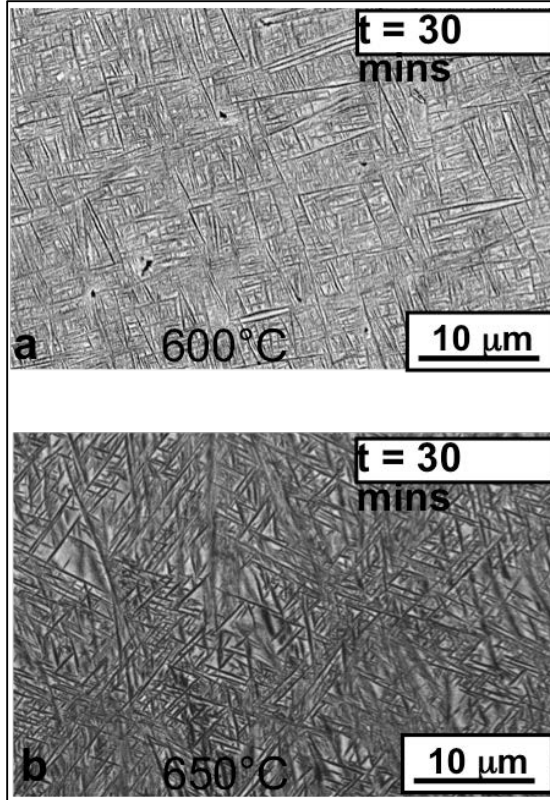


**Figure 3:** Low magnification SEM backscattered images of similar heat treatment at (a) 600 °C and (b) 650 °C with the annealing time being 30 minutes where similar high density of intragranular  $\alpha$  precipitation is observed.

Fig. 3 (a) shows the result of step-quenching a sample of Ti-5553 to 600 °C followed by a hold at that temperature for 30 minutes. It is clear that a significantly finer distribution of the  $\alpha$  phase has resulted, implying a markedly increased nucleation rate over that associated with precipitation at 700 °C. The volume fraction of  $\alpha$  that has formed is also much increased over that observed following step-quenching to 700 °C, confirming an increased kinetics of transformation. While a higher degree of undercooling can result in an increased driving force for nucleation, the observed change in the  $\alpha$  volume fraction and morphology is too sudden to be explained simply based on this argument. This abrupt change in the nucleation rate implies that the transformation mechanism is characterized by very significant temperature dependence. To explore this further, samples were step-quenched from above the  $\beta$  transus to 650 °C, and again held at that temperature for 30 minutes. The result is shown in Fig. 3 (b), and it is clear that the nucleation rate is again significantly higher than that for transformation at 700 °C, although the temperature difference is only 50 °C, and similar to that for transformation at 600 °C. Based on these experimental results, there appears to be a substantial difference between the morphology and size scale of  $\alpha$  precipitates, number density of nucleation sites, and, the kinetics of  $\alpha$  precipitation, between the annealing temperatures of on the one hand 700 °C, and on the other hand 650 °C and 600 °C, after step-quenching from 1000 °C (well above the  $\beta$  transus).

#### 4.2.4.1.3. Mechanism of intragranular $\alpha$ precipitation in Ti-5553 during isothermal annealing

From the experimental work described above, the following are the salient features of the precipitation of the  $\alpha$  phase in a matrix of  $\beta$ :

1. A refined dispersion of  $\alpha$  in  $\beta$  can be effected by heat-treatment at 600 °C and 650 °C in the absence of previously claimed heterogeneous nucleation sites (i.e.,  $\beta$  phase separation and the presence of the  $\omega$  phase). No other obvious heterogeneous nucleation pathways were identified.
2. There is a very significant temperature dependence associated with the phase transformation such that over a 50 °C temperature decrease in the holding temperature following step-quenching from above the  $\beta$  transus, the nucleation rate jumps by several orders of magnitude, as evidenced by the heat-treatments at 700 °C and 650 °C.
3. The precipitating phase appears to form with its thermodynamically stable crystal structure, i.e., *hcp*.
4. The precipitating phase forms with an initial composition that is far from equilibrium, and during subsequent thermal exposure, diffusion provides for a continuous change in the compositions of the  $\alpha$  and  $\beta$  phases towards equilibrium values.

Based on the first of these features, it appears that the phase transformation involves a mechanism of homogeneous precipitation, and does not take advantage of any heterogeneous nucleation sites. The second feature, involving strong temperature dependence, is very difficult to understand in terms of classical nucleation theory. Thus, the abrupt increase in nucleation activity with only a small decrease in temperature (50 °C) is not consistent with the increase in nucleation rate expected from undercooling [Porter and Easterling (1981)]. The third feature appears to suggest that the phase transformation does not occur via metastable structures, or pathways involving metastable phases. Finally, the fourth feature again is difficult to understand in terms of classical nucleation theory, which would suggest that the nucleus would have a composition at or very close to equilibrium [Porter and Easterling (1981)]. In the following, a new transformation mechanism is described which is indeed non-classical and whose features are consistent with those discussed above.

The proposed precipitation mechanism is based on the occurrence of small compositional fluctuations that under certain conditions render regions of a single phase unstable against a phase transition to a second phase. This mechanism has been inspired by the pseudospinodal decomposition concept that was recently proposed by Ni and Khachaturyan [Ni and Khachaturyan (2008)] to account for “tweed” microstructures. The mechanism of the pseudospinodal involves the homogeneous decomposition of a parent phase via small compositional fluctuations leading to either the solute-depleted or solute-rich regions transforming to a product phase of a different symmetry. The basic principle of pseudospinodal decomposition lies in the simple concept that if the nominal composition of the parent phase lies near the intersection point of the free energy–composition (G-X) curves for both parent and product phases (referred to as the  $c_0(T)$  point for that particular temperature), on the side where the free energy of the parent phase is lower than that of the product phase, then it is feasible that small compositional fluctuations will drive the composition of certain regions of the parent phase to the opposite side of the  $c_0(T)$  point. The system can reduce its energy by transforming these regions to the product phase.

In the case of the present study, the  $c_0(T)$  points have been considered for two different temperatures, namely 700 °C where the nucleation rate is low and the scale of the distribution of precipitates is rather coarse, and 600 °C where the nucleation rate is extremely high, and a very refined distribution of precipitates results. With decreasing temperature, the  $c_0(T)$  point approaches closer to the nominal alloy composition ( $C_{alloy}$ ). Presumably at 700 °C, the nominal alloy composition ( $C_{alloy}$ ) lies quite far in composition from the  $c_0(T)$  point. Consequently, only relatively large compositional fluctuations within the  $\beta$  would be able to drive the matrix composition to the other side of  $c_0(T)$  where the formation of  $\alpha$  would be favorable. It is expected that such a large compositional change would only be a rare event at 700 °C, and hence would lead to low nucleation rates and coarse  $\alpha$  precipitation. At a lower temperature such as 600 °C, the relative positions of the free energy curves for the two phases change, and the nominal alloy composition ( $C_{alloy}$ ), may now lie very close to  $c_0(T)$ . Small compositional fluctuations within the  $\beta$  matrix would then easily drive regions to the other side of the  $c_0(T)$  point making them favorable to transform into  $\alpha$ .

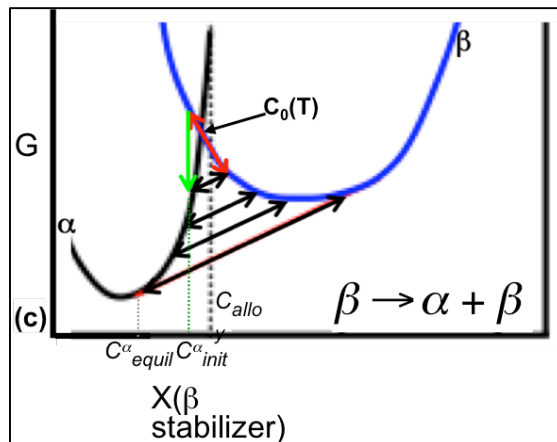


**Figure 4:** Schematic Gibbs free energy versus composition (G-X) plots for the  $\beta$  and  $\alpha$  phases in case of the present study where at 600 °C the  $c_0(T)$  point is close to the nominal alloy composition ( $X_0$ ). The red arrow indicates the range of possible compositional fluctuations. The green arrow indicates that, for fluctuations that cause the local composition to be less than the  $c_0(T)$  point, transformation from the  $\beta$  phase directly to the  $\alpha$  phase would be favorable.

The phase transformation mechanism is summarized in Fig. 4. Thus, the alloy composition, marked  $C_{alloy}$  in the figure, lies close to  $c_0(T)$ , such that a small compositional fluctuation, shown in red in the figure, may result in regions of the  $\beta$  phase having compositions on the solute lean side of  $c_0(T)$ . These solute lean  $\beta$  phase regions will have a driving force for direct transformation to the  $\alpha$  phase of the same composition (congruent transformation), the pathway shown in green in the figure. The activation barrier corresponding to this congruent transformation of the solute-lean  $\beta$  pockets to  $\alpha$  is presently not known and will be the subject of future computational studies. The composition of the precipitated  $\alpha$  phase would be  $C_{init}^\alpha$ , i.e., the same as that provided by the small compositional fluctuation and therefore far from equilibrium, i.e.,  $C_{equil}^\alpha$ . Continued thermal exposure at the temperature of precipitation would be

accompanied by diffusion of solute such that the compositions of the  $\alpha$  and  $\beta$  phases would continually change towards equilibrium.

This proposed mechanism is consistent with the four points listed above that characterize the phase transformation. Thus, regarding point #1, the underlying concept, i.e., compositional fluctuations, is intrinsic to the given alloy system at temperatures where diffusion is appreciable, and does not involve heterogeneous pathways. Regarding point #2, there is a strong temperature dependence associated with the mechanism, such that nucleation will only occur if the alloy composition is within a small deviation from the given  $c_0(T)$ . For a given alloy, the difference between these two compositions is influenced by temperature (because the two free energy curves are relatively displaced with change in temperature). Regarding point #3, the transformation is directly from the  $\beta$  phase to the  $\alpha$  phase, and does not involve metastable pathways (see the green arrow in Fig. 4. Therefore, the equilibrium crystal structure is expected to form. Finally, regarding point #4, the composition of the precipitating phase is given by  $C^{\alpha}_{init}$ , and is therefore somewhat different from equilibrium, and with further heat-treatment, will continually change towards the equilibrium value.

The discussion presented above has been based on schematic G-X plots. The form of these plots is supported by versions derived from solution thermodynamic models used in the commercial programs Thermo-Calc and PANDAT [W. Cao 209, H. Lukas, S.G. Fries and B. Sundman 2007], if the Mo-equivalency [Boyer et.al. (1994)] is used to represent the composition of the alloy Ti-5553. The Mo-equivalency for the composition of the alloy Ti-5553 is  $\approx 9.0$ wt.% Mo; for the case of  $700^{\circ}\text{C}$ , there is a reasonable difference between the alloy composition and  $c_0(T)$ , whereas for the case of  $600^{\circ}\text{C}$ , these compositions are almost coincident. These calculations lend credence to the arguments made above using the schematic diagrams. More sophisticated assessments of these G-X plots, based on *ab-initio* first principles calculations, are the subject of further research.

The discussion above does not make reference to the physical mechanisms of the precipitation process. In the case of precipitation of refined distributions of  $\alpha$  in  $\beta$ -Ti, the Burgers orientation relationship between product and parent phases is observed, exhibiting an invariant line. Because of this, it is expected that the mechanisms of the transformation process will involve a displacive component. This is the subject of further research.

The proposed mechanism relies on compositional fluctuations that cause local variations such that pockets of the sample are thermodynamically favored to undergo a phase change from  $\beta$  to  $\alpha$ -Ti. For the computational assessment (Thermo-Calc), the  $c_0(T)$  values for  $700^{\circ}\text{C}$  and  $600^{\circ}\text{C}$  are 5.69wt%Mo and 8.83wt.%Mo. From fluctuation theory, it is known that the thermal fluctuations in composition may be approximated by a Gaussian probability distribution function [L. D. Landau and Lifshitz (1980)]. Landau and Lifshitz give the variance of this distribution in c as:

$$\langle(\Delta c)^2\rangle = \frac{1}{\beta} = \frac{T}{N\left(\frac{\partial\mu}{\partial c}\right)_{P,T}} \quad (4)$$

where T is temperature,  $\frac{\partial \mu}{\partial c_{P,T}}$  is the first derivative of the chemical potential with respect to c evaluated at constant pressure and temperature, and N is the amount of matter in the region being considered. Now assuming that the local average composition to be 4.0 at.% Mo, (based on the approximate Mo-equivalency of Ti-5553, ~9wt% Mo) and estimating other values such as the driving force for nucleation at different temperatures [Shim et.al. (1996)], and surface energy  $\gamma$ , the inverse of variance ( $\beta$ ) can be estimated. Thus the Gaussian probability density function is given by:

$$w(x) = \sqrt{\frac{\beta}{2\pi}} \exp\left(-\frac{1}{2}\beta(x - \bar{\mu})\right) \quad (5)$$

where  $\omega(x)$  is the probability of fluctuation around an average composition  $\mu=4$  at% ~ 9wt%. It appears that the maximum fluctuation in composition varies from  $\approx 3.8$ - $4.2$  at.% Mo for temperatures in the range 600-700 °C, i.e., a maximum fluctuation amplitude of about 0.4wt.% Mo from the average composition would be expected. At 700 °C the difference in composition between the  $c_0(T)$  point and the alloy is approximately 2wt.% Mo, and so the estimated compositional fluctuation would not be sufficient to permit the proposed mechanism to operate. In contrast, at 600 °C, the difference between the  $c_0(T)$  value and the average alloy composition (i.e., equivalency) is  $\approx 0.17$  wt% Mo, and so the fluctuations expected, 0.4wt% Mo, would be such as to promote the operation of the proposed mechanism. It is to be emphasized, as noted above, that the use of the Mo equivalent composition represents an approximation, and the results of the Thermo-Calc assessments also involve uncertainties, so this analysis is offered not as proof of the operation of the proposed mechanism, but points out that, using best estimates, the computational assessment, based on a binary simplification, is at least consistent with observations and the proposed model for non-classical nucleation.

As noted in the introduction, it is of interest to attempt to interpret the present observations on the basis of the model described by Menon and Aaronson [Menon and Aaronson (1986)]. The mechanism proposed by these authors (based on the monotectoid reaction), leads to a substantial difference between the compositions of the  $\beta$  phases (referred to as  $\beta_1$  (lean in beta stabilizers) and  $\beta_2$  (rich in beta stabilizers)), in equilibrium with the  $\alpha$  phase, when the alloy is annealed above versus below the monotectoid temperature, while the composition of the  $\alpha$  phases as nucleated are predicted to be close to equilibrium. With continued aging following nucleation, the composition of the  $\alpha$  phase would not be expected to change to any extent, whereas that of the  $\beta$  phase would be expected to change quite considerably (the transformation from  $\beta_1$  to  $\beta_2$  not being identified in [Menon and Aaronson (1986)]). In contrast, the pseudo-spinodal model, presented here, would predict that both phases would form with compositions far from equilibrium and they would both change in composition during subsequent aging until equilibrium would be reached. The experimental evidence presented in this paper supports the latter prediction, i.e., the composition of both phases changing with continued aging following nucleation of the  $\alpha$  phase. Hence, it is reasonable to conclude that the model presented in [Menon and Aaronson (1986)], while perhaps being useful in describing the formation of “black

plate”  $\alpha$  particles, is not relevant to the case of homogeneous precipitation studied in this paper. It is interesting to note that no direct measurements of phase composition were made in [Menon and Aaronson (1986)].

This mechanism is expected to apply to a more general group of alloys which exhibited extremely refined distributions of second phase(s), rather than be restricted to the present alloy system under discussion. For example, reference was made above to the lack of understanding of the homogeneous precipitation of ordered  $\gamma'$  (based on  $\text{Ni}_3\text{Al}$ ) in Ni-base superalloys. The relevance of the proposed non-classical mechanism of precipitation is being assessed in further research. It is reasonable to speculate that the proposed mechanism may be relevant to any potential phase transformation where the alloy composition is sufficiently close to the appropriate  $c_0(T)$  for the two phases (parent and product) involved in the given transformation at appropriate transformation temperatures.

This work describes the process of precipitation of the  $\alpha$  phase in a matrix of  $\beta$  titanium in the absence of potential heterogeneous nucleation agents (i.e., the  $\omega$  phase and  $\beta$  phase separation). A new mechanism for homogeneous precipitation is described, based on the pseudo-spinodal concept. Thus, the transformation is mediated by small compositional fluctuations in the  $\beta$ -phase when the alloy composition is sufficiently close in value to that of the  $c_0(T)$  for the two phases (parent and product). This mechanism accounts for all of the experimentally observed features of the transformation, including the marked temperature dependence exhibited by this transformation, a pathway leading to the direct formation of the equilibrium crystal structure, and the composition of the nucleated phase being far from equilibrium. It is suggested that this mechanism is generally applicable to a large number of transformations involving precipitation of a refined distribution of precipitates.

More details of the work can be found in [Nag et.al. (2012)]

#### *4.2.4.2. Pseudospinodal Mechanism for Fine $\alpha/\beta$ Microstructures in $\beta$ -Ti alloys*

The above mentioned experimental observations in Ti-5553 have demonstrated the formation of a dense population of fine intragranular alpha-Ti precipitates when the alloy is step-quenched below a critical temperature. These precipitates are associated with a sudden, significant increase in the apparent nucleation rate. We developed a computational model of alpha precipitation in Ti-alloys, via the phase field method, in order to investigate the fundamental cause of the observed microstructural changes. We simulated the nucleation of alpha phase in TiMo for a series of compositions and temperatures and qualitatively reproduced the experimental observations. These results are explained via a pseudospinodal nucleation mechanism: when the system is close enough to the critical point at which the alpha and beta phases have the same free energy, fluctuation assisted partitionless transformation from beta to alpha becomes the dominant precipitation pathway. Consequently a rapid increase in nucleation rate occurs, resulting in a fine distribution of numerous intragranular alpha precipitates.

#### 4.2.4.2.1 Model Development

Since the Ti5553 alloy investigated in the recent experimental study [Nag et.al. (2012)] is a complex, multicomponent commercial alloy, it may not be suitable for fundamental simulation studies because of the lack of fundamental thermodynamic data. There are, however, several well studied binary Ti alloys which retain the typical features of more complex Ti alloys such as Ti5553. Therefore in the current study we will restrict our investigation to the binary Ti-Mo – system that is often considered the prototypical  $\beta$ -stabilized Ti alloy.

#### 4.2.4.2.2 Free energy model

Construction of the model begins with expressions for the chemical free energy of the alloy system. Several such models of the CALPHAD type exist for the Ti-Mo system [T. M. Rogers 1988, J. L. Murray (ed.), Phase Diagrams of Binary Titanium Alloys 1987, Shim et.al. (1996)] and we employed the recent assessment by Shim *et al.* [Shim et.al. (1996)]. This specific assessment was chosen because it is the most recent work and it shows the presence of a miscibility gap in the  $\beta$ -phase. Some disagreement on this point exists in the literature, with several authors observing or predicting a miscibility gap in the binary Ti-X alloys [J. L. Murray (ed.), Phase Diagrams of Binary Titanium Alloys 1987, Furuhara et.al. (1998), Shim et.al. (1996), Ikematsu et.al. (1991)] while the others asserting any observations of spinodal in these alloys to be erroneous [L. Kaufman 1978, R. Prasad 1993, K. Santhy, 2010, I. Ansara, COST 507 1995]. A recent thermodynamic model which does not contain the miscibility gap is given by [Santhy and hari-Kumar (2010)]. With or without a miscibility gap, available thermodynamic models generally agree as to the equilibrium volume fractions of  $\alpha$  and  $\beta$ , but will differ in  $c_0$ ,  $T_0$ , and the equilibrium concentration of the  $\beta$  phase. We have chosen the work of Shim *et al.* [Shim et.al. 1996] in order to explore the possibility of the metastable equilibration proposed by [Menon and Aaronson(1986)] in a follow up paper.

From this work we derive expressions for the chemical free energy for the  $\alpha$  and  $\beta$  phases as function of composition and temperature:  $g_\alpha(c_{Mo}, T)$  and  $g_\beta(c_{Mo}, T)$ , respectively. The free energies of the  $\alpha$  and  $\beta$  phases from the assessment of Shim *et al.* [Shim et.al. 1996] We note that as temperature decreases,  $c_0$  increases (shifts towards the Mo-rich side).

Using these expressions, we may develop a free energy functional for the two phase system in terms of a set of phenomenological structural order parameters,  $\{\eta_i\}$ , that describe the spatial distribution of the  $\alpha$  and  $\beta$  phases:

$$F = \int_V \left[ \sum_p h(n_p) g_\alpha(c_{Mo}, T) + (1 - \sum_p h(n_p)) g_\beta(c_{Mo}, T) + w \sum_{p \neq q} n_p n_q + \frac{\kappa}{2} (\nabla c_{Mo})^2 + \frac{\kappa}{2} \sum_p (\nabla \eta_p)^2 \right] + E^{Elast} \quad (6)$$

where  $c_{Mo}$  is the concentration field,  $\eta_p$  is the structural order parameter of the  $p$ th  $\eta$  variant, i.e.,  $\eta_p = 1$  within the  $p$ th  $\alpha$  variant and  $\eta_p = 0$  within all the other  $\alpha$  variants as well as within the  $\beta$  phase, and  $h(\eta_p)$  is an interpolation function.

$$h(\eta) = \eta^3(6\eta^2 - 15\eta + 10) \quad (7)$$

which allows a smooth connection of the free energy curves as function of concentration alone in the dimension of the structural order parameters,  $w$  characterizes the hump height on the free energy surface across an  $\alpha/\alpha$  domain wall,  $\kappa$  and  $\epsilon$  are the gradient energy coefficients for concentration and structural order parameter, respectively, and  $E^{elast}$  is the coherency elastic strain energy.

The elastic energy is given by Khachaturyan-Shatalov theory as [ Khachaturyan (1983)]

$$E^{elast} = \int_V \sum_{pq}^{12} B_{pq}(\vec{n}) \tilde{\eta}_p(\vec{k}) \tilde{\eta}_q(\vec{k}) \quad (8)$$

where  $\int_V$  is an integral over reciprocal space (excluding a volume of  $(2\pi)^3/V$  around  $\vec{k}=0$ ).  $B_{pq}(\vec{n})$  is a function of the transformation strains of each  $\alpha$  variant. A necessary input for  $B_{pq}$  is the stress-free transformation strain,  $\epsilon_{ij}^T$ . Since we are interested in studying the early stages of nucleation, we make the assumption that  $\alpha$  is fully coherent with the parent matrix. Given this, the specific value of  $\epsilon_{ij}^T$  for the  $\beta$ -to- $\alpha$  may be derived from the Burgers orientation relationship [Burgers (1934)]. The specific strain tensor for each variant is then subsequently derived by symmetry operations; in the real system, there are 12 possible variants of  $\alpha$ .

#### 4.2.4.2.3. Kinetic equations

$$\frac{\partial x_{Mo}}{\partial t} = \nabla \left[ M(c_{Mo}) \nabla \frac{\delta F}{\delta c_{Mo}} \right] + \xi_c \quad (9)$$

$$\frac{\partial \eta_p}{\partial t} = -L \left[ \frac{\delta F}{\delta \eta_p} \right] + \xi_\eta \quad (10)$$

Evolution of the system is then governed by a set of coupled integro-differential equations. where  $M(c_{Mo}) = M[c_{Mo}(1 - c_{Mo})]$  is the chemical mobility of Mo,  $L$  is the structural mobility of the  $\eta$  fields, and  $\kappa_c$  and  $\kappa_\eta$  are Langevin force terms that simulate thermal fluctuations.

#### 4.2.4.2.4. Nucleation model

Several methods have been employed to simulate nucleation in the phase field model. These may broadly be classified as either explicit [Simmons et.al. (2000)] or Langevin force approaches [Rogers et.al. (1988)]. Even though it is practically impossible to reproduce nucleation rates with quantitative accuracy when using the Langevin force terms [Plapp et.al. (2010)], we have chosen this approach in our simulations. The reason for this choice is that, although it cannot

quantitatively reproduce the nucleation rates, it allows for nucleation to be produced via statistical sampling of the free energy landscape as a result of random fluctuations. Since we are interested in the effect that subtle variations in the position of the system on the free energy landscape have on nucleation rates, we have to employ a method that does not proscribe the transformation pathway. Consequently, in the simulations below we have arbitrarily chosen the magnitudes of  $\kappa_c$  and  $\kappa_\eta$  such that nucleation was observed in a reasonable period of wall-clock time. Although we cannot make quantitative comparisons between our simulations and experiment, the relative changes in nucleation as a function of composition and temperature may still provide insight into the behavior of the physical system

#### 4.2.4.2.5. Results and Discussion

We are specifically interested in examining the effect of pseudospinodal mechanism on the overall transformation kinetics. To this end, we perform a series of simulations in which precipitation processes in alloys with their compositions at various distances from  $c_0$  (i.e. at various values of  $\Delta c = c - c_0$ ) are studied. We can alter  $\Delta c$  either by directly changing alloy composition  $c$  or by changing the temperature (where, in our simulations, decreasing temperature will result in decreasing  $\Delta c$ ). Unless otherwise noted, all other parameters are held constant while changing either  $c$  or  $T$ . This includes those values which would otherwise vary with  $T$ , namely  $M$  and the magnitudes of  $\xi_c$  and  $\xi_\eta$ . By artificially holding these parameters constant, we may focus solely on the influence of the position of the system relative to  $c_0$ .

At each point in  $(\bar{c}, T)$ -space, we simulate nucleation via the Langevin force terms. Starting from an initially supersaturated homogeneous  $\beta$  phase, fluctuations via the Langevin force are introduced for a given period of dimensionless simulation time ( $t_n$ , varying as needed for each simulation). Once  $t_n$  has elapsed the noise terms are turned off, and the system is allowed to evolve further for 2.0 units of dimensionless time in order to eliminate any sub-critical fluctuations. At this point, any remaining nuclei are assumed to be supercritical (stable) and are counted directly. The dimensionless nucleation rate  $J^*$  is then estimated as

$$J = \frac{[\# \text{ of stable nuclei}]}{[\text{length of noise period}].[\text{volume of simulation cell}]} \quad (11)$$

Contributions from the coherency elastic energy will shift  $c_0$  toward the solute-lean side, increase the total energy barrier for nucleation, and affect the morphology of growing  $\alpha$  particles, which will make the calculation of  $\Delta c$  and hence the analysis of effects of alloy chemistry or temperature on the precipitation mechanism more difficult. Furthermore, the lath morphology which  $\alpha$  particles assume under the influence of elastic interaction renders particle counting difficult. For these reasons, most of the simulations were performed without the consideration of the elastic energy, but the simulation results should retain all the features necessary for the investigation of the effects of alloy chemistry and temperature on the precipitation mechanism.

At the end, we also show an example where the effect of the coherency elastic energy is included to demonstrate its effect on the overall morphology of the precipitates.

We construct two series of simulations in the  $(\bar{c}, T)$ -space, one with constant  $c$ , and one with constant  $T$ , which have decreasing values of  $\Delta c$ ). For each combination of  $c$  and  $T$  three simulations with computational cells of 512x512 were carried out in two-dimensions (2D), and the value of  $J^*$  were calculated by the procedure described above.

We observed a sharp increase in  $J^*$  as the system approached  $c_0$  - either by decreasing  $c$  or decreasing  $T$ . This was also evident in the resulting microstructures. While we emphasize that the Langevin force method employed in these simulations cannot give quantitatively accurate values of  $J^*$ , but it will reproduce qualitatively the effect of the free energy landscape on nucleation. The observed change in  $J^*$  is quite large, increasing by orders of magnitude when  $\Delta c$  decreases below 1%.

This increase in the apparent nucleation rate is out of proportion to the change which would be predicted by the classical nucleation theory (CNT). From the typical expressions for nucleation rate, we expect that the change in  $J^*$  should follow the proportionality [Simmons et.al. (2000)]

$$J^* = \exp\left(\frac{-\pi\gamma^2}{k_B T_f}\right) \quad (12)$$

in 2D, where  $\gamma$  is the  $\alpha/\beta$  interfacial energy,  $k_B$  is the Boltzmann's constant, and  $\Delta f$  is the bulk driving force for nucleation. While the CNT is widely recognized as an approximation, expressions derived from it have proven reasonable in predicting experimental observations [Ballufi(2005)]. Assuming that  $\gamma$  is constant, the CNT predicts that any changes in  $J^*$  may be explained by changes in  $T$  and  $\Delta f$ . Since we have held the magnitude of the Langevin force terms constant we should also assume that  $k_B T$  is constant - changes in temperature only affect the simulations by changing the local free energy landscape (moving  $c_0$ , and increasing or decreasing  $\Delta f$ ).

Given a free energy model, the maximum driving force for nucleation of  $\alpha$  from  $\beta$  can be estimated as

$$\Delta f = \left. \frac{\partial g_\beta(c)}{\partial x} \right|_{\bar{c}} (c_{eq}^\alpha - \bar{c}) + g_\beta(\bar{c}) - g_\alpha(c_{eq}^\alpha) \quad (13)$$

From the calculated values of  $\Delta f$ , the proportionality given above can be used to estimate the

expected relative nucleation rates. Using the thermodynamic assessment of Shim et al. [J. Shim 1996], we calculated the value of  $\Delta f$  for each simulation, and then compared the measured relative changes in  $J^*$  with what would be predicted using CNT and changes in  $\Delta f$  alone. For simulations holding temperature constant at 873 K, the change in  $\Delta f$  as  $c$  changes from 3.5% to 2.55% is small. Accordingly, the expected change in  $J^*$  is minimal in contrast to the observed rapid increase in the nucleation rate in these simulations. Nucleation driving force is more sensitive to temperature and the expected change in  $\Delta f$  between 900 K and 873 K is larger. However, the predicted increase in  $J^*$  for this case is still far smaller than what was observed in the simulations.

In order to confirm that this disagreement in trends is due to the proximity of alloy composition to  $c_0$ , we performed additional simulations at  $T = 900$ ,  $887$ , and  $873$  K with  $c = 7\%$ , much further away from  $c_0$ . We repeated simulations of nucleation at these three points using the same algorithm as before, though with increased noise magnitudes (nucleation rates in these conditions proved impractically slow using identical fluctuation magnitudes, so they were increased for computational efficiency). The agreement between the measured and predicted variation in  $J^*$  is observed and the difference between the measured and predicted changes in  $J^*$  is well within an order of magnitude in this case. This observation confirms that, when the system is far from  $c_0$ , our simulations behave roughly as what would be expected from the CNT

We can make a closer examination of stable and growing nuclei in two cases (near and far from  $c_0$ ) in order to highlight the differences in the typical nucleation process, using the following procedure. We chose two simulations as representatives of each case:  $T = 873$  and  $c^- = 2.45\%$  (near  $c_0$ ), and  $T = 873$  and  $c = 7.0\%$  (far from  $c_0$ ). Examining snapshots from the simulations, the locations of growing nuclei were identified at later simulation times. The evolution of each such nucleus was then followed backwards in simulation time to determine the earliest stable or "supercritical" configuration. We decided whether or not a given configuration was stable by extracting successively earlier snapshots, then simulating their evolution in the absence of Langevin noise. Those snapshots in which the nucleus continues to grow are deemed stable, and the earliest such stable snapshot is then used for the purpose of comparison. Note that a more rigorous and accurate method in determining a critical nucleus configuration in the phase field method is to use the nudged elastic band method or the mountain-climbing method.

The composition profile of two such early, stable nuclei configurations at  $c^- = 7.0\%$  and  $2.45\%$  is done. In the first case, the typical nucleus has a "classical" concentration profile, in which the concentration of the stable nucleus is relatively close to the equilibrium value, and its subsequent growth occurs via further rejection of solute into the  $\beta$  matrix at the interface. When  $c^- = 2.45\%$ , in contrast, the concentration profile of the stable nucleus is rather "non-classical", consisting of only a few contiguous points which are below  $c_0$ . Furthermore, the growth of this nucleus differs significantly from that in the previous case where the initial nucleus composition is far from the equilibrium and gradually approaches towards equilibrium ( $c^\alpha_{eq}$ ) as the nucleus grows, in a manner similar to concentration variation seen in spinodal decomposition. This process corresponds well to the pseudospinodal transformation mechanism described by Ni et al [Ni and Khachaturyan (2009)].

For identical noise magnitudes, it is plausible that the pseudospinodal mechanism would permit a significantly higher nucleation rate. Thermal fluctuations follow a Gaussian distribution, with small fluctuation being much more likely than large ones. Since the stable "nuclei" in the pseudospinodal mechanism require small concentration fluctuations, they effectively have a much higher probability of formation as a result. Thus, our simulations present compelling evidence that at least the changes in microstructure and nucleation rate reported by Nag et al. [Nag et.al. (2012)] could be explained via a pseudospinodal mechanism.

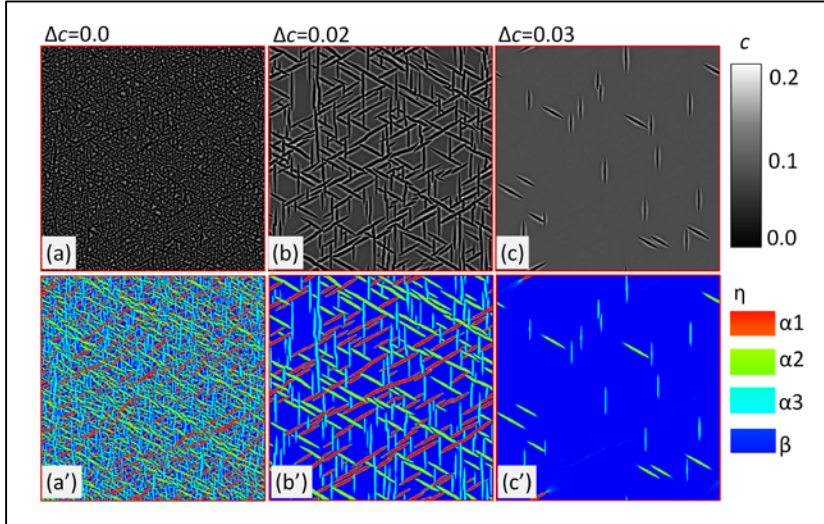


**Figure 5:** Calculated  $\alpha$  precipitates morphology with elastic energy at fixed temperature with different average composition  $\Delta c = 0.0, 0.02, 0.03$  ( $\Delta c = c - c_0$ ). (a) – (c) describe the composition field with different  $\Delta c$ , black color describes the low composition. (a') – (c') describe the structure field with different  $\Delta c$ , red, green and blue colors describe the three variants of  $\alpha$  precipitate, dark blue color describes the  $\beta$  phase.

The above simulations show that the nucleation rate depends on the distance of the average composition  $c$  from  $c_0$ , which is consistent with experimental observations. However the morphology of the  $\alpha$  precipitates obtained in the simulations are obviously quite different from those observed in experiments because the coherency elastic energy is ignored in the above simulations. Even though precipitate morphology is not the concern of the current study, we show in Fig. 12 the simulated  $\alpha$  precipitate morphology when the coherency elastic strain is considered.

Figs. 5 (a)-(c) show the composition fields (where the  $\alpha$  precipitates are shown as black), while Figs. 5 (a')-(c') show structural fields (where the red, green and light blue colors distinguish the three variants of the  $\alpha$  precipitate and the dark blue describes the  $\beta$  phase) at different values of  $\Delta c$ . When the average composition is at  $c_0$  ( $\Delta c = 0.0$ ) (Figs. 5 (a) and (a')) we observe a high density of refined  $\alpha$  precipitates. When the average composition is close to  $c_0$  ( $\Delta c = 0.02$ ) (Figs. 5 (b) and (b')) we observe a high density of larger  $\alpha$  precipitates with a typical triangular pattern due to the long-range elastic interactions. When the average composition is far from  $c_0$  ( $\Delta c = 0.03$ ), we observe a low density of  $\alpha$  precipitates, as homogenous nucleation becomes difficult. The change in the number of precipitates between  $\Delta c$  of 0.0 and 0.02 is roughly twice the change observed between  $\Delta c$  of 0.02 and 0.03. The calculated morphology of the  $\alpha$  precipitates agrees

well with experimental observations. These simulations also confirm that the density of  $\alpha$  precipitates depends sensitively on the distance of alloy composition from  $c_0$ .

#### 4.2.4.2.6. Conclusion

The simulations presented in this study demonstrate that a pseudospinodal transformation pathway could result in a sudden increase in the nucleation rate of  $\alpha$  in an  $\alpha/\beta$ -Ti alloy, far above what would be predicted by the classical nucleation theory (CNT). We have observed that this behavior is a function of the distance of the alloy composition from the  $c_0$  point in G-T -space: far from  $c_0$  the nucleation rate roughly follows the predictions of CNT, while close to  $c_0$  the nucleation rate increases far beyond what can be explained by the change in undercooling alone. This increase in  $J^*$  is associated with, and indeed explained by the transition from conventional nucleation and growth to a pseudospinodal mechanism. The simulation results suggest the strong possibility that the experimental observations of Nag *et al.* can best be explained by the activation of a pseudospinodal mechanism. This would explain the sudden increase in nucleation rate with only a small change in temperature (and thus driving force). It also presents a general mechanism by which fine precipitate microstructures could be generated in many other alloy systems.

### 4.2.5. Task E: Evaluation of the oxidation behavior of titanium alloys

#### 4.2.5.1. Influence of oxygen ingress on fine scale precipitation of $\alpha$ -Ti during oxidation of Beta21S, $\beta$ -Ti alloy

The formation of a surface oxide layer along with  $\alpha$  precipitation in the subsurface oxygen-enriched zone, during the oxidation of a  $\beta$ -Ti alloy, has been investigated using Scanning electron microscopy, Electron probe microanalysis, X-Ray diffraction, (Scanning) Transmission Electron Microscopy, 3D-Atom Probe studies and Nano-indentation. Immediately below the nanocrystalline oxide layer, a two-phase mixture consisting of nanoscale equiaxed  $\alpha$  grains and rutile grains is formed. With increasing depth, the  $\alpha$  morphology below the oxide layer varied from nanoscale equiaxed to lathlike, coupled with substantial changes in size-scale and nucleation density of  $\alpha$  precipitates. A distinct change in the lattice parameters of  $\alpha$  and  $\beta$  phases below the oxide layer and the overall micro hardness of the material is also noted. The role of oxygen ingress on the scale and morphology of  $\alpha$  precipitation has been discussed.

#### 4.2.5.1.1. Results and Discussion

In a cross section secondary electron (SE) image of an oxidized Beta 21s sample, a significant variation in the size-scale and nucleation density of the  $\alpha$  precipitates with distance from the oxide-alloy interface is observed. Large scale  $\alpha$  laths represent the bulk microstructure. On moving away from the oxide-alloy interface, the size of the  $\alpha$  precipitates decreases substantially. Near the oxide layer, the size of these laths is extremely fine ( $< 1 \mu\text{m}$ ).

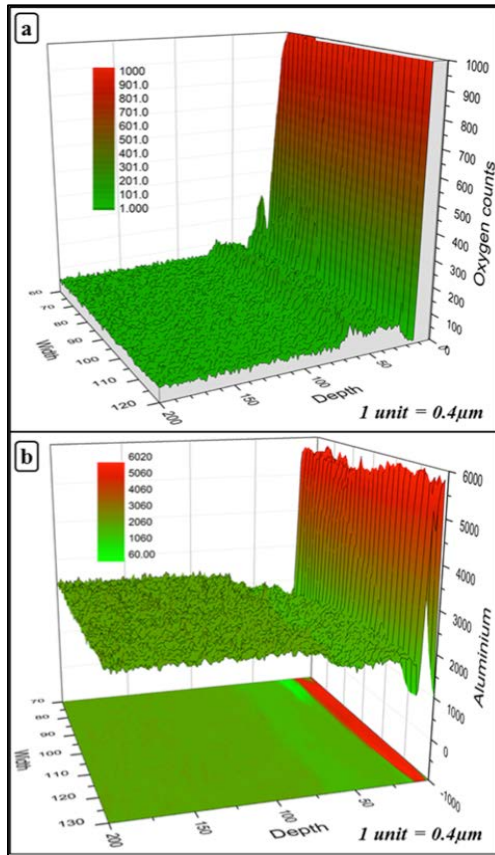


**Figure 6:** 3D surface plots mapping concentration distributions for a) Oxygen and b) Aluminum across the oxide–alloy interface using Electron probe micro-analyzer

Higher hardness values were observed near the oxide layer, where finer  $\alpha$  precipitates are present, as opposed to the values obtained far into the bulk of the specimen. Thus a typical hardness reading taken at  $5 \mu\text{m}$  from the oxide-alloy interface is  $\sim 8.5 \text{ GPa}$  while it is only  $\sim 5 \text{ GPa}$  at a distance of  $35 \mu\text{m}$  from this interface. The increase in the hardness values could be attributed to the finer size of  $\alpha$  precipitates and the presence of oxygen in the interstitial sites. Similar results were obtained by previous researchers, where the mechanical property values such as micro hardness and tensile strength of the alloy seemed to vary quite significantly with oxygen content [Guangjun et.al. (1999), Chaze et.al. (1987)]. Concentration of oxygen near the oxide alloy interface was measured using SEM-EDS operating at voltage of 15 keV. It shows the variation in oxygen counts measured from the oxide surface going into the matrix. The graph

shows higher amounts of oxygen count in the oxide region and a sharp decline with the curve flattening out at a distance of  $\sim 20 \mu\text{m}$ .

Electron probe micro-analysis (EPMA) was also used to create a 3D color map, shown in Figure 6 depicting oxygen concentration profile across the oxide-alloy interface. It shows sharp oxygen concentration gradient with clear enrichment of oxygen in the fine scale  $\alpha$  precipitation zone, up to a depth of  $\sim 25 \mu\text{m}$ . The depth of oxygen ingress matches well with the hardness result, which shows an oxygen concentration gradient as far as  $30 \mu\text{m}$  from the oxide-alloy interface. From the above observations it is evident that higher oxygen content corresponds to higher nucleation density of  $\alpha$  phase leading to finer  $\alpha$  precipitates. This could possibly be explained either due to the effect of oxygen, an  $\alpha$  stabilizer, on  $\beta$  transus temperature or its role in providing additional nucleation sites for  $\alpha$  precipitation. Figure 2(b) shows similar 3D color map along with its 2D projection for aluminum concentration distribution close to the oxide alloy interface. A clear depletion of aluminum in the oxygen-enriched region is observed from the EPMA concentration maps. The results also show enrichment of aluminum on the oxide surface, providing evidence of alumina formation. This could be further confirmed in subsequent TEM analysis. Reports of alumina at the oxide surface, owing to faster diffusivity of Al in Ti compared to other alloying additions as well as higher driving force for Al to oxidize, have been previously documented even for alloys having low Al concentration [Guangjun et.al (1999), Wallace (1993)].

X-ray diffraction patterns were obtained from bulk matrix of the alloy and the oxide surface revealing  $\alpha$  and  $\beta$  phases showed peaks corresponding to rutile ( $\text{TiO}_2$ ). The scans were intentionally conducted in Bragg Brentano theta-theta setup mode to include intensity peaks from subsurface layers beneath the oxide. On careful comparison between the bulk and oxide patterns one can note the relative shift of intensity peaks for both  $\alpha$  and  $\beta$  phases due to oxidation. In comparison to the bulk matrix, intensity maxima's for  $\alpha$  phase in the oxide surface seem to be shifted towards lower 2-theta angles. This could be due to oxygen dissolution in the subsurface layers that leads to an increase in the lattice parameter of  $\alpha$  phase, by occupying a fraction of the octahedral interstitial sites. In contrast, intensity peaks for  $\beta$  phase seem to shift towards higher 2-theta angles in the x-ray diffraction plot of the oxide surface. This shift may be interpreted in a way that during the oxidation process, oxygen an  $\alpha$  stabilizer, drives towards precipitation of fine scale  $\alpha$ . This increases the volume fraction of  $\alpha$ , consequently enriching the  $\beta$  phase in  $\beta$ -stabilizing alloying elements like Mo and Nb. As both these elements have smaller atomic radius than Ti, an increased amount of these elements results in a decrease of  $\beta$  phase lattice parameter, thus shifting the corresponding peaks to higher 2-theta values. The lattice parameter changes, as tabulated in the Fig. 3, clearly shows that oxygen ingress in  $\alpha$  phase results in an increase of both 'a' and 'c' lattice parameters. However the lattice parameter in the 'c' direction increases to a larger extent, thus increasing the  $c/a$  ratio, similar to previous synchrotron based studies [Malinov et al. (2002)]. A difference in the angular shift is observed for different peaks of  $\alpha$  phase. The shift in case of [0002] peak of  $\alpha$  phase is seen to be markedly more than the shift for [10-10] $\alpha$  peak. Similarly, the peak shift for [10-12] $\alpha$  is more than [11-20] $\alpha$ . Thus it can be concluded that angular shifts of peak intensities is higher for basal and pyramidal planes compared to prismatic planes. The increase in lattice parameter in the 'c' direction is greater than those in 'a' or 'c+a' directions. This could be due to the interstitial oxygen atoms that occupy the octahedral sites of HCP  $\alpha$ , resulting in a non-uniform change in lattice parameters (c and a values).

The variation of lattice parameter for  $\alpha$ -Ti with oxygen content has been previously reported in literature [Boyer et.al.(1994), Thyne et.al. (1952)]. The pronounced increase in lattice parameter in the ‘c’ direction is also noted. The lattice parameter of  $\alpha$ -Ti in the ‘c’ direction increases from 4.68 Å to 4.82 Å with an increase in oxygen content from 0 to 40at%. In the present study an oxygen content of about 20-25 at% could be estimated in the oxygen enriched  $\alpha$  case layer, underneath the oxide layer. The variation of lattice parameter for  $\beta$ -Ti phase with Mo content, has been previously reported in case of the Beta III (Ti-11.5Mo-6Zr-4.5Sn wt%) alloy [Boyer et.al.(1994), ]. The  $\beta$  lattice parameter was shown to decrease by about 0.02Å for a 6 wt% increase in the Mo concentration in the  $\beta$  phase. In the present study, the observed  $\beta$  phase lattice parameter decrease of 0.03 Å after oxidation can therefore be attributed to a Mo enrichment of approximately 8 wt%.

Atom probe studies were performed on site-specific lift-out samples to compare the compositional partitioning between  $\alpha$  and  $\beta$  phases. Two sites were chosen; one in the oxygen enriched case layer (at a distance of 5  $\mu\text{m}$  from the oxide layer/case layer interface) and the other in the bulk matrix. Proximity histograms depicting compositional partitioning averaged over the entire  $\alpha/\beta$  interface, along with the actual 3D reconstructed volume, show molybdenum enrichment (from 15 at% to 19 at%) in the  $\beta$  phase of the oxygen enriched case layer when compared with the  $\beta$  phase in the bulk matrix. This could be presumably due to a lower volume fraction of the  $\beta$ -phase in the case layer as discussed previously in this paper. Also a higher oxygen concentration (8 at%) in the  $\alpha$  phase of the fine scale alpha precipitated region within the case layer was measured, which is in qualitative agreement with the predictions afforded by the lattice parameter measurements from x-ray diffraction, discussed previously. The slight difference between the oxygen concentration values calculated from the lattice parameter measurements versus those measured directly from the atom probe experiments can be rationalized based on the fact that the atom probe studies correspond to samples extracted at a distance of 5  $\mu\text{m}$  from the oxide-case layer interface, while the x-ray diffraction results correspond to an average  $\alpha$  lattice parameter very near to the same interface (within  $\sim 1 \mu\text{m}$ ). Consequently the measured oxygen concentration in  $\alpha$  from the atom probe results is a little lower than those calculated from the x-ray diffraction lattice parameters. The vertical bars marked on each of the plots signify the statistical error associated with the measurement of a certain atom type. This is proportional to the inverse square root of the total number of atoms collected for that particular specie.

A scanning transmission electron microscopy (STEM) image that illustrates the change in microstructure, starting from the oxide layer on the top to about 10  $\mu\text{m}$  deep into the specimen reveal the entire oxidized sample can be roughly divided into distinct layers. The oxide region, the region of fine scale distribution of seemingly equiaxed  $\alpha$  grains, and the two the regions where the  $\alpha$  precipitates seem to exhibit more lath-like morphology ( $\sim 50$ -100 nm, and  $\sim 2$ -3  $\mu\text{m}$  in length), representing bulk microstructure. A bright field TEM micrograph of the oxide layer shows large number of nanocrystalline oxide grains, with an average grain size of  $\sim 20$  nm. A random orientation of these grains was clearly evident from the rings that were present in the selected area diffraction (SAD) pattern. Most of the rings could be indexed consistently based on either rutile ( $\text{TiO}_2$ ) or alumina ( $\text{Al}_2\text{O}_3$ ) phases. Similar study conducted on nanoscale equiaxed grains reveal the average grain size can be estimated to be  $\sim 50$ -100 nm. The corresponding SAD

pattern can be consistently indexed as  $<10-10> \alpha$ . The SAD pattern corresponding to this entire layer could be consistently indexed as either  $\alpha$ -Ti or rutile ( $TiO_2$ ) phases. The electron diffraction results indicate that this layer consists of a two-phase mixture. However, it is difficult to state with certainty that no  $\beta$  phase was present between the equiaxed  $\alpha$  grains. Also, there seems to be a six fold symmetry in the intensity rings corresponding to hexagonal closed packed structure of  $\alpha$ -Ti phase. This indicates the presence of a texture within the equiaxed  $\alpha$  grains, which is a subject of further investigation.

In this study, the influence of oxygen diffusion on the microstructure and hardness of oxide and oxygen-enriched regions in an oxidized  $\beta$ -Ti alloy has been investigated. Overall the experimental observations can be summarized as follows:

1. Oxidation of  $\beta$  solutionized and water quenched samples of Beta 21S, leads to fine scale  $\alpha$  precipitation next to the oxide layer (layer 1). The oxygen enriched case layer right below the oxide layer comprises of a two-phase mixture of rutile ( $TiO_2$ ) and fine scale equiaxed  $\alpha$  grains (layer 2).
2. With further increase in depth, due to oxygen ingress, a substantial gradient in  $\alpha$  size and nucleation density can be observed, starting with fine scale lath-like  $\alpha$  (layer 3) which slowly transitions into coarser  $\alpha$  laths (layer 4) in the bulk matrix. The observed microstructural changes could be directly attributed to the presence of oxygen gradient, as confirmed by EPMA and SEM-EDS studies.
3. Within the oxygen-enriched layer, there is an increase in the lattice parameters of  $\alpha$  phase as well as the 'c/a' ratio. In contrast, the lattice parameter of  $\beta$  phase within the same region decreases due to the enrichment of Mo and Nb, elements that have smaller atomic radii than Ti.
4. Atom probe studies show quantitatively the enrichment of Mo in the  $\beta$  phase and oxygen in  $\alpha$  phase, within the oxygen enriched  $\alpha$  case layer close to the oxide layer. Oxygen being an  $\alpha$  stabilizer, almost entirely partitions to the  $\alpha$  phase as evident from these observations. The observed enrichment in Mo and oxygen concentrations matches quite well with estimated values mentioned in previously published literature.
5. The microstructural changes appear to have a significant influence on the mechanical properties of these layers, as evident from nano-indentation results.

#### 4.2.5.1.2. Conclusions

Based on these experimental observations, possible mechanisms influencing  $\alpha$  precipitation due to the ingress of oxygen during oxidation of Beta 21S can be postulated. In addition to oxygen ingress, formation of a mixed two-phase region consisting of  $\alpha + TiO_2$  (Rutile) right next to the oxide layer, where the  $\alpha$  precipitates tend to exhibit a near-equiaxed morphology, is also noted. This ingress of oxygen, an  $\alpha$  stabilizer, creates a concentration gradient of it across the oxide-alloy interface which consequently results in a systematically decreasing  $\beta$  transus temperature from the region adjacent to the oxide layer into the bulk alloy. Effect of oxygen on  $\beta$  transus temperature for alloys such as Ti-6Al-4V has previously been shown by researchers [R. Boyer, G. Welsch, E.W. Collings (Eds.), 1994]. Furthermore, it should be noted that the  $\beta$  transus

temperature could be substantially higher than the bulk at regions closer to the oxide layer. This gradient in the local  $\beta$  transus temperature leads to a systematically changing undercooling with the regions adjacent to the oxide layer experiencing the highest undercooling for a constant overall annealing temperature (650 °C in this case). Consequently, based on classical nucleation theory the  $\alpha$  nucleation rate and spatial density will be much higher in the oxygen-enriched region leading to finer scale precipitates. Additionally, the possible clustering of oxygen or complexes such as carbon-oxygen atoms within the  $\beta$  matrix can potentially act as  $\alpha$  nucleation sites as discussed by others [Li et.al. (1999), Imam et.al. (1997)]. However, such clustering has not yet been directly experimentally verified and needs further investigation.

#### **4.2.6. Task F: Development of models of nucleation associated with solid-solid phase transformations in titanium and nickel base alloys**

##### *4.2.6.1. Nucleation of second phases in Titanium Alloys*

In this work we provide direct experimental evidence of the formation of embryonic omega from competing compositional and structural instabilities arising in the body-centered cubic (*bcc*) lattice of titanium-molybdenum alloys during rapid quenching. The partial collapse of the {111} planes within phase-separated regions of the *bcc* phase, containing marginally lower amounts of molybdenum, forming embryos of the omega phase, has been conclusively shown by coupling aberration-corrected high-resolution scanning transmission electron microscopy with three-dimensional atom probe observations.

###### *4.2.6.1.1. Results and Discussion*

Well-developed  $\omega$  precipitates of size 30 – 50 nm are clearly visible in the dark-field TEM image from the Ti-9at%Mo sample that was  $\beta$  solutionized (at 1000 °C), quenched, and then isothermally annealed for 30 mins at 475 °C. Such displacement of atomic columns within the *bcc* phase, equivalent to the collapse of the {111}  $\beta$  planes, leading to the formation of  $\omega$  phase, has been discussed in great detail in previous literature [Banerjee Mukhopadhyay (2004), Fontaine (1971), Williams (1973)]. The fully developed  $\omega$  structure, at atomic resolution, is clearly visible in the high-resolution TEM image from the 475 °C annealed Ti-9at%Mo sample. The same sample has also been analyzed using 3D atom probe and the compositional partitioning of Mo across the  $\beta/\omega$  interface shows large difference between the Mo contents of the  $\beta$  (~12at%) and the  $\omega$  (~4-5at%) regions.

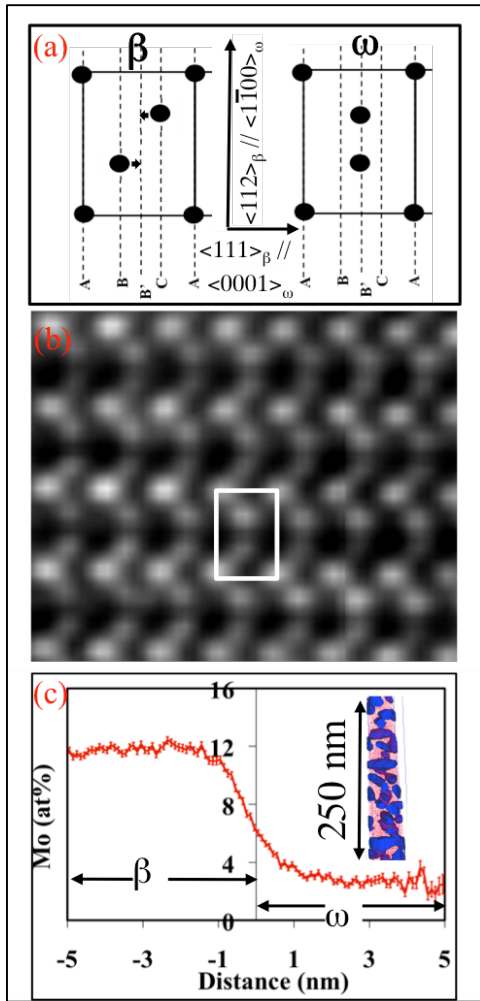


**Figure 7:** (a) Schematic arrangement of atoms as seen from the  $\langle 110 \rangle_\beta$  zone axis, corresponding to the  $\beta$  and fully collapsed  $\omega$  motifs. Small arrows show the shifts of atoms along  $\langle 111 \rangle_\beta$  directions. (b) HRTEM image recorded along the  $\langle 011 \rangle_\beta$  zone axis, in a 748 K/30 min aged Ti-9 at.% Mo sample, showing the collapse in atomic columns corresponding to the well-developed  $\omega$  phase. (c) Proximity histogram using  $\text{Ti} = 93$  at. % isosurface that shows substantial compositional partitioning between the  $\beta$  and  $\omega$  phases. The inset shows the corresponding 3DAP reconstruction of the Ti-rich regions.

High-resolution HAADF-STEM image from the rapidly cooled Ti-9at%Mo sample exhibits regions of relatively brighter and darker contrast indicative of differences in atomic masses between these regions (Z-contrast). In some cases the darker regions (lower Z) clearly exhibit shifts in the atomic columns corresponding to the nanoscale embryos of the  $\omega$  phase. An atom probe proximity histogram clearly shows that there is Mo partitioning across this interface with  $5.5 \pm 0.11$  at% and  $10.5 \pm 0.47$  at% Mo in the solute-depleted and solute-rich regions respectively.

Enlarged HAADF-HRSTEM images exhibiting the un-displaced and partially displaced atomic columns within the  $\beta$  matrix and an  $\omega$  embryo respectively were analyzed by intensity measurement of atomic columns along straight lines. The collapse of the  $\{111\}$  planes can be described as a displacement wave with a wavelength  $\lambda = 3d_{222}$  with the corresponding wave vector being  $2/3 <111>^*$  (reciprocal space) [D. De Fontaine 1970, D. De Fontaine 1973]. Based on this formalism, complete  $\beta$  to  $\omega$  transformation will correspond to a longitudinal displacement wave with an amplitude equaling  $0.5d_{222}$ . Consequently, the partial collapse of the  $\{111\}$  planes, observed in the present case, indicates smaller amplitude of the displacement wave as compared to that required for full collapse. The displacements of the atomic columns have been calculated to be in the range  $0.16d_{222}$  -  $0.2d_{222}$ , progressively increasing on moving from  $\beta$  to  $\omega$  region).

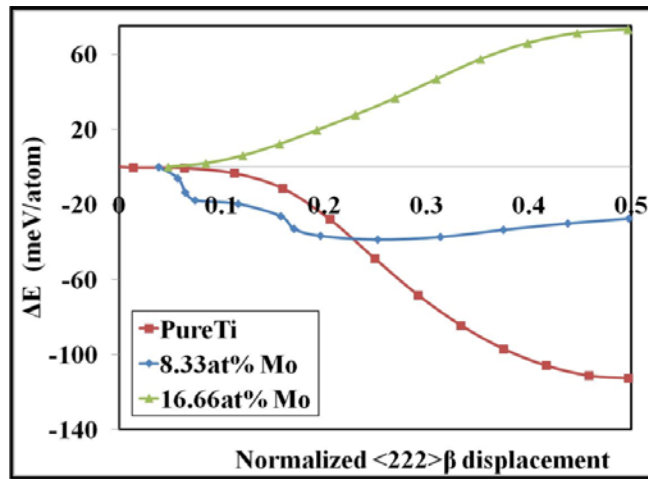


**Figure 8:** Nudged elastic band (NEB) results plotted for 24 atom supercell systems with 0at.%, 8.33at.%, and 16.66at.% Mo in Ti. E is relative energy of the system along the minimum energy path with  $\beta$  phase taken as reference. On the x-axis we have average coordinate of the collapsing  $\{111\}$  planes normalized by their inter-planar spacing.

Systems with 0, 8.33, and 16.66 at.% Mo in Ti were studied by DFT. Molybdenum atoms were added on collapsing  $\{111\}$  planes of  $\beta$  and  $\omega$  titanium and these structures relaxed by using Vienna ab initio simulation package (VASP). While there is no activation barrier for  $\beta$  to  $\omega$  transformation in the pure Ti system, we see a local energy minimum for the Ti-8.3 at.% Mo system along the minimum energy pathway corresponding to an average partial collapse of (222) planes (Fig 8). The normalized interplanar spacing for this local minimum structure is 0.25 from nudged elastic band calculations, in agreement with the experimental value of 0.20. Interestingly,  $<111>$  atom columns with a Mo atom do not collapse while a neighboring parallel  $<111>$  column with Ti does so. Such a partially collapsed structure is energetically favored over a fully collapsed structure when we have Mo atoms in the cell. For full collapse to occur Mo atoms must diffuse out of the omega region.

Based on these experimental observations a mechanism for the formation for embryonic  $\omega$  within the bcc  $\beta$  matrix can be proposed. Thus, during rapid quenching of the Ti-Mo alloy from

the high temperature single  $\beta$  phase field, the compositional instability within the bcc matrix manifests itself via compositional clustering (phase separation) into nanoscale Mo-enriched and Mo-depleted regions, presumably by a second order spinodal process. The rapid cooling rates involved limit the diffusion of Mo. Subsequently, a structural instability manifests within the Mo-depleted regions, where it is energetically favorable, resulting in initiation of collapse of the  $\{111\}$  bcc planes forming embryonic  $\omega$  regions. An undercooled alloy of composition Ti-9Mo presumably has a free energy lying within the miscibility gap (also within the spinodal) of the  $\beta$  phase, and consequently is unstable to compositional fluctuations. As these compositional fluctuations grow in amplitude and wavelength, eventually the solute (Mo) depleted regions within the  $\beta$  phase cross the point of intersection of the  $\beta$  and  $\omega$  free energy curves. These solute-depleted regions now become metastable (or unstable) with respect to the structural instability causing the partial collapse of the  $\{111\}$  beta planes leading to the formation of  $\omega$  embryos.

Summarizing, coupling aberration-corrected HAADF-STEM with atom probe tomography and density functional theory calculations, the early stages of phase separation (compositional clustering) and consequent displacive collapse of  $\{111\}$  bcc planes within the solute-depleted regions of the  $\beta$  matrix of Ti-Mo alloys have been established. These results provide novel insights into the mechanisms of solid-state transformations in metallic systems by capturing the earliest stages of nucleation at atomic to near atomic spatial and compositional resolution.

#### 4.2.6.2. Nucleation of $\gamma'$ in Nickel Base Alloys

This paper focuses on developing a mechanistic understanding of the process of multiple nucleation bursts leading to the formation of multiple generations (or populations) of  $\gamma'$  precipitates with different size distributions, during the continuous cooling of a commercially used nickel base superalloy. This mechanistic understanding has been developed based on a number of critical experimental results; direct observation of the multiple nucleation bursts during in situ x-ray diffraction studies in the synchrotron, characterization of the size distributions associated with the different populations of  $\gamma'$  precipitates by coupling multiple imaging techniques at the appropriate length scale, and detailed compositional analysis of the  $\gamma'$  precipitates as well as the  $\gamma$  matrix using atom probe tomography. These analyses reveal that while local compositional equilibrium appears to have been achieved near the  $\gamma'/\gamma$  interface for the first-generation of precipitates, a non-equilibrium long range diffusion profile in the  $\gamma$  matrix is retained during the process of continuous cooling which is largely responsible for the subsequent nucleation bursts at larger undercooling (or lower temperatures) leading to the second and third generations of precipitates. Additionally, since these subsequent generations of precipitates are formed at larger undercoolings, they are typically finer in size scale, exhibit far-from equilibrium compositions, and also have very diffuse  $\gamma'/\gamma$  interfaces, indicating a non-classical precipitation mechanism associated with their formation.

The  $\gamma'$  precipitation during slow continuous cooling of the Rene' 88 DT alloy from above the  $\gamma'$  solvus temperature at the rate of 24 °C/min, i.e. from the single  $\gamma$  phase field, has been investigated via in situ high energy x-ray diffraction studies, carried out using a high temperature furnace mounted on the synchrotron beam line at the Advanced Photon Source (APS) at the Argonne National Laboratory. The results of these diffraction studies show the progressive

change in the intensity of the (001)  $\gamma'$  superlattice, and (111) fundamental reflections arising from both  $\gamma$  and  $\gamma'$  phases, as a function of temperature during in situ slow continuous cooling from the single  $\gamma$  phase field. A sudden increase in (001) peak intensity during cooling between 1284 °C and 1174 °C, which then increases gradually with further reduction in temperature is noticed. The combined (111) reflection from  $\gamma'$  and  $\gamma$  phases show a gradual increase in intensity during the same cooling cycle. A simple first order approximation of the change in volume fraction of  $\gamma'$  as a function of temperature during continuous cooling, can be qualitatively measured by plotting the ratio of the intensities of (001)  $\gamma'$  peak to (111)  $\gamma' + \gamma$  peak at every temperature. The plot clearly shows that during the cooling experiment, the intensity of the (001)  $\gamma'$  peak starts increasing at a temperature marginally higher than 1200 °C, corresponding to the onset of the first nucleation burst. With decreasing temperature there is a continuous increase in the above intensity ratio, with a maxima at around 1000 °C. On subsequent cooling, there is another increase in the intensity ratio with an onset at a temperature ~800 °C with an actual maxima at around 700 °C. These peaks observed in the (001)  $\gamma'$  peak to (111)  $\gamma' + \gamma$  peak intensity ratio give an indication of various  $\gamma'$  nucleation bursts, eventually resulting in a multimodal size distribution of  $\gamma'$  precipitates. It is important to note that the relative increase in this intensity ratio is directly proportional to the volume fraction of newly formed  $\gamma'$  precipitates and with decreasing temperature, the relative increase in  $\gamma'$  volume fraction with each successive generation decreases. A systematic shift in the (001)  $\gamma'$  as well as (111)  $\gamma' + \gamma$  intensity peaks, indicating a decrease in lattice parameter for both  $\gamma'$  and  $\gamma$  phases with decreasing temperature is detected. This decrease in lattice parameters can possibly be attributed to the combined effect of thermal contraction and the chemical partitioning between  $\gamma'$  and  $\gamma$  phases. However, the changes in lattice parameters are not equal for  $\gamma'$  and  $\gamma$  phases that gives rises to an increase in the  $\gamma'/\gamma$  lattice mismatch with decreasing temperature as reported previously for the Rene' 88 DT alloy [Tiley J 2009]. This also alludes to the fact the ordered  $\gamma'$  phase is more stable with respect to temperature changes and therefore the change in lattice parameter with temperature is minimal for this phase.

#### 4.2.6.2.1. *Precipitate size and morphology*

Slow cooling (SC0) of Rene' 88 DT from a temperature exceeding the  $\gamma'$  solvus resulted in a multimodal distribution of precipitates as mentioned earlier. This multimodal distribution of precipitates can be divided into different groups based on their size, morphology and number density. These parameters in turn depend on the undercooling corresponding to the specific nucleation event, resulting in that particular population of precipitates. The different populations of  $\gamma'$  precipitates were characterized by coupling backscatter SEM studies with EFTEM studies.

Backscatter SEM images of the SC0 sample show the larger first generation  $\gamma'$  precipitates develop largely a cuboidal morphology or in some cases an irregular morphology, due to coarsening or impingement of neighboring  $\gamma'$  precipitates. Henceforth, these first generation  $\gamma'$  precipitates, will be referred to as primary  $\gamma'$  precipitates. These primary  $\gamma'$  precipitates have a relatively low number density, attributable to the smaller driving force for nucleation expected at lower undercooling. This is also evident on comparison with second and third generations of  $\gamma'$  precipitates forming at larger undercoolings (lower temperatures). Furthermore, there is a large variation in shape and size of the primary  $\gamma'$  precipitates. The equivalent diameters of these  $\gamma'$

precipitates were determined by measuring their respective areas and equating these areas to areas of equivalent circles. Due to the irregular shape of these precipitates, this method really provides a qualitative rather than a quantitative distribution of precipitate sizes. As expected from the figure, there is a large variation in the sizes of these precipitates, ranging from 100-400 nm in diameter with the maximum number of precipitates lying in the size range of 150-250 nm. Thus it is clear that the primary  $\gamma'$  precipitates of this size range can be analyzed based on SEM investigations.

The second generation, secondary  $\gamma'$  population, that nucleates at lower temperatures due to a very high thermodynamic driving force, grow at much lower rates due to the limited diffusivity at the lower temperatures. Imaging these rather small second generation  $\gamma'$  precipitates is difficult using SEM, and therefore EFTEM imaging was employed. These EFTEM images are recorded using the Cr M-edge in the electron energy loss spectrum, obtained from the same sample. As observed in the images, the  $\gamma'$  precipitates exhibit a darker contrast being depleted in Cr [Singh et.al. (2011), Sarosi et.al. (2005)]. As discussed earlier, the number density of the secondary  $\gamma'$  precipitates is clearly much larger than those of the primary  $\gamma'$  precipitates. This could be attributed to high nucleation rate at high undercoolings. Furthermore the primary  $\gamma'$  precipitates are separated from the secondary  $\gamma'$  precipitates by a precipitate-free depleted zone. Due to limited growth these secondary  $\gamma'$  precipitates exhibit near-spherical morphologies with size ranging from 12-30 nm in diameter.

On careful study of the higher magnification EFTEM image a third population of extremely fine scale  $\gamma'$  precipitates is visible. These precipitates are present between the primary and secondary  $\gamma'$  precipitates, beyond the precipitate free zone that surrounds the primary  $\gamma'$  precipitates. The extremely small size of these precipitates, even smaller than the secondary ones, may be a result of a third burst of nucleation at much lower temperatures (even higher undercooling). Due to their very small size and the limitations of EFTEM imaging in terms of spatial resolution, it is very difficult to accurately measure the size distribution of these precipitates using this technique.

#### *4.2.6.2.2. Overall size distribution*

Both bursts of nucleation give rise to two distinctly different populations of  $\gamma'$  with each nucleation event probably occurring over a range of temperatures, starting with a high driving force for nucleation which gradually decreases. The average diameter of the primary  $\gamma'$  precipitates is  $\sim 191$  nm with standard deviation of  $\sim 78$  nm. Secondary  $\gamma'$  precipitates have average diameter of  $\sim 8$  nm and a standard deviation of  $\sim 7$  nm. The salient points regarding the size distribution of  $\gamma'$  precipitates can be summarized as follows:

1. The size distribution of the primary  $\gamma'$  precipitates is quite large, ranging from  $\sim 100$  nm to  $\sim 400$  nm with a mean  $\sim 191$  nm indicating that the nucleation of these precipitates takes place over a wide range of temperatures during continuous cooling.
2. Second generation, secondary  $\gamma'$  precipitates, have a much higher number density as compared to primary  $\gamma'$  precipitates.

3. The distributions observed in this study also indicate that each nucleation burst occurs over a range of temperatures.
4. Within each temperature window for a specific generation of  $\gamma'$  precipitates, the larger number of precipitates nucleate at lower temperatures and a smaller number nucleate at higher temperatures.

As mentioned earlier, a third generation of (tertiary)  $\gamma'$  precipitates is also present in this SC0 sample. However the size distribution of the tertiary population cannot be accurately quantified using EFTEM. The distribution also shows that the size difference between primary and secondary  $\gamma'$  is more as compared to secondary and tertiary  $\gamma'$  populations. This can be attributed to the higher diffusivity at high temperatures (where the primary precipitates form) leading to their more rapid growth while the growth of the secondary and tertiary precipitates is rather limited at their lower formation temperatures. While previously reported modeling studies, based on classical nucleation theory, predict the formation of these multiple generations of  $\gamma'$  precipitates and their size distributions [Wen et.al. (2013), Wen et.al. (2006), Radis et.al. (2009)] this study is one of the first reports presenting direct experimental evidence of the size distribution associated with different generations of  $\gamma'$  precipitates forming during continuous cooling of a nickel base superalloy.

#### *4.2.6.2.3. Compositional analysis of different generations of $\gamma'$*

The compositional analysis of different generations of  $\gamma'$  precipitates has been carried out using atom probe tomography (APT). Reconstructions of APT data clearly shows sections of large primary (first-generation)  $\gamma'$  precipitates along with multiple fine scale  $\gamma'$  precipitates. A precipitate-free  $\gamma'$  depletion zone, containing only Ni ions, between the two different sizes of precipitates is also observed from the reconstructions in Fig. 5.

The partitioning of the primary alloying elements in Rene' 88 DT alloy, i.e. Al, Ti, Cr, Co, and Mo, for two different generations of  $\gamma'$  precipitates can be measured in by compositional profiles clearly revealed that all the  $\gamma'$  precipitates are enriched in Al and Ti and depleted in Cr, Co and Mo. The primary  $\gamma'$  precipitates contain a higher amount of Al and Ti, whereas the tertiary  $\gamma'$  have lower Al and Ti and higher Co and Cr. Even though there is a variation in size of the smaller  $\gamma'$  precipitates, the variability in composition between different precipitates was observed to be minimal. This indicates that even though the tertiary (or secondary) precipitates form over a range of temperatures, large variations in composition within this particular generation does not occur. A substantially more diffuse interface in case of the smaller precipitates was observed as compared with the primary ones. Similar evidence of a larger compositional width of the  $\gamma'/\gamma$  interface in case of smaller tertiary (or secondary) precipitates, indicating a compositionally diffuse interface, was observed in case of many other precipitates analyzed in the same manner.

While each generation of  $\gamma'$  has a different composition, the  $\gamma$  region near these  $\gamma'$  precipitates also exhibit local compositional variations. Right next to the primary  $\gamma'$  precipitate the  $\gamma$  matrix shows a near-equilibrium  $\gamma$  composition. It is evident that primary  $\gamma'$  precipitate contain higher amounts of Al and Ti whereas the depletion zone is enriched in Cr and Co. The compositional gradient across the interface also appears sharp. Mo partitioning across the interface is not large

even though it seems to be partitioning more towards the  $\gamma$  matrix. There is a local enrichment of Cr next to the interface ( $\sim 30$ at %) which slowly decays to  $\sim 27$ at % inside the depletion zone. These observations show that in Rene' 88 DT alloy there exists a compositional gradient within the precipitate free region of the  $\gamma$  matrix, where the composition of all the major alloying additions slowly change from near-equilibrium to far from equilibrium as one moves away from the interface into the  $\gamma$  matrix. However, as expected this gradient is much more diffuse in comparison to the compositional gradient observed across the  $\gamma'/\gamma$  interface. Additionally, it should be noted that the far-field composition of this precipitate free region within the  $\gamma$  matrix is enriched in Cr and Co, and depleted in Al and Ti, as compared to average alloy composition.

Comparing the proxigrams generated from primary and secondary (or tertiary) precipitates it is evident that the former exhibits a compositionally sharper interface when compared to the latter. This is in accordance with the prediction of Cahn and Hilliard [Cahn and Hilliard (1959)] who mentioned that at lower supersaturations (lower undercooling) the nucleus exhibits more classical-like behavior with a near-equilibrium composition and the region around this classical nucleus also approaches an equilibrium composition. However as supersaturation increases, corresponding to larger undercoolings (or lower precipitation temperatures) encountered by the smaller scale secondary or tertiary  $\gamma'$  precipitates, the nucleus starts losing its resemblance to a classical nucleus. Thus at higher undercooling, both Helmholtz free energy as well as gradient energy factors contribute to the diffuseness of the interface. Also no part of this non-classical nucleus is approximately homogeneous and the composition at its center is substantially lower than that of a classical nucleus. Another similar non-classical decomposition pathway that has been discussed in the literature and also applicable to  $\gamma'$  precipitation within the disordered  $\gamma$  matrix, is phase separation (or composition clustering) via spinodal decomposition followed by ordering within the appropriate phase separated pockets [Soffa (1989), Hill and Ralph (1982), Laughlin et.al. (1976), Viswanathan et.al. (2011)]. Such decomposition is expected to take place in systems that have been undercooled to a large extent below the equilibrium transformation temperature. When a disordered solid solution is rapidly cooled (or quenched) from a single-phase field to a temperature corresponding to a two-phase field, the resulting highly undercooled and supersaturated disordered solid solution is often unstable (or metastable) with respect to both clustering and ordering processes [Soffa (1989)]. Experimental evidence of such a decomposition pathway in nickel base alloys has been previously reported in the literature in case of binary Ni-Al [Hill and Ralph (1982)] and Ni-Ti alloys [Laughlin et.al. (1976)], as well as in a recent study on very fast quenched Rene 88 DT [Viswanathan et.al. (2011)]. The important difference to note is that while in these systems that have been rapidly cooled to low temperatures below the equilibrium transformation temperature, a monomodal size distribution of ordered  $\gamma'$  precipitates result, in the present study there are multiple generations of  $\gamma'$  precipitates and the mechanism of spinodal decomposition followed by ordering might be applicable to only the second (or third) generation of precipitates. However, more detailed investigations are required in order to develop a more detailed understanding of the precipitation mechanism applicable to the refined second or third generation of ordered precipitates.

#### *4.2.6.2.4. Growth influenced Morphology and Chemical changes*

Three-dimensional (3D) atom probe reconstruction of the slow cooled and 760 °C/1 hr aged (SC1) sample the depletion zone between precipitates of two different generations is clearly

visible in this reconstruction. The overall size of these precipitates was determined using the IVAS<sup>TM</sup> software and their equivalent diameters. Similar to the studies conducted in case of the SC0 sample, the first and second generation of primary and secondary  $\gamma'$  precipitates were imaged using SEM and EFTEM respectively and subsequently their size distributions were measured. This sample contains three different  $\gamma'$  generations, obtained using three different characterization tools, suggesting three distinct nucleation bursts corresponding to different undercooling values below the  $\gamma'$  solvus temperature. Similar to the SC0 condition, on moving away from the  $\gamma'/\gamma$  interface, while the near field  $\gamma$  composition has reached equilibrium, the far-field  $\gamma$  composition is far-from equilibrium and contains lower than equilibrium amounts of Cr and Co, and supersaturation of Al and Ti.

Similar studies were conducted on Rene 88 DT samples that were aged for 15 hours at 760°C after solutionizing and slow cooling to room temperature (SC15). The smaller  $\gamma'$  precipitates are coarser than those in the SC0 condition. However, very limited changes are observed in the size of primary  $\gamma'$  precipitates or the depleted zone around them. Atom probe tomography was conducted with the SC15 sample so as to obtain the true morphology and size of the tertiary (or secondary)  $\gamma'$  precipitates. The  $\gamma'$  precipitates have grown and are ~20 nm in diameter after 15 hours of aging. Also the size of the  $\gamma'$  precipitates closest to the primary precipitate appear to be smaller than the precipitates present at further distances from the primary precipitate indicating the development of three distinct populations, primary, secondary, and tertiary. The long-range composition profiles for the alloying elements across the primary  $\gamma'/\gamma$  interface into the precipitate free depleted zone have shown that for all alloying elements the compositional profile within the precipitate free depleted zone remains constant, clearly indicating that the far-field  $\gamma$  matrix has reached its equilibrium composition in this case. Consequently, there is no supersaturation of Al and Ti (or undersaturation of Cr and Co) present within the matrix that can lead to nucleation or growth of additional  $\gamma'$  precipitates.

#### 4.2.6.2.5. Mechanism of multiple bursts of nucleation

Based on the detailed experimental results presented in this paper it is now possible to develop a mechanistic model leading to the multiple nucleation bursts of  $\gamma'$  precipitates during continuous cooling of a nickel base superalloy. This mechanism has been schematically shown using two representative figures, Figs. 9 and 10. During cooling, due to the continuous decrease in temperature below the  $\gamma'$  solvus, there is an associated increase in the thermodynamic driving force for nucleation associated with the continuously increasing undercooling. However as soon as the first generation of  $\gamma'$  precipitates are nucleated, this driving force is partially consumed, especially in the local region surrounding the first-generation (or primary) precipitates. Thus, the local region surrounding these primary  $\gamma'$  precipitates, also referred to as the near-field  $\gamma$  composition, is depleted in  $\gamma'$  forming elements, Al and Ti, and enriched in  $\gamma$  stabilizing elements, Co and Cr. Since the first nucleation burst occurs at relatively high temperatures (low undercooling below the  $\gamma'$  solvus), the higher diffusivity of the various alloying elements promotes their rapid partitioning between the  $\gamma'$  precipitate and the adjacent  $\gamma$  matrix. Also at these high temperatures, the primary  $\gamma'$  precipitates grow quite rapidly and develop a cuboidal to irregular morphology (schematic in Fig. 10) as anisotropic elastic strain energy starts dominating over the isotropic interfacial energy. However as temperature decreases, due to the reduced mobility of the solute elements, their redistribution becomes more and more difficult. Thus a

condition similar to the schematic diagram in Fig. 9(a) occurs where the near-field  $\gamma'$  composition, close to the primary  $\gamma'$  precipitates, reaches equilibrium (as suggested by a decrease in Al and increase in Cr). However as one probes away from the precipitate, far-field into the  $\gamma$  matrix, there is an enrichment of Al (and Ti) and depletion of Cr (and Co), primarily because of the inability of these regions to equilibrate rapidly at low temperatures (Fig. 9(a)). A schematic of a typical near field near-equilibrium and far field non-equilibrium composition profile for Co has been shown in Fig. 10. This results in the formation of far-field supersaturated corridors within the  $\gamma$  matrix, that act as potential sites for  $\gamma'$  nucleation at lower temperatures when the relative driving force increases. Thus, at these lower temperatures, the higher thermodynamic driving force and higher nucleation rate result in a second nucleation burst leading to a large number density of  $\gamma'$  precipitates, increasing the  $\gamma'$  volume fraction.

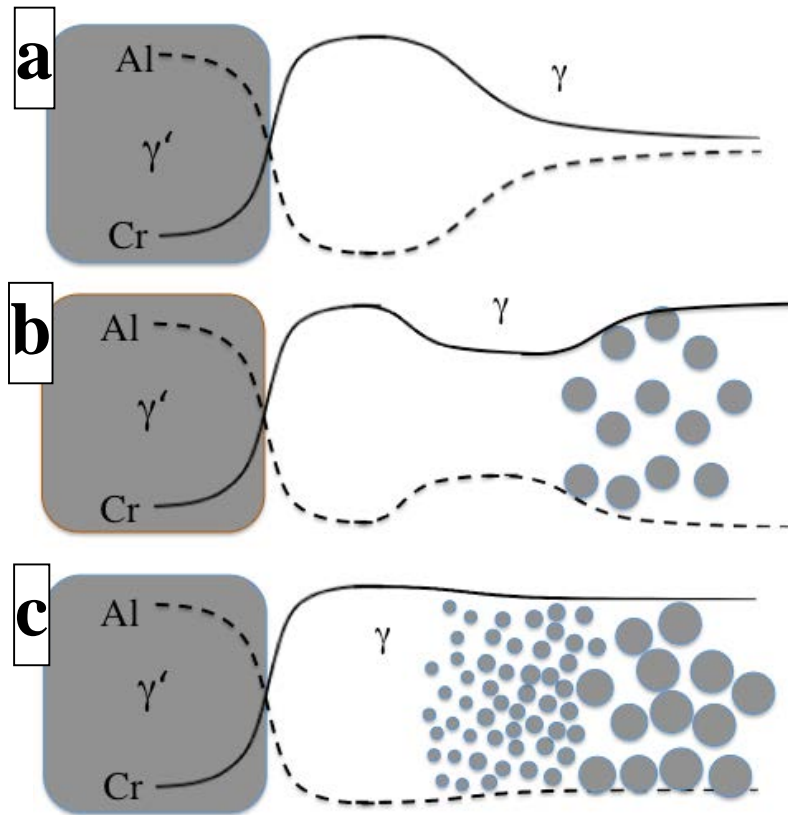


**Figure 9:** (a)-(c) Schematic illustrations of how multiple  $\gamma'$  generations can form during slow cooling of Rene' 88 DT alloy.

On further cooling these particles try to grow but their growth is severely restricted due to the low diffusivities. Thus the second generation of precipitates has a higher number density and is smaller than the first generation of precipitates (schematic in Fig. 10). Furthermore, this high number density of secondary precipitates leads to small inter-precipitate distances and consequently results in rapid overlap of the diffusion fields (soft impingement), restricting their further growth. These precipitates are small enough such that the isotropic interfacial energy dominates over anisotropic elastic strain energy. This coupled with the inherently low  $\gamma$ - $\gamma'$  misfit in case of Rene' 88 DT, results in these secondary precipitates maintaining a near spherical

morphology. Also as discussed earlier, these secondary precipitates do not exhibit features of a classically nucleated precipitate of equilibrium composition, but rather exhibit both compositional inhomogeneities within the precipitates as well as relatively diffuse  $\gamma'/\gamma$  interfaces.

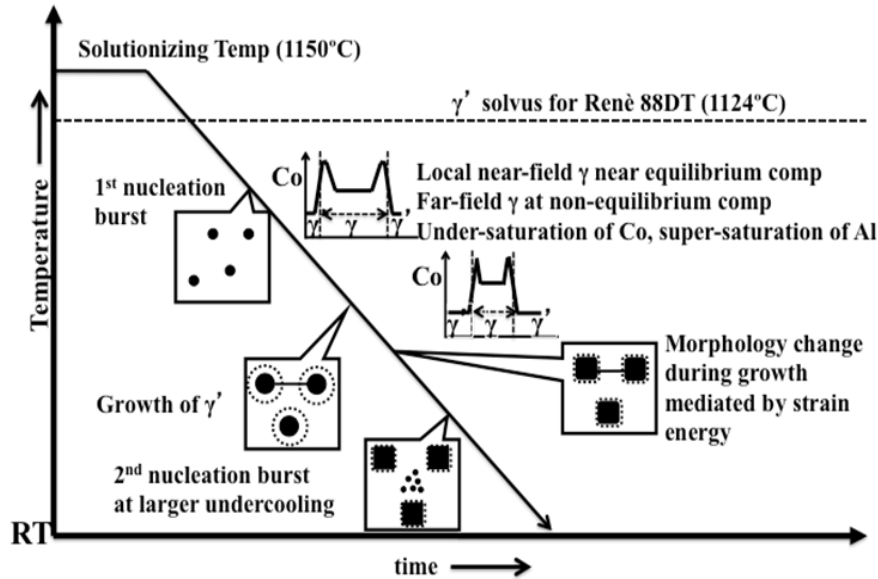


**Figure 10:** Schematic illustrating the effect of cooling rate on the formation of different gamma prime generations in Rene 88 DT alloy.

Changes also take place in the  $\gamma$  matrix that surround these precipitates. Thus the matrix becomes depleted in Al (and Ti) and enriched in Cr (and Co), as shown in the schematic diagram in Fig. 9(b). Thus at this temperature the region close to the secondary  $\gamma'$  precipitates have a very low driving force for further nucleation. However Fig. 9(b) also shows that the  $\gamma$  matrix between the secondary  $\gamma'$  and the depleted zone (around the primary  $\gamma'$ ) still retains a non-equilibrium composition, involving, for example, an Al supersaturation (or Cr undersaturation). However the thermodynamic driving force is not sufficient to cause any fresh nucleation until a really large undercooling is achieved. This undercooling occurs when the sample is cooled to further lower temperatures that leads to a third burst of nucleation resulting in the population of tertiary  $\gamma'$  precipitates (schematic diagram in Fig. 13(c)). However, slower kinetics and limited supersaturation of solute at this stage further limit the growth of these tertiary  $\gamma'$  precipitates. Thus a large number of fine scale spherical  $\gamma'$  precipitates are formed. It should be noted that typically the tertiary  $\gamma'$  precipitates are nucleated in between the primary and secondary  $\gamma'$  precipitates but closer to the secondary precipitates, primarily because the depletion zone around a secondary  $\gamma'$  precipitate is much smaller than that of primary  $\gamma'$  precipitate (Fig. 9(c)). Summarizing, several thermodynamic and kinetic factors such as driving force for nucleation, number density of nucleation sites (related to the nucleation rate), and diffusivity determine the formation of multiple generations of  $\gamma'$  precipitates and the complex interplay of these factors give rise to the multi-scale microstructures that are experimentally observed on continuous cooling. These observations are in excellent agreement with the phase field simulations reported

previously [Wen et.al. (2003)] as well as with experimental investigations in some commercial nickel base superalloys [Babu et.al. (2001), Sarosi et.al. (2007), Radis et.al. (2009)], where continuous cooling results in shrinkage of diffusion fields associated with larger  $\gamma'$  precipitates, consequently opening up precipitate free supersaturated  $\gamma$  channels where further nucleation events can take place.

#### **4.2.7. Task G: Growth and coarsening of L1<sub>2</sub> precipitates in new generation Co based alloy**

The expeditious development of novel cobalt base  $\gamma$ – $\gamma'$  alloys as possible next generation superalloys critically depends on achieving a comprehensive understanding of the coarsening kinetics of ordered  $\gamma'$  precipitates. This paper discusses the coarsening of L1<sub>2</sub> ordered Co<sub>3</sub>(W, Al) precipitates in a model ternary Co-10Al-10W(at%) alloy during isothermal annealing at 800 °C and 900 °C. The experimentally determined temporal evolution of average size of the  $\gamma'$  precipitates suggests classical matrix diffusion limited LSW coarsening at both temperatures. The  $\gamma'$  coarsening rate constants have been determined using a modified coarsening rate equation for non-dilute solutions. Furthermore, using the Cahn-Hilliard formulation for interfacial energy, the  $\gamma/\gamma'$  interfacial energies at the respective annealing temperatures have been correlated to the concentration profile across the interface that has been experimentally determined using atom probe tomography (APT). The calculated interfacial energies are in comparable range with those observed in Nickel base superalloys. Additionally, this analysis has permitted, for the first time, the determination of the gradient energy coefficient for  $\gamma/\gamma'$  interfaces in Co-base alloys, a critical input for phase-field and other simulation models for microstructural evolution.

##### *4.2.7.1. Water quenched condition prior to annealing*

The presence of {001} type superlattice reflections along with fundamental reflections from disordered cobalt matrix indicates the formation of L1<sub>2</sub> ordered  $\gamma'$  precipitates in face centered cubic (FCC) Co solid solution during rapid cooling from a supersolvus temperature. Centered dark field image, recorded from a {001} superlattice reflection, which shows a uniform distribution of very fine scale  $\gamma'$  precipitates. Though it is rather difficult to accurately measure the sizes of these precipitates, using the Image J software, the size range of  $\gamma'$  precipitates was determined to be 2-6 nm in radius.

Further, APT studies have been carried out on the water quenched sample. The precipitate size and morphology obtained from APT reasonably matches with the TEM observations. A proxigram, constructed using interfaces created with a 10 at % W isosurface, shows partitioning of solutes across a compositionally diffuse, order-disorder interface. The proxigram reveals that W partitions into  $\gamma'$  whereas Co partitions into  $\gamma$ . Interestingly, Al does not appear to exhibit any substantial tendency to partition. The summation of Al content (~10 at %) and W content (~13.5 at%) in the  $\gamma'$  phase is ~23.5%, very close to the 25 at % expected for a stoichiometric Co<sub>3</sub>(Al,W) phase. The local depletion of solute in the  $\gamma$  matrix adjacent to the interface due to matrix diffusion limited growth is clearly visible. While W exhibits a very strong tendency to partition to the  $\gamma'$  phase, Al appears to exhibit a very weak tendency to partition to the  $\gamma'$  phase.

#### *4.2.7.2. Morphological changes during isothermal annealing*

The morphological evolution of the L1<sub>2</sub>  $\gamma'$  precipitates has been extensively studied in nickel base superalloys [McLean et.al. (1984), Yoo et.al. (1995), Vaithyanathan et.al. (2002)]. It has been generally concluded that the competing factors of  $\gamma/\gamma'$  interfacial energy and the elastic strain energy arising from  $\gamma/\gamma'$  lattice parameter mismatch determines the equilibrium shape of the  $\gamma'$  precipitates as a function of their size. Furthermore, the favorable growth of  $\gamma'$  precipitates along low energy {001} type planes of the matrix  $\gamma$  phase along with elastic interactions among these precipitates leads to specific spatial correlations between the precipitates. The evolution of the shape and configuration of  $\gamma'$  precipitates during isothermal annealing at 800 °C and 900 °C in the Co-10Al-10W alloy has been investigated in detail via both SEM and TEM studies. Both the equivalent radius and equilibrium volume fraction of  $\gamma'$  have been measured using the Image J software from TEM Dark-field images. Irrespective of annealing temperature,  $\gamma'$  precipitates exhibited a morphological transition from near spherical to cuboidal shape, at an early stage of growth/coarsening coupled with the development of a spatial co-relation among the precipitates. The expected high volume fraction of precipitates resulting from higher solute supersaturation at the lower annealing temperature of 800 °C as compared to 900 °C is clearly revealed. It is evident that there is a substantial difference in the extent of coalescence of precipitates between 800 °C and 900 °C

#### *4.2.7.3. Compositional changes across $\gamma/\gamma'$ interface during isothermal annealing*

The proxigrams reveals similar compositional partitioning of Al and W as compared to that of the water quenched sample. The local depletion of W in the  $\gamma$  matrix near the  $\gamma/\gamma'$  interface can be rationalized based on the matrix diffusion-limited growth of the  $\gamma'$  precipitates. Thus, during their growth, while W diffuses into these precipitates, the limited diffusivity of this heavy solute in the Co matrix presumably results in local equilibrium to be established near the interface while far-field equilibrium in the  $\gamma$  matrix is still not achieved. Since the far field  $\gamma$  composition retains a supersaturation of W, there is sufficient driving force for further growth of precipitates. After 4 hours annealing, the local W depletion near the  $\gamma/\gamma'$  interface disappears and the composition within the  $\gamma$  matrix is relatively uniform. This indicates that the solute supersaturation in the matrix has been consumed and therefore, further increase in the precipitate size is solely due to coarsening. With continued annealing up to 16 hours and 64 hrs, there is no significant change in composition. Assuming that the compositions of the  $\gamma$  and  $\gamma'$  phases are near-equilibrium after an annealing period of 64 hrs at 900 °C, the equilibrium partitioning co-efficient of W,  $K_{\gamma/\gamma'}$  can be calculated as 2.66. In contrast, the partitioning coefficient for Al has not been calculated because of the insignificant partitioning of this solute between the two phases. While the lack of any significant partitioning of Al between  $\gamma$  and  $\gamma'$  phases is rather unusual, it indicates that the equilibrium compositions of these two phases at 900 °C presumably contain equal amounts of Al.

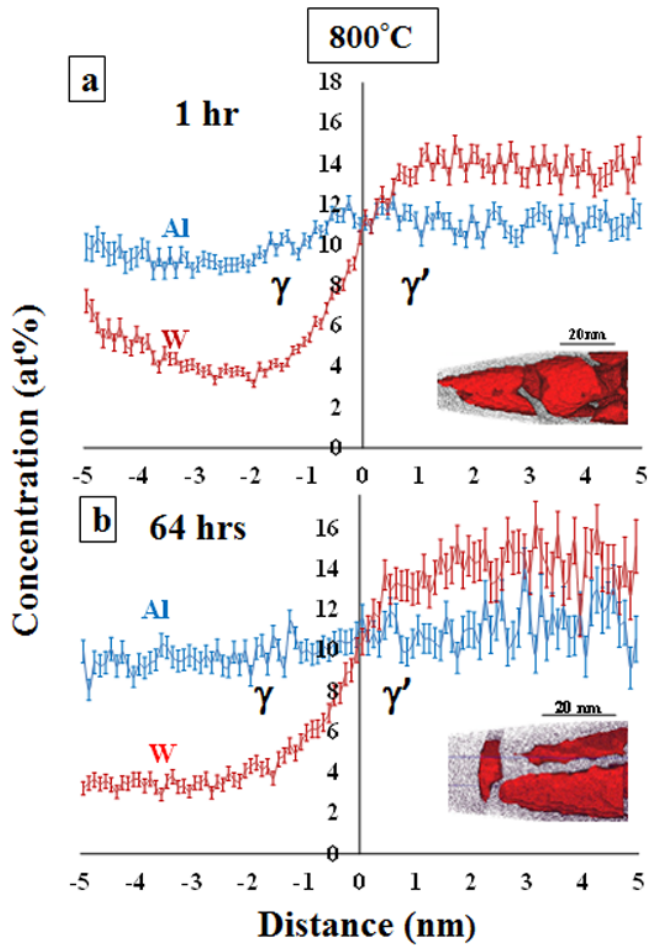


**Figure 11:** Proxigrams corresponding to 9 at% W shows  $\gamma/\gamma'$  interface with partitioning of Al and W in samples subjected to varying isothermal annealing periods at 800°C along with APT reconstructions as insets where 9 at % W isosurface (red) delineates  $\gamma'$  precipitates.

Similarly, the compositional partitioning across  $\gamma/\gamma'$  interfaces for different isothermal annealing time periods at 800 °C, are shown via proxigrams, created from 9 at% W isosurfaces in Fig. 11. The corresponding APT reconstructions are also shown as insets. Fig. 11(a), corresponding to an annealing time period of 1 hr, shows local equilibrium of W near the  $\gamma/\gamma'$  interface while long – range equilibrium has yet been achieved and a W supersaturation is retained within the  $\gamma$  matrix. The equilibrium compositions of both  $\gamma$  and  $\gamma'$  phases after long term annealing (64 hrs) at 800 °C have been listed in Table 5. The partitioning coefficient of W,  $K_{\gamma'/\gamma} \sim 4$  is higher as compared to that observed at 900 °C. This difference in partitioning behavior can be rationalized based on the phase equilibria as a function of temperature. The curvature of the single phase  $\gamma$  and  $\gamma'$  phase boundaries, separating these phases from the two-phase  $\gamma + \gamma'$  region, is usually concave indicating that with increasing temperature, the relative difference in solute content of these two phases decreases. Furthermore, it should be noted that the gradual increase in partitioning of W

across the  $\gamma/\gamma'$  interface, with annealing time, affects the misfit between these two phases and the resultant strain energy, in turn affects the morphological evolution.

Table 5 Equilibrium composition of  $\gamma$  and  $\gamma'$  measured from APT

Temperature (°C)	Compositions (at %)	
	$\gamma$	$\gamma'$
800	Co-10Al-3.5W	Co-10Al-14 W
900	Co-10Al-4.5 W	Co-10Al-12 W

#### 4.2.7.4. Interfacial energy from the Cahn-Hilliard approximation

Ardell [Ardell AJ. Scripta Mater. (2012)] in a recent paper has associated the  $\gamma/\gamma'$  interfacial energy with the concentration gradient across this coherent interface via the concept of a gradient energy term, originally proposed by Cahn and Hilliard [Cahn and Hilliard (1958), Cahn and Hilliard (1959),]. The interfacial energy ( $\sigma$ ) is related to the gradient energy coefficient ( $\chi$ ) and the concentration gradient across the interface ( $dC/dx$ ) as follows [Cahn and Hilliard (1958)]

$$\sigma = 2\chi \int_{C_\gamma}^{C_{\gamma'}} \left( \frac{dC}{dx} \right) dX \quad (14)$$

The proximity histograms obtained from APT which show the concentration profile across the interface with sub-nanometer resolution, can be described by sigmoid functions and can be used to directly determine the average change in concentration over the width of the interface,  $(dC/dx)_{avg}$  and the difference in solute content between the two phases,  $\Delta C$  for evaluating the interfacial energy.

According to Ardell [Ardell (2012)], interfacial energy is related to gradient energy coefficient and interface width ( $\delta$ ) as follows:

$$\sigma = \frac{4\chi \Delta C^2}{3\delta} \quad (15)$$

and moreover, if the compositional profile across the interface is fitted to a sigmoid function, the interface width can be calculated as [Ardell (2012)] :

$$\delta = \frac{\Delta C}{\left(\frac{dC}{dx}\right)_{max}} \quad (16)$$

Hence, the interfacial energy can be rewritten as

$$\sigma = \frac{4\chi\Delta C \left(\frac{dC}{dx}\right)_{max}}{3} \quad (17)$$

While in the original formulation by Cahn and Hilliard, the maximum concentration gradient across the interface was used for evaluating equation (17), it should be noted that the experimentally determined concentration gradient obtained from APT is not very smooth due to its very high spatial resolution. Consequently, using the maximum gradient  $(dc/dx)_{max}$  in the formulation proposed by Cahn and Hilliard, can lead to errors in the numerical evaluation of  $\sigma$  resulting from local fluctuations in the composition profile. Therefore, in the present study,  $(dc/dx)_{max}$  has been replaced by  $(dc/dx)_{avg}$ , which is an average value of concentration gradient over 1 nm across the local region around  $(dc/dx)_{max}$ . Moreover, Cahn and Hilliard [Cahn and Hilliard (1958), Cahn J and Hilliard (1959)] have mentioned that gradient energy coefficient can be regarded as being independent of temperature for regular solutions. Hence, the ratio of the interfacial energies for the two annealing temperatures can be expressed as:

$$\frac{\sigma_1}{\sigma_2} = \frac{\Delta C_1 \left[\frac{dC}{dx}\right]_{avg1}}{\Delta C_2 \left[\frac{dC}{dx}\right]_{avg2}} \quad (18)$$

Where  $\Delta C$  is the difference in equilibrium concentration of the solute in both phases and  $\left[\frac{dC}{dx}\right]_{avg}$  is the average concentration gradient over 1 nm across the  $(dc/dx)_{max}$  at the interface. The calculated values of  $(dc/dx)_{avg}$  are 3.49 and 2.57 and the composition difference of W between the two phases are 10.5 and 7.5 at% for samples annealed for 64 hours at 800 °C and 900 °C respectively. So substituting these values in equation (18), the value of  $\sigma_1/\sigma_2$  has been calculated to equal 1.91. These results clearly indicate that the  $\gamma/\gamma'$  interfacial energy changes with respect to temperature.

#### 4.2.7.5. Coarsening rate constants based on LSW theory

There has been extensive research work that demonstrates that the coarsening of  $\gamma'$  precipitates in a  $\gamma$  matrix typically follows a matrix diffusion-controlled growth behavior, explained by classical LSW coarsening model. Recently, a second coarsening model, the trans-interface diffusion controlled (TIDC) coarsening model [Ardell and Ozolins (2005)] has been proposed. The basis for this second model is that in certain cases, especially in systems involving order/disorder

interfaces such as  $\gamma/\gamma'$  interfaces, the diffusion of solute across a partially ordered interface can be rate limiting rather than solute diffusion through the disordered matrix [Ardell and Ozolins (2005)]. The temporal exponent of coarsening roughly determines the coarsening mechanism: it is expected to be 3 for LSW coarsening and 2 for TIDC coarsening. To determine the operative mechanism of coarsening of  $\gamma'$  precipitates in the Co-10Al-10W (at%), a plot of the logarithm of average precipitate radius ( $\log r$ ) versus the logarithm of ageing time in seconds ( $\log t$ ) for both temperatures (800 °C and 900 °C) is done. The slope of a linear fit to the data points yields the inverse of the temporal exponent that is 0.33 and nearly equal for both temperatures. Therefore, the experimentally determined temporal exponent of coarsening indicates that LSW is the dominant coarsening mechanism indicating that solute (W in this case) diffusion through the  $\gamma$  matrix diffusion is the rate-controlling step.

In case of matrix diffusion-limited coarsening, the temporal evolution of average precipitate size follows the following law:

$$r^3 - r_0^3 = K \cdot t \quad (19)$$

Where  $r_t$  is the mean particle size at time  $t$ ,  $r_0$  is the mean particle size at annealing time,  $t = 0$  and  $K$  = coarsening rate constant

The average precipitate sizes for different annealing time periods at both temperatures have been plotted on a graph of precipitate size (equivalent radius raised to the third power) vs. annealing time ( $t$ ). Linear fits to these plots for the respective datasets, yield slopes that give the rate constants,  $K = 0.07 \times 10^{-27} \text{ m}^3/\text{sec}$  and  $1.41 \times 10^{-27} \text{ m}^3/\text{sec}$  for 800 °C and 900 °C respectively. With an increase in annealing temperature of 100 °C, the coarsening rate appears to increase nearly 20 times.

One of the drawbacks of the original LSW model of coarsening is its applicability to only dilute solution containing small volume fraction of precipitates as well as a near zero solubility of the solute in the matrix. Subsequently, modifications have been proposed to the original coarsening model to overcome this and other assumptions. Since the  $\gamma'$  volume fraction observed in the Co-10Al-10W (at%) is relatively large and far-from a dilute solution, the experimental data presented in this paper has been analyzed based on the description of coarsening kinetics referred to as the modified form of LSW model by Calderon et al. [Calderon HA et.al. 1994]. This modification takes into account significant solute solubility in the  $\gamma$  matrix as experimentally observed in many alloy systems and the corresponding rate equation has dependence on the solute content of both matrix and precipitate phases.

Assuming that the diffusion of W in the  $\gamma$  matrix as the rate-limiting step for precipitate coarsening (assumption based on APT observations) the LSW rate constant,  $K$ , can be determined as follows:

$$K = \frac{8DC_e(1-C_e)V_m\sigma}{9RT(C_e^{\gamma'} - C_e)^2} \quad (20)$$

where D is the diffusion coefficient of W in the matrix,  $C_e$  is the solubility (in atomic fraction) of W in equilibrium with the precipitate,  $C_e^{\gamma'}$  is the equilibrium solubility of W in the  $\gamma'$  precipitate,  $\sigma$  is the precipitate/matrix interfacial energy,  $V_m$  is the molar volume of the precipitate, R is the universal gas constant ( $=8.31 \text{ Jmol}^{-1}\text{K}^{-1}$ ) and T is the absolute temperature. The reported lattice parameter of cubic  $\text{Co}_3(\text{Al},\text{W})$ , based on DFT calculations is  $3.55 \text{ \AA}$ , yielding a molar volume of these precipitates as  $6.8 \times 10^{-6} \text{ m}^3/\text{mol}$ .

#### 4.2.7.6. Determination of the activation energy

The diffusivity of W in the  $\gamma$  matrix can be expressed as

$$D = D_0 \exp\left(\frac{-Q}{R.T}\right) \quad (21)$$

Where  $D_0$  is the diffusion coefficient for  $W = 10^{-3} \text{ m}^2/\text{sec}$  and Q is the activation energy for W diffusion in the  $\gamma$  matrix. Using equations 7 and 8 for two different temperatures, an expression for determination of activation energy can be written which employs experimentally determined parameters as follows:

$$\ln\left[\frac{KT(C_e^{\gamma'} - C_e)^2}{C_e(1-C_e)\sigma}\right] = \text{Constant} - \frac{Q}{RT} \quad (22)$$

Equation 22 has been used to determine the activation energy for diffusion of W in the  $\gamma$  matrix by comparing data on annealing at both  $800 \text{ }^{\circ}\text{C}$  and  $900 \text{ }^{\circ}\text{C}$ . Q was calculated to be  $295 \text{ kJ/mol}$ . Previously, values of Q in binary  $\text{Co}-10 \text{ at\%W}$  alloys was reported as  $310 \pm 11 \text{ kJ/mol}$ , which is very close to the value reported in the present study. Substituting the value of  $Q = 295 \text{ kJ/mol}$  in equation 3, the diffusivity of W in the  $\gamma$  matrix, D, can be calculated to be  $4.387 \times 10^{-18} \text{ m}^2/\text{sec}$  and  $7.28 \times 10^{-17} \text{ m}^2/\text{sec}$  at  $800 \text{ }^{\circ}\text{C}$  and  $900 \text{ }^{\circ}\text{C}$  respectively.

#### 4.2.7.7. Determination of $\gamma/\gamma'$ interfacial energy and the gradient energy coefficient

Historically, the coarsening data for  $\gamma'$  precipitates in nickel base alloys has been used to experimentally determine the  $\gamma/\gamma'$  interfacial energy in these alloys [McLean D 1984, Vaithyanathan V 2002]. The values reported in the literature, based on such coarsening data vary over a wide range, from  $10 \text{ mJ/m}^2$  to  $100 \text{ mJ/m}^2$  [Ravi R et.al. (2011)]. This variation is expected

due to variations in alloy compositions and experimental conditions, as well as application of different precipitate coarsening models to analyze the data.

A similar approach is being employed in the present case to determine the  $\gamma/\gamma'$  interfacial energy in the Co-10Al-10W alloy. Thus, substituting the experimentally determined K, D and  $C_e$  values in equation 2, the values of  $\sigma$  have been evaluated as 10 and 19 mJ/m<sup>2</sup> at 900 °C and 800 °C respectively. Substituting the experimentally determined value of  $\gamma/\gamma'$  interfacial energy at 900 °C in equation 4, the gradient energy coefficient has been evaluated as  $5 \times 10^{-9}$  J/m for the Co-Al-W system.

#### *4.2.7.8. Inter-precipitate distances and coalescence of $\gamma'$ precipitates*

The average inter-precipitate distance after annealing at 800 °C for 256 hours is  $\sim 25$  nm which is about half that after annealing at 900 °C for the same time period ( $\sim 55$  nm). The Image J software was used for measuring the inter-precipitate distance and a large dataset has been used to minimize the statistical inaccuracy in these measurements. The lower inter-precipitates distance at 800 °C can be attributed to the higher volume fraction of precipitates at this temperature as compared to 900 °C, and consequently can lead to a higher propensity for precipitate coalescence at 800 °C.

The driving force for coalescence of  $\gamma'$  precipitates has been previously attributed, in case of nickel base superalloys, to the removal of the elastically strained  $\gamma$  matrix between two precipitates, dominant in systems exhibiting a high  $\gamma/\gamma'$  lattice mismatch [Lifshitz et.al. (1961), Wagner et.al. (1961)]. However, the coalescence of these ordered  $\gamma'$  precipitates is often limited by the high energy of the antiphase domain boundary, APB  $\sim 220$  mJ/m<sup>2</sup> [Flinn et.al. (1960)], that forms when two out-of-phase ordered precipitates come in proximity. The APB energy is usually very high as compared to the  $\gamma/\gamma'$  interfacial energy. There are four different crystallographic variants of  $\gamma'$  precipitates that can form during the  $\gamma \Rightarrow \gamma + \gamma'$  precipitation reaction. Statistically, there is only a 25% probability that two adjacent and independently nucleated  $\gamma'$  precipitates belong to the same crystallographic variant. Consequently, the degree of coalescence remains rather limited even in systems containing a high volume fraction of  $\gamma'$  precipitates. The experimentally observed coalescence of the  $\gamma'$  precipitates in case of the Co-10Al-10W alloy in the present study is rather interesting considering that the  $\gamma/\gamma'$  interfacial energy is quite low  $\sim 19$  mJ/m<sup>2</sup>. While the APB energy in this system is presently not known, it is difficult to justify that the APB energy would be lower than the  $\gamma/\gamma'$  interfacial energy. Furthermore, it should be noted that though close proximity of the  $\gamma'$  precipitates, a thin wetting layer of  $\gamma$  matrix between the precipitates is also observed in multiple cases

#### 4.2.7.9. Discussion

Similar to nickel base superalloys, Co-Al-W alloys also exhibit the presence of coherent ordered  $\gamma'$  precipitates within the disordered  $\gamma$  matrix and therefore are being actively investigated for potential high temperature applications. While the high temperature mechanical properties and deformation behavior of Co-Al-W alloys are promising, recent studies indicate that the additions of alloying elements such as Ta, enhance these properties even further as compared to the base ternary alloy [Suzuki and Pollock (2008)]. Some initial investigations have also been carried out on solute partitioning and site preferences within the  $\gamma'$  precipitates in these alloys [Meher et.al. (2012)]. The focus of the present study is a detailed investigation of the coarsening kinetics of  $\gamma'$  precipitates in a ternary Co-10Al-10W base alloy. The temporal evolution of precipitate size, along with the concentration profile in the  $\gamma$  matrix adjacent to the  $\gamma/\gamma'$  interface, suggest that solute diffusion of W through the matrix is the rate-limiting phenomenon governing the coarsening of the  $\gamma'$  precipitates (Oswald ripening or LSW model).

The experimentally determined coarsening rate constant (K) in case of the Co-10Al-10W alloy, determined in the present study, is  $0.07 \times 10^{-27} \text{ m}^3/\text{sec}$  at  $800^\circ\text{C}$ . Values of coarsening rate constants (K) reported for typical Ni base superalloys, such as Nimonic 115 at  $800^\circ\text{C}$  and Rene' 88DT at  $760^\circ\text{C}$ , are  $0.87 \times 10^{-27} \text{ m}^3/\text{sec}$  [Li et.al. (2002)] and  $0.0157 \times 10^{-27} \text{ m}^3/\text{sec}$  [Tiley et.al. (2009)]. Comparing these values with the experimentally determined value for Co-10Al-10W (at%), indicates that while  $\gamma'$  coarsening rate is slower in case of Rene' 88DT, it is actually faster in case of Nimonic 115. The  $\gamma/\gamma'$  lattice misfit will influence the interfacial energy which in turn will affect the morphology and coarsening kinetics of the  $\gamma'$  precipitates in these alloys. There is very limited data reported in the published literature on  $\gamma/\gamma'$  lattice misfit in case of Co-Al-W base alloys. Sato et al. has reported the value of  $\gamma'/\gamma$  lattice misfit as 0.53% for a Co-9Al-9W (at%) alloy, subjected to long term annealing at  $900^\circ\text{C}$  [Sato et.al. (2006)]. This alloy is similar in composition to the alloy being investigated in the present study. Additionally, another recent paper reports that the  $\gamma/\gamma'$  lattice mismatch values are 0.34% and 0.78%, respectively, for Co-8Al-8W-25Ni (at %) and Co-10Al-5W-2Ta (at %) [Yan et.al. (2012)]. All these reported misfit values in Co-base alloys are rather large and can consequently explain the faster  $\gamma'$  coarsening rate. In contrast, the  $\gamma'/\gamma$  lattice misfit in case of Rene 88DT is 0.05% which explains the relatively low coarsening rate in this Ni base alloy. Furthermore, in case of a model Ni-7.5Al-8.5Cr (at%) alloy, the  $\gamma'/\gamma$  lattice mismatch has been reported to be 0.27% and the coarsening rate constant, K, for  $\gamma'$  precipitates as  $1.84 \times 10^{-31} \text{ m}^3/\text{s}$  at  $600^\circ\text{C}$  [Booth-Morrison et.al. (2008)]. However, despite the high  $\gamma'/\gamma$  lattice misfit in case of Co-Al-W alloys, the coarsening rate of  $\gamma'$  precipitates is restricted in part due to the very low diffusivity of W in this alloy.

As regards the mechanical properties of  $\gamma/\gamma'$  Co-Al-W base alloys, Suzuki et al. have reported that these alloys exhibit a temperature dependent flow stress behavior, similar to that observed in case of  $\gamma/\gamma'$  Ni base alloys [Suzuki and Pollock (2008)]. Therefore, Co-Al-W alloys exhibit an

increase in flow stress with increasing temperature of deformation. For example, in case of a Co-9Al-9W (at%) alloy the flow stress varies from 420 MPa at 600 °C, to a maximum value of 460 MPa at 700 °C. Also, the effect of positive  $\gamma'/\gamma$  lattice misfit in Co-Al-W based alloys with quaternary additions of Ta, Mo, Ni, and Cr, on high temperature creep has been discussed in detail in a recent paper [Titus et.al. (2012)]. The reported creep testing results indicate that there is a strong preference for direction coarsening of  $\gamma'$  precipitates along the applied stress direction, in agreement with similar observations of directional coarsening in a Ni base alloys with a positive  $\gamma'/\gamma$  misfit. The design of the next generation of Co base alloys, is expected to focus on developing microstructures with a negative  $\gamma'/\gamma$  misfit which can enhance their creep resistance. Further reduction in the  $\gamma/\gamma'$  lattice mismatch by suitable alloying can lower the interfacial energy, leading to enhanced microstructural stability against  $\gamma'$  precipitate coarsening.

Using the experimental coarsening data for  $\gamma'$  precipitates within the framework of the modified LSW model for non-dilute solutions, the diffusivity of the rate-limiting solute, W, and the  $\gamma/\gamma'$  interfacial energy, has been determined for the Co-10Al-10W alloy. Additionally, by incorporating the Cahn-Hilliard approximation, the relative values of the  $\gamma/\gamma'$  interfacial energy at the annealing temperatures of 800 °C and 900 °C has also been estimated. The application of the Cahn-Hilliard approximation requires the compositional profile across the  $\gamma/\gamma'$  interface, and this has been experimentally determined in the present study at high spatial resolution from APT investigations. The resultant  $\gamma/\gamma'$  interfacial energy at 800 °C and 900 °C was determined to be 19 and 10 mJ/m<sup>2</sup> respectively, and is comparable to values reported in the literature for  $\gamma/\gamma'$  interfaces in nickel base superalloys. The sensitivity of the calculated value of the  $\gamma/\gamma'$  interfacial energy for the Co-10Al-10W alloy depends on the accuracy of the experimentally determined matrix and precipitate compositions, as well as the calculated rate constants based on the coarsening data. A high degree of confidence can be placed on the value of the phase compositions since these values have been determined using APT which has been proven as an accurate tool for such analysis. Statistical inaccuracies arising from the measurement of the precipitate sizes from the SEM and TEM images is expected to be relatively small since a large dataset has been used to determine the average values. Thus, the error in the value of interfacial energy is expected to be relatively small. The only discrepancy in the quantification of interfacial energy can arise from the value of diffusion exponent that has been adopted from the published literature [Ravi et.al. (2011)].

Additionally, the coupling of Cahn-Hilliard approximation with concentration profile across the  $\gamma/\gamma'$  interface obtained from APT has provided the gradient energy coefficient ( $\chi$ ) which forms an integral part of phase field simulations of precipitation processes. The estimated value of  $\chi$  in the present study nearly matches with that evaluated earlier [Ardell (2012)] for coherent  $\gamma/\gamma'$  interfaces in case of nickel base alloys.

There is an experimentally observed difference in the inter-precipitate distances between  $\gamma'$  precipitates at 800 °C and 900 °C, resulting from the change in volume fraction of precipitates at these two annealing temperatures. This is coupled with enhanced partitioning of W between the  $\gamma$  and  $\gamma'$  phases at the lower annealing temperature (800 °C), as indicated by APT results, leading to a higher degree of lattice mismatch between the two phases. Within the limits of  $\gamma$ - $\gamma'$  coherency regime, the larger lattice mismatch results in higher strain energy in the inter-leaving  $\gamma$  matrix. Hence, a combined effect of narrower inter-precipitate distances and higher elastic strain energy leads to enhanced coalescence of  $\gamma'$  precipitates at 800 °C, presumably removing the elastically strained matrix between two precipitates.

Apart from a detailed characterization of the  $\gamma$ / $\gamma'$  microstructure and associated solute partitioning between the two phases at elevated temperatures, this article quantifies the coarsening kinetics of  $\gamma'$  precipitates at the annealing temperatures of 800 °C and 900 °C in a Co-10Al-10W alloy. Furthermore, this paper presents calculations of the  $\gamma$ / $\gamma'$  interfacial energy as well as the gradient energy term associated with these interfaces within the framework of the Cahn-Hilliard approximation. These results serve as critical inputs for both models of microstructural evolution as well as the future development of Co base alloys with further reduced  $\gamma'$  coarsening rates and optimized microstructures.

#### **4.2.8. Task H: Mechanism of Nano-scale precipitation in soft magnetic alloys**

The role of the solute elements, copper and niobium, on the different stages of de-vitrification or crystallization of two amorphous soft magnetic alloys,  $\text{Fe}_{73.5}\text{Si}_{13.5}\text{B}_9\text{Nb}_3\text{Cu}_1$ , also referred to as FINEMET, and a  $\text{Fe}_{76.5}\text{Si}_{13.5}\text{B}_9\text{Cu}_1$  alloy, a model composition without Nb, has been investigated in detail by coupling atom probe tomography and transmission electron microscopy. The effects of copper clustering and niobium pile-up at the propagating interface between the  $\alpha$ - $\text{Fe}_3\text{Si}$  nanocrystals and the amorphous matrix, on the nucleation and growth kinetics has been addressed. The results demonstrate that while Cu clustering takes place in both alloys in the early stages, the added presence of Nb in FINEMET severely restricts the diffusivity of solute elements such as Cu, Si, and B. Therefore, the kinetics of solute partitioning and mobility of the nanocrystal/amorphous matrix interface is substantially slower in FINEMET as compared to the  $\text{Fe}_{76.5}\text{Si}_{13.5}\text{B}_9\text{Cu}_1$  alloy. Consequently, the presence of Nb limits the growth rate of the  $\alpha$ - $\text{Fe}_3\text{Si}$  nanocrystals in FINEMET and results in the activation of a larger number of nucleation sites, leading to a substantially more refined microstructure as compared to the  $\text{Fe}_{76.5}\text{Si}_{13.5}\text{B}_9\text{Cu}_1$  alloy.

##### *4.2.8.1. Results*

Atom probe tomography (APT) reconstructions from the melt-spun sample of the FINEMET ( $\text{Fe}_{73.5}\text{Si}_{13.5}\text{B}_9\text{Nb}_3\text{Cu}_1$ ) alloy, exhibited a uniform distribution of Fe and other alloying elements (Figs. 1(a) and (b)). On annealing at 400°C for 60 minutes, Cu-rich clusters form within the amorphous matrix due to the immiscibility of Cu in the Fe-base matrix. The number density of

Cu-rich clusters calculated from the APT reconstruction is  $9.7 \times 10^{23} \text{ m}^{-3}$ . Such Cu-rich cluster results were also seen in a Fe-Si-B-Cu system after similar annealing (410 °C for 60 min.). Additionally, these Cu clusters have been reported to act as potential heterogeneous nucleation sites for nucleation of  $\alpha$ -Fe<sub>3</sub>Si nanocrystals within the amorphous matrix [Ayers et.al. (1998)]. Thus the kinetics of Cu clustering contribute to the volume fraction and growth of Fe<sub>3</sub>Si crystals.

The second set of annealing studies was carried out for both alloy compositions at 550°C for 10 minutes. Based on TEM diffraction evidence of Fe<sub>76.5</sub>Si<sub>13.5</sub>B<sub>9</sub>Cu<sub>1</sub> it can be concluded that the nanocrystalline grains belong to the  $\alpha$ -Fe<sub>3</sub>Si phase and their size range is 50 – 100 nm. The size of  $\alpha$ -Fe<sub>3</sub>Si nanocrystals formed in the case of the FINEMET alloy are in the range of 5-10 nm, an order of magnitude smaller than those formed in the Fe<sub>76.5</sub>Si<sub>13.5</sub>B<sub>9</sub>Cu<sub>1</sub> alloy after an identical annealing treatment.

APT studies of the 550 °C/10mins (short duration annealing) annealed condition for both alloys was carried out with the objective of determining the partitioning of the solute elements across the interface between the nanocrystals and the amorphous matrix as well as to get further insight into the size and enrichment within the Cu-rich clusters. The cluster number density of 5 at% Cu clusters has been calculated to be  $2.3 \times 10^{23} \text{ m}^{-3}$  in case of both Fe<sub>76.5</sub>Si<sub>13.5</sub>B<sub>9</sub>Cu<sub>1</sub> and FINEMET alloys. The number density of  $\alpha$ -Fe<sub>3</sub>Si nanocrystals in case of Fe<sub>76.5</sub>Si<sub>13.5</sub>B<sub>9</sub>Cu<sub>1</sub> has been calculated to be approximately  $2 \times 10^{22} \text{ m}^{-3}$  while in case of FINEMET it was calculated to be  $6.8 \times 10^{22} \text{ m}^{-3}$  (varies by a factor of 3). While the  $\alpha$ -Fe<sub>3</sub>Si nanocrystals appear to be associated with Cu-rich clusters in both alloys, the substantial difference in number densities of 5 at% Cu clusters versus that of the  $\alpha$ -Fe<sub>3</sub>Si nanocrystals indicates that all 5 at% Cu clusters are not acting as heterogeneous nucleation sites for nanocrystals. The number densities of the 20 at% Cu clusters are  $4.5 \times 10^{22} \text{ m}^{-3}$  in the case of Fe<sub>76.5</sub>Si<sub>13.5</sub>B<sub>9</sub>Cu<sub>1</sub> and  $4.7 \times 10^{22} \text{ m}^{-3}$  in the case of the FINEMET alloy. It can be concluded that the most enriched Cu-rich clusters, containing at least 20 at % Cu, are associated with  $\alpha$ -Fe<sub>3</sub>Si nanocrystals. Furthermore, these APT results also reveal that  $\alpha$ -Fe<sub>3</sub>Si nanocrystals have grown substantially larger in the case of the Fe<sub>76.5</sub>Si<sub>13.5</sub>B<sub>9</sub>Cu<sub>1</sub> alloy compared with the FINEMET alloy for the same annealing treatment, corroborating the TEM results. These results clearly indicate the significant role played by Nb in constraining the growth of the  $\alpha$ -Fe<sub>3</sub>Si nanocrystals, since the only difference between the two alloy compositions is the absence of Nb in the Fe<sub>76.5</sub>Si<sub>13.5</sub>B<sub>9</sub>Cu<sub>1</sub> alloy.

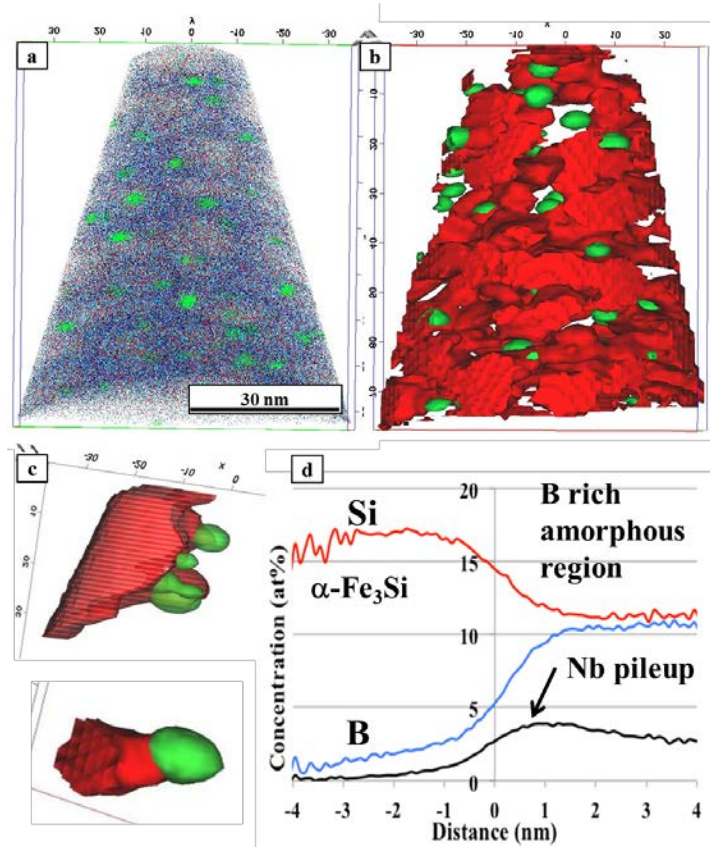


**Figure 12:** APT of Fe-Si-B-Cu-Nb after annealing at 550 °C for 15 minutes.

(a) shows the APT reconstruction of the FINEMET alloy after this annealing and shows the higher number density of nucleated Fe<sub>3</sub>Si crystals as compared after 10 minutes. (b) and (c) shows clear examples of side nucleation of Fe<sub>3</sub>Si from Cu clusters supporting Hono's model. (d) shows a proxigram of the Fe<sub>3</sub>Si interface with the amorphous matrix and reveals a clear Nb pileup at the interface.

Furthermore, it appears that the enrichment of Cu-rich clusters is also dependent on the presence of Nb in the alloy during short term annealing ( $\leq 10\text{min}/550\text{ }^{\circ}\text{C}$ ). Thus, in the case of the Fe<sub>76.5</sub>Si<sub>13.5</sub>B<sub>9</sub>Cu<sub>1</sub> alloy, the Cu-rich cluster exhibits a maximum core concentration of ~90 at % Cu while in the case of the FINEMET alloy, the Cu-rich clusters exhibit a much lower maximum core concentration of ~55 at % Cu.

Proxigram composition profiles clearly show that while Si partitioning is significant in the case of the Fe<sub>76.5</sub>Si<sub>13.5</sub>B<sub>9</sub>Cu<sub>1</sub> alloy, locally changing from ~18 at% Si to ~10 at% Si across the nanocrystal/amorphous matrix interface, it is negligibly small in case of FINEMET (~14at% Si constant across the interface). Similarly, B partitioning across the nanocrystal/amorphous

interface is also substantially more, changing from ~2 at% B to ~15 at% B in case of the Fe<sub>76.5</sub>Si<sub>13.5</sub>B<sub>9</sub>Cu<sub>1</sub> alloy compared with FINEMET (~2 at% B to ~7.5 at% B). A distinct partitioning of Nb can also be observed in the case of the FINEMET alloy. The general partitioning trend appears to be an enrichment of B and Nb in the amorphous phase accompanied by partitioning of Si in the growing Fe<sub>3</sub>Si phase. Annealing the FINEMET alloy at 550 °C for 15 minutes resulted in substantial microstructural changes from the 10 minutes annealing case. Thus, TEM bright-field and dark-field micrographs indicate that after 15 minutes annealing,  $\alpha$ -Fe<sub>3</sub>Si nanocrystals are 10-15 nm in size and the number density of crystals has greatly increased compared to the 10 min. heat treatment. After an even longer term of annealing at 550 °C for 60 minutes, the size range of  $\alpha$ -Fe<sub>3</sub>Si nanocrystals and their number density does not change significantly.

The APT analysis of the 550 °C/15mins annealed FINEMET alloy (Fig. 12) confirms a significant change in the volume fraction of  $\alpha$ -Fe<sub>3</sub>Si nanocrystals between 10 minutes and 15 minutes of annealing. Fig. 12(a) shows the Cu ions (green), Si ions (red), B ions (blue), and Nb ions (black) within the 3D volume of an atom probe reconstruction for this heat-treatment. Fig. 12(b), an APT reconstruction showing regions of more than 5 at% Cu (Cu-rich clusters in green) and less than 5 at% B ( $\alpha$ -Fe<sub>3</sub>Si regions in red) isosurfaces, clearly reveal that there is a larger volume fraction of  $\alpha$ -Fe<sub>3</sub>Si nanocrystals after 550 °C/15mins annealing compared with 10 minutes annealing at the same temperature. It should be noted that the larger volume fraction of the crystalline phase led to overlaps of the 5 at% B isosurfaces, giving the impression of an interconnected network of the crystalline  $\alpha$ -Fe<sub>3</sub>Si phase. There are two noteworthy points regarding these composition profiles. Firstly, Si partitioning across the nanocrystal/amorphous matrix interface locally changed from ~17 at% Si to ~11 at% Si, while B changed from ~1 at% B to ~10 at% B. Thus it is clear that both Si and B have partitioned more than what was observed after 10mins, preferably due to the increased volume fraction of  $\alpha$ -Fe<sub>3</sub>Si nanocrystals. Secondly, the Nb profile clearly shows a distinct pileup at this interface, which can act as a diffusion barrier to the growth of the  $\alpha$ -Fe<sub>3</sub>Si nanocrystals.

The results of longer term annealing of the Fe-Si-B-Cu and FINEMET alloys at 550 °C for 60 mins have been compared by TEM and APT. Interestingly, comparing the bright-field TEM images from the Fe-Si-B-Cu alloy for 550 °C/60 mins annealing reveals that the nanocrystals embedded in the amorphous matrix were about twice the size as compared with those imaged after 550 °C/10 mins. Also, the atom probe composition profiles for these phases exhibit significant differences. The composition profiles for Si and B across the crystal/amorphous interface clearly reveal that the  $\alpha$ -Fe<sub>3</sub>Si crystal contains ~19 at% Si after 550 °C/60 mins annealing, while the B-enriched amorphous phase contains ~25 at% B. Furthermore, the Si content within the amorphous matrix and B content within the  $\alpha$ -Fe<sub>3</sub>Si crystal, both are nearly zero after the 500 °C/60 mins anneal. Thus, the partitioning of Si across the  $\alpha$ -Fe<sub>3</sub>Si crystal/amorphous interface, as well as the B partitioning across the same interface are substantially greater than that observed after 550 °C/10 mins annealing (~18 at% Si to ~10 at% Si and ~2 at% B to ~15 at% B across the nanocrystal/amorphous matrix interface). Another point to note is that unlike the local equilibrium established near the crystal/amorphous matrix interface in case of 550 °C/10 mins annealing, after the longer term isothermal anneal for 60 mins, there is long-range equilibrium within both the crystalline and amorphous phases. From the composition profiles across the Cu cluster/ $\alpha$ -Fe<sub>3</sub>Si crystal interface; the Cu cluster is nearly elemental (~100

at%) Cu after the longer term anneal, as well as long-range equilibrium has been established in terms of compositional partitioning across this interface.

APT results from the 550 °C/60 mins annealed FINEMET alloy sample reveal the Si-rich nanocrystals, presumably corresponding to the  $\alpha$ -Fe<sub>3</sub>Si phase are highly refined in size and separated from each other by an amorphous wetting layer in between. From the solute partitioning across the interface using composition profiles for B, Si, Nb, and Cu it is clear that the large B-rich region contains ~ 26 at% B with no other solute atoms in any appreciable amount, indicating that this is possibly a grain of the Fe<sub>3</sub>B phase, reported to form in FINEMET on long term annealing [Zhang(2005)]. Based on the composition profiles across the interface between the  $\alpha$ -Fe<sub>3</sub>Si nanocrystals and the thin wetting amorphous layer separating them it can be concluded that the  $\alpha$ -Fe<sub>3</sub>Si phase contains ~15 at% Si and also contains ~2 at% of both B and Nb. This is consistent with the composition profiles observed in case of the interface between the  $\alpha$ -Fe<sub>3</sub>Si phase and the Fe<sub>3</sub>B crystal. The amorphous wetting layer separating these  $\alpha$ -Fe<sub>3</sub>Si nanocrystals has a composition of ~15 at% B, ~12 at% Nb, and ~10 at% Si. Therefore, it should be noted that while the amorphous phase separating the  $\alpha$ -Fe<sub>3</sub>Si nanocrystals contain a substantial amount of Si and Nb, the grains of the Fe<sub>3</sub>B phase, that form on long term annealing, does not contain any Si or Nb.

#### 4.2.8.2. Discussion

The nucleation and growth of the  $\alpha$ -Fe<sub>3</sub>Si nanocrystals depends on the diffusion of different atomic species involved, in both crystalline as well as amorphous phases. Diffusion in amorphous materials is dependent on the fraction of excess free volume in these materials, the equivalent of lattice vacancies in crystalline materials [Cantor et.al. (1983), Dorner et.al. (1991) and Horva et.al. (1990)]. In the present case, the ribbons were synthesized by a non-equilibrium melt spinning process. Due to the nature of this process, all the as melt-spun samples are expected to contain substantial amounts of excess free volume. During the process of annealing, in the early stages, diffusion of atoms is rapid due to this excess free volume and a coupled process of atomic diffusion as well as the annihilation of free volume occurs simultaneously [Cantor (1983)]. At later stages of annealing, all the excess free volume gets either annihilated or homogeneously re-distributed and the amorphous phase is structurally relaxed. Therefore, diffusion becomes very sluggish after structural relaxation of amorphous phase at longer annealing time periods [Cantor et.al. (1983)]. This phenomena has been previously reported by measuring the diffusivity of Fe in as-quenched Fe<sub>40</sub>Ni<sub>40</sub>B<sub>2</sub> amorphous alloys, and the observations indicated a reduction in diffusivity of Fe as a function of annealing temperature [Horvath et.al. (1985)]. The relaxation effects in the present alloy systems are further discussed below.

In the initial stages of annealing (400 °C/10 min), Cu clustering is observed in both Fe<sub>76.5</sub>Si<sub>13.5</sub>B<sub>9</sub>Cu<sub>1</sub> and Fe<sub>76.5</sub>Si<sub>13.5</sub>B<sub>9</sub>Cu<sub>1</sub>Nb<sub>3</sub> (FINEMET) alloys and can be attributed to the positive enthalpy of mixing for Cu-Fe which is essentially an immiscible system. Thus, the negligible solubility of Cu in the parent Fe-base amorphous matrix becomes a strong driving force for cluster formation. The clusters formed at a low temperature (400 °C), substantially

below the crystallization temperature of the  $\alpha$ -Fe<sub>3</sub>Si phase. Thus, the results are in good agreement with previous reports that Cu clustering occurs prior to crystallization [Ayers et.al. (1998)]. It has also been reported by several authors that Cu clusters act as heterogeneous nucleation sites for the precipitation of the  $\alpha$ -Fe<sub>3</sub>Si phase. The results presented here demonstrate a clear association between Cu-rich clusters and  $\alpha$ -Fe<sub>3</sub>Si nanocrystals, confirming the role of the former as heterogeneous nucleation sites for nanocrystals. Furthermore, the relatively larger volumes of the APT reconstructions clearly show that the Cu-rich clusters are joined to the surface of the  $\alpha$ -Fe<sub>3</sub>Si nanocrystals, in agreement with the model proposed by Hono et. al. [Hono et.al. (1999)] and not with the model proposed by Ayers et. al. [Ayers et.al. (1998)]. One report also indicates a possible crystallographic orientation relationship between Cu-rich clusters and  $\alpha$ -Fe nanocrystals in a soft magnetic Fe-Zr-B-Cu alloy [Zhang et.al. (2005)], presumably dictated by the low interfacial energy of certain well-matched planes between the two phases.

The results presented in this paper allow a direct comparison of Cu-clustering process in FINEMET alloy versus the model Fe<sub>76.5</sub>Si<sub>13.5</sub>B<sub>9</sub>Cu<sub>1</sub> alloy, a similar alloy but not containing Nb. The APT results for short term annealing duration ( $\leq 10$  min) clearly indicate that for identical annealing conditions, both the size of Cu-rich clusters is smaller as well as their compositions are less enriched in the case of Nb-containing FINEMET compared to the Fe<sub>76.5</sub>Si<sub>13.5</sub>B<sub>9</sub>Cu<sub>1</sub> alloy. This indicates that the diffusion of Cu is restricted by the presence of Nb. Therefore, in case of the Fe<sub>76.5</sub>Si<sub>13.5</sub>B<sub>9</sub>Cu<sub>1</sub> alloy, Cu can diffuse rather rapidly and form highly enriched Cu-clusters in the initial stages of annealing before annihilation of free volume takes place, restricting overall diffusion kinetics. On the other hand, Cu diffusion is restricted in the presence of Nb for the case of the FINEMET alloy, and thus the amorphous phase is structurally relaxed before a sufficient number of relatively larger size Cu-rich clusters can form. As noted earlier, these Cu-rich clusters can act as heterogeneous nucleation sites for  $\alpha$ -Fe<sub>3</sub>Si nanocrystals. However, the efficacy of Cu clusters as heterogeneous nucleation sites appears to be directly dependent on the level of Cu-enrichment. Thus, the results presented in this study clearly indicate that only the relatively higher Cu containing clusters (with at least 20 at%Cu) act as potent  $\alpha$ -Fe<sub>3</sub>Si nucleation sites. This is further confirmed by the composition profiles across the  $\alpha$ -Fe<sub>3</sub>Si nanocrystal/Cu cluster/amorphous matrix, wherein the Cu-rich cluster in the case of the Fe<sub>76.5</sub>Si<sub>13.5</sub>B<sub>9</sub>Cu<sub>1</sub> alloy reaches a peak composition  $\sim 90$  at%Cu at its core, while in the case of FINEMET the peak composition achieved at the core of the Cu-rich cluster is only  $\sim 55$  at%Cu. Additionally, it is also interesting to note that Nb not only restricts the diffusivity of Cu, but also the other elements, such as Fe and Si. Therefore, in the case of the Fe<sub>76.5</sub>Si<sub>13.5</sub>B<sub>9</sub>Cu<sub>1</sub> alloy, the absence of Nb, results in much more rapid growth of the  $\alpha$ -Fe<sub>3</sub>Si nanocrystals compared to FINEMET.

Crystallization in the case of the Fe<sub>76.5</sub>Si<sub>13.5</sub>B<sub>9</sub>Cu<sub>1</sub> alloy is growth dominated with relatively fewer  $\alpha$ -Fe<sub>3</sub>Si nuclei growing rather rapidly, the growth being dominated by diffusion of Si into the nanocrystals coupled with the diffusion of B out of the nanocrystals. In contrast, crystallization behavior of the Nb containing FINEMET is rather different. Cu-rich clusters form in this alloy, but the slower diffusion of Cu results in smaller cluster sizes as well as less enrichment in these clusters. Due to the less pronounced enrichment of Cu in these clusters as well as their smaller sizes, many of these clusters may not act as potential  $\alpha$ -Fe<sub>3</sub>Si nucleation sites at the early stages of annealing (e.g. 550 °C/10 mins). Furthermore, in cases where one of these Cu-rich clusters nucleates a  $\alpha$ -Fe<sub>3</sub>Si nanocrystal, Nb is rejected by the growing nanocrystal and piles up at the amorphous/crystalline interface, acting as a diffusion barrier and substantially

reducing the growth rate. These results clearly reveal the Nb pile up in substantially larger scale compared to those shown previously in one-dimensional atom probe studies on partially de-vitrified FINEMET alloys [Hono et.al. (1999)]. After annealing the FINEMET alloy for 15 min at 550 °C, there are many clusters that are both substantially enriched in Cu (greater than at least 20 at%) and of reasonable size (> 3nm), potent nucleation sites for  $\alpha$ -Fe<sub>3</sub>Si nanocrystals. Therefore, a large number of nucleation sites are activated while the growth of the  $\alpha$ -Fe<sub>3</sub>Si nanocrystals is still limited due to Nb pile-up at the nanocrystal/amorphous matrix interface. Furthermore, Nb also slows down diffusion of Si as well as B. The overall result is that a much more refined microstructure (compared to the Fe<sub>76.5</sub>Si<sub>13.5</sub>B<sub>9</sub>Cu<sub>1</sub> alloy) is obtained with an average  $\alpha$ -Fe<sub>3</sub>Si nanocrystal size ~15 nm.

Furthermore, it is interesting to note that the average size of nanocrystals remains nearly the same, even after prolonged annealing at the same temperature for 60 minutes. As mentioned earlier, the presence of excess free volume in the amorphous matrix promotes diffusion during the early stages of annealing, resulting in growth of the  $\alpha$ -Fe<sub>3</sub>Si nanocrystals. However, by the time these nanocrystals have grown to a certain size, the excess free volume of the amorphous matrix is largely annihilated or re-distributed and consequently restricts further diffusion of Fe, Si and Cu. This effect coupled with the reduced diffusivity of these elements in the presence of Nb leads to rather limited diffusion in the matrix during the later stages of annealing (> 60 mins). The microstructure reaches a steady state without exhibiting substantial change with increasing annealing time. Subsequently, annealing at 550 °C for extended time periods (~ 1 hr) can result in formation of other compounds, such as Fe<sub>3</sub>B, as reported previously [17]. Additionally, it should be noted that partitioning of Si and B between  $\alpha$ -Fe<sub>3</sub>Si nanocrystals and the adjacent amorphous matrix progressively increases after isothermal annealing at 550 °C (10 mins (Fig. 5(b) to 15 mins (Fig. 7(d)) and finally to 60 mins (Fig. 9(c)). Similarly, the partitioning of Si and B across the  $\alpha$ -Fe<sub>3</sub>Si crystal/amorphous interface in case of the Fe<sub>76.5</sub>Si<sub>13.5</sub>B<sub>9</sub>Cu<sub>1</sub> alloy also progressively increases from 550 °C/10 mins annealing (~18 at%Si to ~10 at%Si and ~2 at%B to ~15 at%B across the interface shown in Fig. 5(a)) to 550 °C/60 mins annealing (~19 at%Si to ~0 at%Si and ~0 at%B to ~25 at%B across the interface shown in Fig. 8(c)). Comparing these results for the FINEMET alloy with the Fe<sub>76.5</sub>Si<sub>13.5</sub>B<sub>9</sub>Cu<sub>1</sub> alloy clearly demonstrates the strong influence of Nb in reducing the diffusivity of other solute elements (Si, B, and Cu) in the amorphous matrix.

### 4.3. Thrust Area III: Three-dimensional (3D) Functionally-graded Hybrid Materials for Aerospace Structural Applications

#### 4.3.1. Task A: Metal-Ceramic Hybrids

##### 4.3.1.1. Nickel-TiC-Graphite Hybrids

###### 4.3.1.1.1. Laser Engineered Net Shaping (LENS<sup>TM</sup>)

The titanium carbide (TiC) reinforced nickel based composites used for 3D microstructural characterization were deposited using the laser engineered net shaping (LENS<sup>TM</sup>) process from a feedstock consisting of a blend of elemental nickel, titanium and nickel-coated graphite powders. The powders used for depositing the Ni-Ti-C composites consisted of commercially pure near

spherical Ni (40-150  $\mu\text{m}$ ), pure Ti (40-150  $\mu\text{m}$ ) and Ni coated graphite powders, which were premixed in a twin roller mixer with the nominal compositions 80Ni-10Ti-10C and 77Ni-3Ti-20C (refer to Ni-10Ti-10C and Ni-3Ti-20C for brevity). These composites were laser deposited in a cylindrical geometry of diameter 10 mm and height 10 mm. The LENST<sup>TM</sup> deposited *in situ* Ni-Ti-C composites were characterized by scanning electron microscopy (SEM) in FEI-Quanta Nova-SEM. X-ray diffraction analysis of deposits was performed using (1.54 Cu K $\alpha$ ) line of Rigaku Ultima III X-ray Diffractometer. Area fraction calculation of TiC and graphite reinforcements was done using ImageJ software, and an average of 50 SEM images were reported in this paper. The details of FIB serial sectioning and 3D reconstruction are explained in the next section.

#### 4.3.1.1.2. Dual Beam FIB-SEM Serial Sectioning Methodology:

This section will briefly describe the dual-beam FIB based serial sectioning methodology employed to study the 3D microstructure characterization of these Ni-Ti-C composites. A dual beam workstation (FEI Nova NanoSEM) equipped with a focused ion beam column employing a Gallium (Ga) liquid metal ion source, combined with a high-resolution field emission scanning electron microscope (FEG SEM) was used. Prior to the 3D serial sectioning, the stage was tilted to maintain the 52° angle between the FIB and SEM columns so that the sample surface of interest was oriented parallel to the ion beam during cross sectioning. A layer of platinum (Pt) was deposited on the top of region of interest, which serves not only as protection but also helps in minimizing curtaining effects and provides a sharp cutting edge during serial sectioning [Uchic et.al. (2006)]. Additionally, this Pt layer also acts as a fiducial marker during the 3D reconstruction process for proper alignment of the 2D SEM images. Prior to the serial-sectioning procedure, the sample is micro machined into a cantilever beam geometry using the dual-beam FIB, as shown in Fig. 1(b). This sample geometry has two main advantages: firstly it minimizes the redeposition of milled material onto the surface of interest, and secondly it eliminates the possibility of shielding of the detectors by the sample [Uchic et.al. (2006)]. An automated serial sectioning procedure was employed, using FEI's auto slice and view software. The use of an automated software routine ensures a consistent material removal rate during serial-sectioning, and also eliminates the need for human supervision and interaction, so that the experiment can run for substantially longer time periods resulting in a large number of serial sections and consequently larger 3D reconstructed volumes [Uchic et.al. (2006)].

#### 4.3.1.1.3. Three Dimensional (3D) Reconstruction:

The 2D image stack collected during the serial sectioning procedure was reconstructed in to a 3D object using the software package termed MIPAR<sup>TM</sup> (Materials Image Processing and Automated Reconstruction) based on a MATLAB platform, developed at The Ohio State University, and the commercially available AvizoFire 6.3 software. The entire 3D reconstruction procedure consists of (a) alignment of the stack, (b) cropping of a region of interest, (c) noise filtering/ thresholding, (d) segmentation, and (e) visualization. The first 4 steps were performed using MIPAR<sup>TM</sup> and AvizoFire 6.3 was used for 3D visualization. In MIPAR<sup>TM</sup>, an FFT filter was applied to minimize curtaining effects (artifacts) obtained from FIB serial sectioning. Thresholding of TiC and graphite phases was done by applying a Gaussian blur subtraction along with the global range thresholding filter prior to segmentation of individual features. Finally, this

entire post-processed 2D image stack was exported to AvizoFire 6.3 format for 3D visualization of TiC and graphite reinforcements.

#### *4.3.1.1.4. Microhardness and Tribological Properties:*

The micro-hardness was measured using a standard Vickers micro-hardness tester using 300g load. Sliding friction and wear testing was conducted with a Falex (Implant Sciences) ISC-200 pin-on-disk (POD) system at room temperature. The samples were openly exposed in lab air (~40% RH) during the tests. Tests were performed under a 1 N normal load with a 1.6 mm radius  $\text{Si}_3\text{N}_4$  ball, which correspond to an initial maximum Hertzian contact stress ( $P_{\max}$ ) of ~1.2 GPa. The sliding speed was fixed at 50 mm/sec. The ratio of tangential to normal load is the friction coefficient. At least three POD tests were run out to a total sliding distance of 140 m (steady-state friction behavior).

#### *4.3.1.1.5. Results*

X-ray diffraction (XRD) was done on the as-deposited Ni-Ti-C composites of nominal compositions Ni-10Ti-10C and Ni-3Ti-20C. In case of Ni-10Ti-10C, the primary diffraction peaks can be consistently indexed based on the face centered cubic (FCC) Ni phase and the  $\delta$ -TiC phase exhibiting the rocksalt (NaCl type) structure. In case of Ni-3Ti-20C, a peak at  $20\text{--}26^\circ$ , corresponding to the {0002} planes of graphitic carbon is clearly visible in addition to the FCC Ni and  $\delta$ -TiC peaks. The absence of peaks corresponding to any Ni-Ti intermetallic phases is also evident in these diffraction patterns indicating that there is no reaction between nickel and titanium, rather titanium and carbon react within a molten nickel pool to form TiC precipitates.

Backscattered SEM images from the Ni-10Ti-10C composite clearly exhibit the presence of TiC precipitates with two different morphologies and size-scales. The coarser and faceted carbides are likely to be the primary TiC precipitates while the finer scale needle-like carbides are likely to be eutectic TiC precipitates, homogeneously distributed within the nickel matrix.

Backscattered SEM images of the Ni-3Ti-20C composite clearly show the presence of TiC precipitates along with a substantial volume fraction of a phase exhibiting a black contrast, presumably corresponding to the graphitic phase revealed in the x-ray diffraction pattern. Ni-10Ti-10C exhibits approximately 17% (area fraction) of TiC whereas Ni-3Ti-20C exhibits approximately 8% graphite and 4% TiC. However, the focus of the present study is a more detailed 3D analysis of the microstructure via serial-sectioning in the dual-beam FIB and subsequent reconstruction of the 3D volume, as discussed below.

The reconstructed 3D volume corresponding to the Ni-10Ti-10C composite is shown in Fig. 13(a). A cropped version of the entire 3D volume is shown in Fig. 13(b) for better visualization purposes. In the cropped view, the primary TiC precipitates have been colored in green, while the eutectic TiC are represented in purple color. While the appearance of this 3D microstructure is rather complex (Figs. 13(a) and (b)) it clearly highlights the following salient aspects of this microstructure:

- a. The primary TiC precipitates exhibit a cuboidal morphology.

- b. The eutectic TiC precipitates appear to exhibit a plate-like morphology in most cases unlike the needle-like morphology revealed by 2D SEM observations. Some needle-like eutectic TiC precipitates are also visible in the 3D reconstruction.
- c. The eutectic TiC precipitates appear to be interconnected forming a 3D network with the larger primary TiC precipitates located at the nodes of this network.

The connectivity between the carbide precipitates is impossible to discern based on the 2D SEM images without the aid of the 3D reconstruction. The eutectic TiC precipitates that are connected to the primary TiC, possibly nucleated from the primary precipitate during solidification.

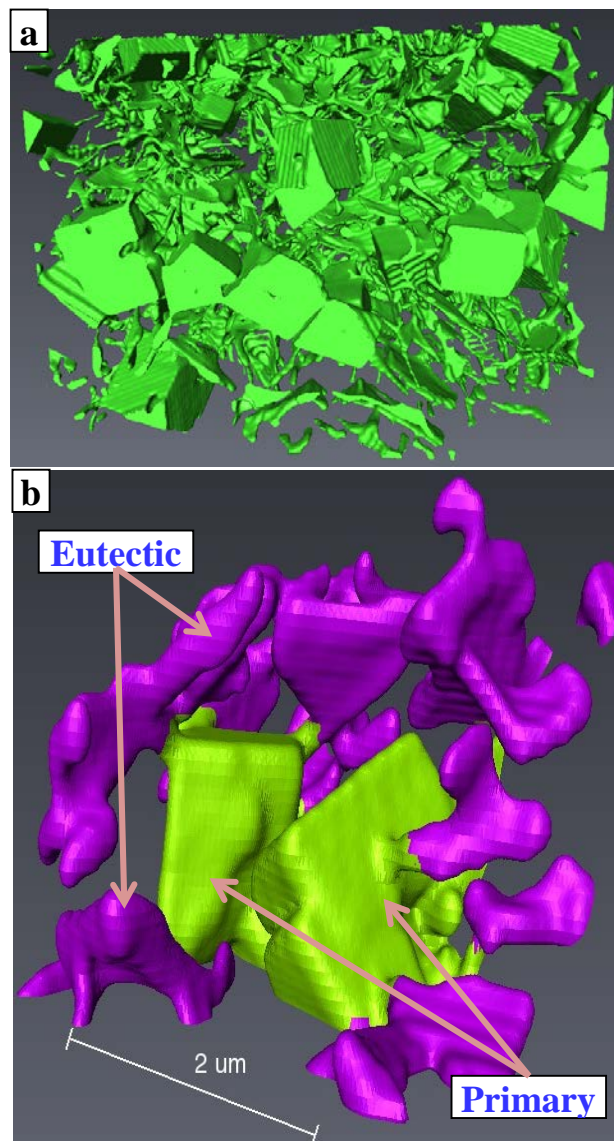


**Figure 13:** (a) 3D reconstruction of Ni-10Ti-10C composites obtained from the 2D SEM image stack (b) Cropped version of 3D reconstructed volume of Ni-10Ti-10C showing primary and eutectic TiCs.

The major challenge in 3D reconstruction of these Ni-3Ti-20C composites compared to the Ni-10Ti-10C composites is the presence of 2 different precipitates phases i.e. TiC and graphite. During post processing of 2D SEM images, both the phases (TiC and graphite) were thresholded differently and then exported to reconstruct the 3D volume. The carbide precipitates are clearly connected to each other and form a complex network in 3D. This connectivity between the carbide precipitates is nearly impossible to visualize based on the 2D SEM images. The distinction between the cuboidal primary TiC precipitates and the plate or needle-shaped eutectic TiC precipitates is more difficult in this case since the primary precipitates are smaller in size as clearly shown in the higher magnification views of cropped sections of the 3D reconstruction. Furthermore, most of the cuboidal primary TiC precipitates are engulfed by graphite bundles. There is a gap between the TiC precipitates and the graphite bundles, and it is very difficult to comment on their interconnectivity and association based on these images. The 3D reconstructions conclusively reveal the true nature of the connection between the carbide precipitates and the graphitic bundles in this microstructure. The eutectic TiC precipitates in case of the Ni-3Ti-20C composite exhibit both plate-like and needle-like morphologies. The volume fractions of the different phases, in both types of composites, have also been calculated using the 3D reconstructions. The results indicate that Ni-10Ti-10C exhibits approximately 17% of TiC whereas Ni-3Ti-20C exhibits approximately 7% graphite and 5% TiC which is in good agreement with the values computed from the 2D area fractions. Based on these phase fractions, it is possible to recalculate the nominal compositions of the two types of composites as Ni-17Ti-17C and Ni-5Ti-12C. These corrected composition values will be employed in the subsequent section discussing the sequence of phase evolution in these composites.

Modeling the sequence of phase evolution in the Ni-17Ti-17C and Ni-5Ti-12C composites has been carried out using a simple phase diagram analysis of the Ni-Ti-C ternary phase diagram. Therefore, isothermal sections of the Ni-rich corner of the Ni-Ti-C phase diagram, at four different temperatures, computed using commercially available solution thermodynamic models (PANDAT™ from CompuTherm). At a very high temperature of 2725 °C, both compositions lie in the single liquid phase region. Reducing the temperature to 2500 °C results in the Ni-17Ti-17C composition lying within the liquid + primary TiC two-phase field suggesting that primary TiC precipitates will nucleate and grow in this composite. Subsequent continuous cooling of the same composition to lower temperatures increases the volume fraction of the primary TiC precipitates and eventually at a temperature of ~ 1280 °C, the remaining liquid in the system undergoes a pseudo-binary eutectic solidification to form eutectic Ni + eutectic TiC. Contrastingly, the Ni-5Ti-12C composition exhibits a different sequence of phase evolution, starting with a single liquid phase at high temperatures (>2500 °C). Continuous cooling of this composition initially results in the primary solidification of TiC at temperatures ~ 1800 °C and at even lower temperatures ~ 1500 °C, this composition enters a liquid + TiC + C three phase field indicating the formation of a second solidification product, C (graphite), in the liquid. Eventually at an even lower temperature ~ 1280 °C, the remaining liquid in this case too undergoes a pseudo-binary eutectic solidification to form eutectic Ni + eutectic TiC.

While the sequence of phase evolution can be predicted based on the isothermal sections of the ternary Ni-Ti-C phase diagrams, the resultant microstructure is difficult to visualize without the 3D reconstructions. Thus, these reconstructions lead to a better understanding of the shape, size, distribution, and connectivity between the different phases evolving during the solidification of both types of composites (Ni-17Ti-17C and Ni-5Ti-12C). Within the liquid melt pool consisting

of Ni+Ti+C, the primary TiC appears to be the first solid phase to form during solidification for both types of composites. These primary carbide precipitates exhibit a cuboidal morphology, presumably dictated by surface energy criteria. Continuous cooling results in growth of these cuboidal primary TiC precipitates within the retained Ni-Ti-C liquid, depleting it of Ti and C. In case of the Ni-17Ti-17C composition, the retained liquid eventually undergoes eutectic solidification into Ni + eutectic TiC. The cuboidal primary TiC precipitates act as heterogeneous nucleation sites for the eutectic carbide precipitates, resulting in the formation of a network of eutectic carbide precipitates linked at their nodes by the primary carbide precipitates, as clearly revealed by the 3D reconstructions shown in Fig. 3. The regions in between this network form the pure Ni grains. In contrast, while the Ni-5Ti-12C composition also starts its solidification sequence by forming cuboidal primary TiC precipitates, the remaining liquid does not directly undergo eutectic solidification, but rather forms a second solidification phase within the liquid, a graphitic carbon phase. This graphitic carbon phase forms directly in the liquid Ni-Ti-C and nucleates and grows preferentially at the primary TiC precipitates, eventually encompassing the entire carbide precipitate. Eventually, at even lower temperatures, the retained liquid undergoes a pseudo-binary eutectic solidification to form Ni + eutectic TiC precipitates. The eutectic carbides also appear to heterogeneously nucleate and grow from the cuboidal primary carbide precipitates and form an interconnected three dimensional network linked by the cuboidal primary carbides at the nodes.

The Vickers microhardness values for the three Ni-Ti-C composites and pure Ni have been listed in Table I. Comparing Vickers microhardness values, the Ni-10Ti-10C composite exhibited a substantially higher hardness of 370 VHN as compared to 165 VHN for the LENS<sup>TM</sup> deposited pure Ni and 240 VHN for the Ni-3Ti-20C composite respectively. These microhardness values clearly show a trend of decreasing hardness as a function of increasing C/Ti ratio in the composite. The high volume fraction of titanium carbides (both primary and eutectic), in case of the Ni-10Ti-10C composite resulted in the higher microhardness value. Comparing results of POD tribometry studies carried out on the LENS deposited Ni-10Ti-10C, Ni-3Ti-20C composites and also pure Ni samples, it is clear that the presence of the TiC (and graphite) phases in these composites were beneficial in reducing the friction coefficient with respect to the pure Ni sample. While the presence of TiC reduces the coefficient of friction, as observed in case of the Ni-10Ti-10C composite, the presence of the lubricious graphitic phase can play a more dominant role in reducing the friction for these composites, as clearly evident from the friction curve for the Ni-3Ti-20C composite. However, the most promising composite appears to be the Ni-3Ti-20C composite that exhibits a drastic reduction in friction coefficient (~0.1) as compared to any of the other composites [Gopagani et.al. (2013)], mainly due to the presence of a substantial fraction of the graphitic phase as well as TiC precipitates. Thus, these Ni-Ti-C composites, especially the Ni-3Ti-20C composite, appear to be promising materials for surface engineering applications requiring high hardness with improved solid lubrication.

#### 4.3.1.1.6. Conclusions

Novel in situ Ni-Ti-C composites have been deposited using the laser engineered net shaping (LENS<sup>TM</sup>) process. While the Ni-10Ti-10C composite exhibits a large volume fraction of primary cuboidal TiC precipitates as well as eutectic carbide precipitates, the Ni-3Ti-20C composite exhibits an additional graphitic phase. 3D microstructural characterization of these composites reveals the following salient features:

1. The Ni-10Ti-10C composite consists of a complex interconnected network of carbide precipitates with primary cuboidal TiC precipitates at the nodes of the 3D network, connecting plate-like (needle-like in some cases) eutectic TiC precipitates. The primary carbides appear to act as the heterogeneous nucleation sites for the eutectic carbides.
2. The Ni-3Ti-20C composite also consists of an interconnected network of carbides, comprising primary carbide precipitates at nodes with eutectic carbides connecting them, but the smaller scale cuboidal primary carbide precipitates in this case are engulfed by graphitic bundles, a second primary solidification product.

Such 3D characterization leads to a better understanding of the sequence of phase evolution during solidification in these novel composites. Tribological and mechanical property measurements reveal that the steady-state friction coefficients for these Ni-Ti-C composites are significantly lower than that of pure Ni, while their microhardness is substantially higher, making them promising candidates for surface engineering applications that require both solid lubrication and high mechanical hardness. Comparing the different Ni-Ti-C composites investigated in this study, the Ni-3Ti-20C composite appears to exhibit the best balance of properties with the lowest coefficient of friction as compared to pure Ni and Ni-10Ti-10C, and a microhardness that is greater than pure nickel, though being somewhat lower than the Ni-10Ti-10C composites.

More details can be found in [Borkar et.al. (2014)]

#### 4.3.2. Task B: Ceramic-Ceramic Hybrids

##### 4.3.2.1. *Ceramic coating infiltrated Carbon-Carbon Composites*

Carbon-carbon composites (CCC) are well recognized structural materials which are generally known for their high strength and thermal conductivity, low density, and open cell structure. They have attracted great interest for aerospace applications, such as bushings used in jet engines, and potentially in future hypersonic aircraft wing structures, which function in an oxidizing environment. The enhancement in thermal (oxidation) and wear resistance of CCC is desirable since carbon-based materials start to oxidize around 400 °C and uncoated bushings are susceptible to wear. To this end, thermodynamically stable protective oxide nanolaminates ( $ZnO/Al_2O_3/ZrO_2$ ) have been deposited by atomic layer deposition (ALD) to infiltrate porous CCC and graphite foams in order to improve their thermal stability and sliding wear resistance. It was determined with x-ray tomography imaging and energy dispersive x-ray spectroscopy mapping that ALD  $ZnO/Al_2O_3/ZrO_2$  nanolaminates and baseline  $ZrO_2$  coatings exhibited pore-filling down to  $\sim 55 \mu m$  and 1.5 mm in the porous CCC and graphite foam, respectively. Furthermore, x-ray diffraction and high resolution transmission electron microscopy determined that the {0002}-textured nanocrystalline  $ZnO$  (wurtzite), amorphous  $Al_2O_3$ , and {101}-textured tetragonal  $ZrO_2$  nanolaminates exhibited excellent coating conformality and uniformity inside the pores. A significant reduction in the sliding wear factor ( $2.3 \times 10^{-5}$  to  $4.8 \times 10^{-6} \text{ mm}^3/\text{N}\cdot\text{m}$ ) and friction coefficient (0.22 to 0.15) was observed with the ALD  $ZnO/Al_2O_3/ZrO_2$  nanolaminate in comparison to uncoated CCC. The mechanism for improved tribological properties was attributed to intrafilm shear (slip) of partial dislocations along the  $ZnO$  {0002} basal stacking faults by a dislocation glide process.

The ALD coatings exhibited excellent conformality and pore-filling down to ~55 microns into the CCC, shown in Figure 14, which no other existing coating technique can achieve, while simultaneously providing self-lubricating behavior in room and higher temperature (400 °C) environments.

TEM investigations of microstructural evolution during fretting wear determined that a mechanically mixed layer (MML) of ALD trilayer and *a*-C, shown in Figure 15, was responsible for the improvements in fretting wear compared to the uncoated CCC, which just showed an *a*-C layer. Inside the MML, a high density of ALD ZnO (0002) sliding/shear-induced stacking faults were observed in comparison to unworn ALD nanolaminates. Activating subsurface basal stacking faults in ALD ZnO promotes intrafilm shear/slip and hence improves wear. The slip of partial dislocations results from a dislocation glide process along the ZnO (0002) basal planes.

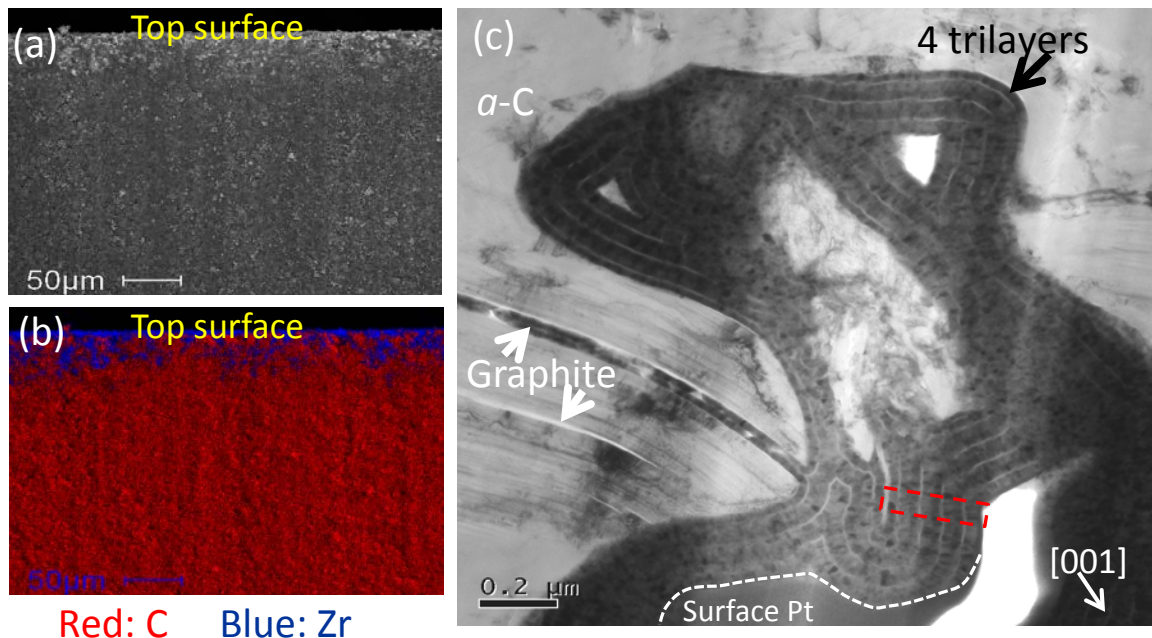


**Figure 14:** (a) Cross-sectional SEM and (b) corresponding EDS color map showing surface and subsurface atomic layer deposition (ALD)  $\text{ZrO}_2$  coating infiltration of CCC. (c) Cross-sectional TEM image of 4 ALD  $\text{ZnO}/\text{Al}_2\text{O}_3/\text{ZrO}_2$  trilayers (~220 nm overall thickness) showing excellent coating conformality/uniformity and infiltration (pore filling) of the CCC. The red rectangle shows the 4 trilayer sequence grown on the CCC with the brighter, white ~5 nm thick  $\text{Al}_2\text{O}_3$  layer serving as a useful marker to distinguish the trilayers. The dashed line represents the surface of the sample where the protective Pt was deposited.

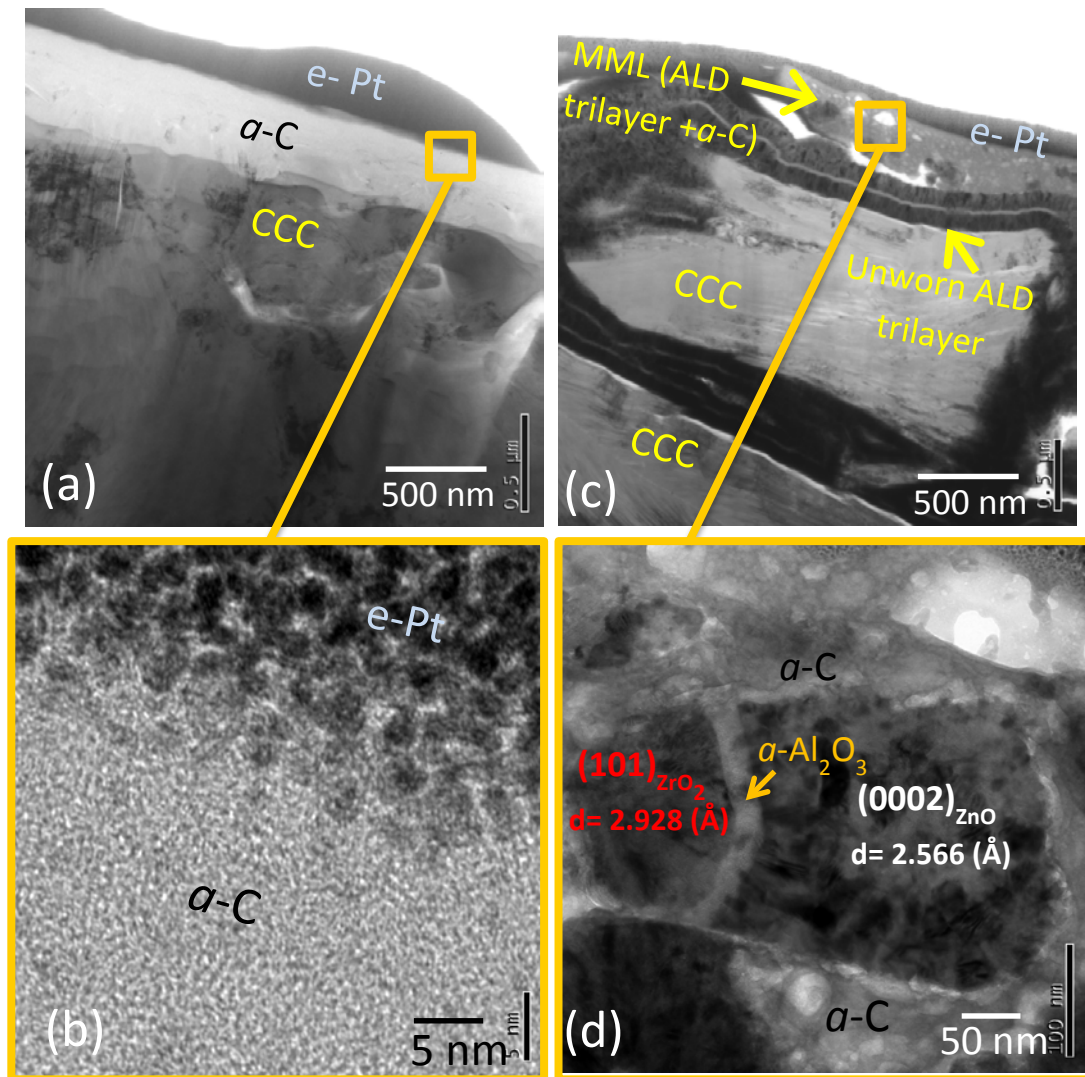


**Figure 15:** Low and high magnification cross-sectional TEM images of fretting wear surfaces and subsurfaces for (a+b) uncoated CCC, and (c+d) ALD coated  $\text{ZnO}/\text{Al}_2\text{O}_3/\text{ZrO}_2$  trilayer showing mechanically mixed layers (MML) resulting from fretting wear contact.

Thus, ALD  $\text{ZnO}/\text{Al}_2\text{O}_3/\text{ZrO}_2$  nanolaminate coatings are good candidates for providing low wear (and potentially high thermal/oxidation resistant) surfaces and interfaces in moving mechanical assemblies, such as CCC bushings that experience fretting wear. More details can be found in reference [Mohseni et.al. (2012)] and published patent [Scharf et.al. (2016)].

#### 4.3.2.1.2. Theoretical and experimental investigations on the mechanism of carbothermal reduction of zirconia

Zirconium carbide (ZrC) is an important ultrahigh temperature ceramic due to its refractory properties. It is commonly synthesized via carbothermal reduction of zirconia above 1657 °C according to the reaction  $\text{ZrO}_2(\text{s}) + 3\text{C}(\text{s}) \rightarrow \text{ZrC}(\text{s}) + 2\text{CO}(\text{g})$ . Contrary to this reaction, prior research indicates that carbon monoxide (CO) is the responsible species for carburizing  $\text{ZrO}_2$  to form ZrC. To explore this reaction pathway, investigations were performed by making two mixed phase pellets with 3 mol% yttria-stabilized zirconia (YSZ) and graphite. Both had an upper half made of YSZ. The lower half of one sample consisted of finely mixed YSZ and graphite powder whereas the other was pure graphite. Similar experiments were conducted with sintered YSZ pellets on top. After heat treatment at 1800 °C, X-ray diffraction analysis revealed higher ZrC conversion for the YSZ pellet face in direct contact with pure graphite. This contradicts previous work as one would assume higher ZrC yield for YSZ pellet in direct contact with YSZ/graphite mix as they produce more CO upon reaction. Lastly, diffusional experiments showed conversion to be highly localized to a depth of ~20  $\mu\text{m}$ . This is in close agreement with calculations for carbon diffusion in YSZ based on a diffusion coefficient ( $D$ ) =  $3 \times 10^{-14}$   $\text{m}^2/\text{sec}$ , which confirms solid-solid reaction rather than solid-gas reaction.

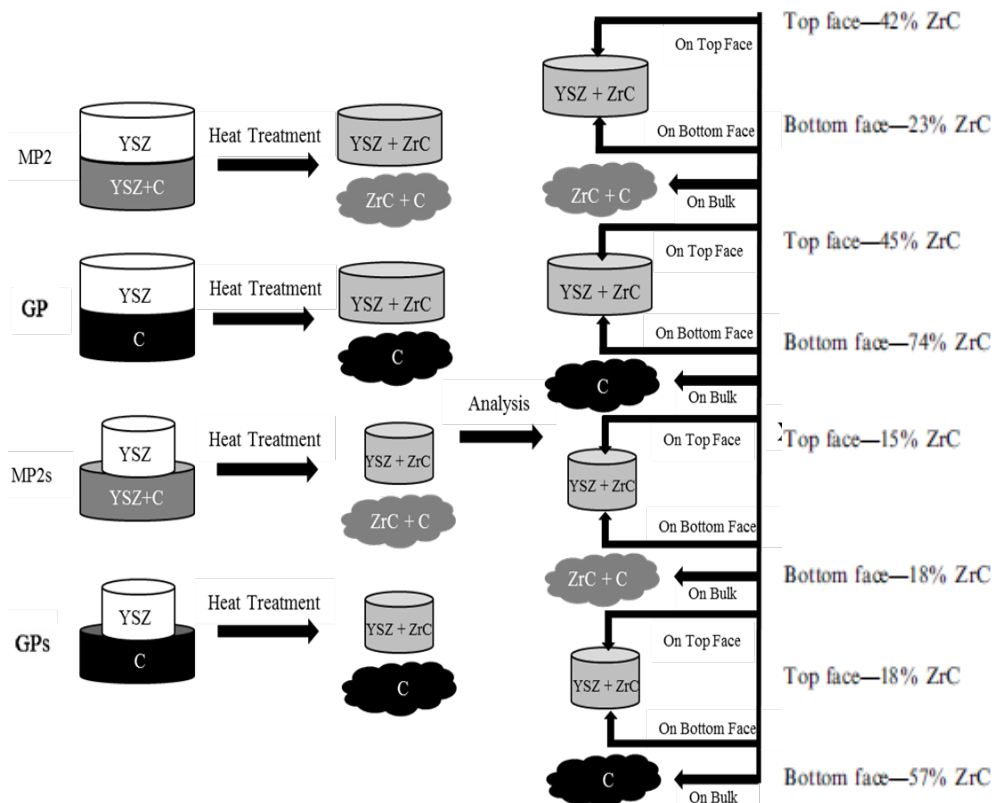


**Figure 16:** Flowchart showing the methodology in XRD analysis of four pellets before and after carbothermal reduction heat treatment. Shrinkage seen in top half of MP2s and GPs is due to prior sintering of the YSZ pellet. The cloud shape represents powder formed from bottom halves as they decompose after heat treatment. Mole percentages determined by XRD Rietveld analysis are listed for ZrC formed on the top and bottom faces of MP, GP, MPs and GPs.

#### 4.3.2.2. Bulk diffusion of C in YSZ pellets

The carbon diffusion coefficient in zirconia has been reported to be six orders of magnitude smaller than oxygen self-diffusion. This would indicate several orders of magnitude difference in diffusivity between C and CO through YSZ due to the gaseous nature of CO. Based on the recent work of Vykhotets et al [Diffusion of insoluble carbon in zirconium oxides, JETP Letters 93 (2011) 5–9] and utilizing their data, the diffusion coefficient of C in YSZ at 1800 °C is calculated to be  $3 \times 10^{-14}$  m<sup>2</sup>/sec. Using Fick's second law and this diffusion coefficient, the effective diffusion length of C in YSZ can be approximated to 25 μm for 1800 seconds at 1800 °C (calculated plots shown in Figure XX). According to these results at distances greater than 25 μm there should not be any ZrC formation due to lack of diffusing carbon. To confirm this experimentally, the top halves of MP, GP, MPs, and GPs were sliced radially to half their heights (~1.5 mm). After slicing, XRD scans were acquired from the exposed faces, while keeping the X-ray beam close to the geometric center. XRD scans were obtained from both faces for all the pellets. None of the scans show the dominant ZrC (111) peak at  $2\theta=33.2^\circ$ . On the contrary, all the peaks correspond to YSZ (monoclinic and tetragonal phases) confirming that no ZrC formed in the center, at least to these 1.5-2 mm depths. Figure XX theoretically shows for longer diffusion times of 3600 seconds (circles) to 5400 seconds (triangles), C cannot diffuse past 50 μm distance. These results further confirm that carbothermal reduction is more C driven than CO driven due to its slow diffusional nature. X-ray penetration depth calculations indicate that the diffraction analysis only examines approximately the first 16-20 μm of ZrO<sub>2</sub>/ZrC.

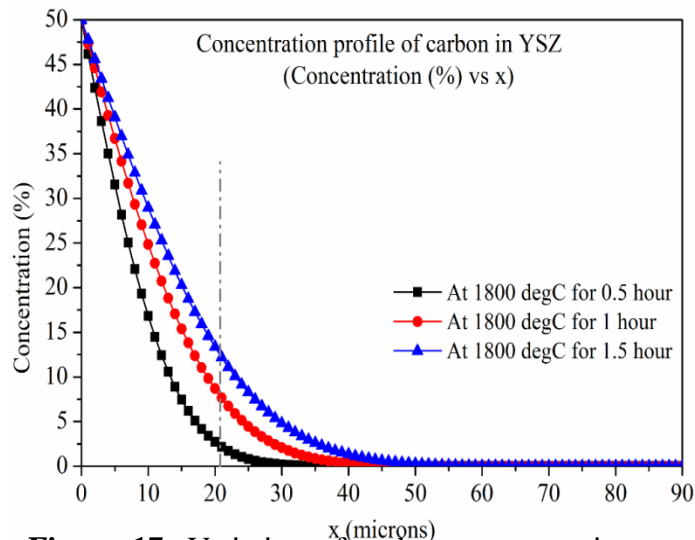


**Figure 17:** Variation of carbon concentration as a function of diffusion distance (x) in YSZ at 1800 °C. Curves are plotted for various diffusion times of 1800, 3600 and 5400 seconds. Vertical dotted line shows maximum distance to which X-rays penetrated based on diffraction data acquired from bottom and top faces of MP, GP, MPs and GPs top halves.

Surface diffusion of C in YSZ pellets: It was determined that the bottom half of MP acts as a strong source of CO and a weak source of C for diffusion into the top half. In contrast, GP acts as a strong C source and a weak CO source for its top half. In principle, during the course of the carbothermal reduction reaction, it is feasible that CO as a reaction product can be liberated from the sample and potentially form a sheath around the top YSZ pellet leading to radially inward diffusion. Similarly, C due to being a small and relatively mobile species can also diffuse to the top from surface sites on the pellet edges. These pathways can possibly cause a gradient in the amount of YSZ converted to ZrC along the sides of the pellet in addition to the aforementioned bulk transformations occurring at respective bottom and top faces. Given the differences between gaseous and surface diffusion rates, one would expect that surface diffusion would have more observable time dependence. The physical inspection of the top halves after heat treatment showed color changes from bright white to grey to black indicating reactions occurred at the pellets' periphery. With further XRD analysis, it was determined that any surface diffusion occurring is significantly less than the previously observed bulk diffusion in the top and bottom faces of the MP, GP, MPs, and GPs top halves.

#### *4.3.2.2.1. Discussion on mechanism of carbothermal reduction of zirconia*

During the carbothermal reduction heat treatment, the bottom face of the MP top half (YSZ) is exposed to more CO than GP because of its mixed  $\text{ZrO}_2$  and C bottom half. Based on previous research where CO is thought to be the reaction driver for ZrC conversion, the bottom face of the MP top half should produce more ZrC formation than GP. However, it was determined that GP bottom face exhibits significantly more ZrC conversion (74%) than MP (23%). The pellet systems studied have CO and C as the only likely species capable of carburizing YSZ to ZrC. The top halves of MP and GP densify to 80% ( $4.8 \text{ g/cm}^3$ ). During this treatment, enough porosity exists that both species can diffuse; therefore, it is difficult to discern the dominating species driving carbide formation. To study this effect, sintered versions of these samples, GPs and MPs, were exposed to the same heat treatments and carbonaceous exposures as their porous counterparts. In both sintered samples, the top and bottom faces still show  $\text{ZrO}_2$  to ZrC conversion, albeit less mole percent than the corresponding non-sintered pellets. These sintered YSZ top halves should, in principle, restrict or minimize any gaseous CO diffusion through them and only react through direct contact or gaseous species emanating from the lower halves. However, carbon because of its very small size can diffuse via grain boundaries, interstitial sites and lattice defect sites. Thus, reduction of YSZ to ZrC is still observed in the sintered GPs and MPs pellets.

Moreover, diffusion measurements show that kinetics of carbon diffusion in zirconia is rather slow. Thus, any YSZ to ZrC conversion occurring because of carbon will be highly localized. Experimental XRD results on Face A and B of the top halves confirms this since no ZrC was detected. In support of this, calculated X-ray depth penetration is less than  $20 \mu\text{m}$  on bottom faces of all the pellets. This effectively means that carbon diffusion in YSZ is so slow that it causes the diffusion front to extend to similar depths as that of the conversion front of  $\text{ZrO}_2$  to ZrC transformation.

In summary, experiments and calculations were performed to determine carbothermal reduction mechanisms and whether CO is the dominant species driving the  $\text{ZrO}_2$  to ZrC conversion. A series of experiments using pellet systems were conducted in which major and minor amounts of

CO and C were exposed to YSZ, and the reaction products were analyzed to confirm the reaction driver. If CO is the source of C for ZrC formation then the sample with the most available CO, MP, would exhibit the highest conversion; however, this was not observed. Instead, GP, which has a bottom half of graphite acts as a weak source of CO, shows maximum ZrC formation at the interface between top and bottom half due to solid-solid reaction of zirconia and graphite. In addition, top halves of MP and GP undergo sintering and reaction at the same time. This restricts CO diffusion through the bulk as the top pellets are sintered to ~77% of theoretical density of zirconia during heat treatment. To form ZrC, a carbonaceous species must transport into ZrO<sub>2</sub>, thus, C is a much more likely species to diffuse through a sintered sample than CO. In support of this mechanism, theoretical calculations indicate partial pressures of CO needed to drive zirconium carbide formation from zirconia are far beyond the environment in the reaction furnace. Since most of the processing is done under normal atmospheric pressure, so as to avoid capital investments and safety issues, formation of ZrC by reaction between ZrO<sub>2</sub> and CO appears less likely than carbon diffusion. In addition, carbon diffusion in zirconia is slow even at elevated temperatures. Thus any ZrC formation is highly localized as seen experimentally in all the top halves as well as theoretically based on diffusion depth calculations. These results indicate carbothermal reduction to be C driven as CO would be expected to be orders of magnitude faster than C and cause unlocalized diffusion (within the sample pores). Based on the above, carbothermal reduction of zirconia is more dependent on solid-solid reaction than gas-solid reaction, which is in disagreement with previous research findings that suggest carbothermal reduction of zirconia to be only a CO driven reaction mechanism.

More details can be found in reference [Sondhi et.al. (2013)].

#### *4.3.2.2.2 X-ray absorption spectroscopy (XAS) studies on the carbothermal reduction reaction products of 3 mol% yttria stabilized zirconia*

Extended x-ray absorption spectroscopy (EXAFS) at Zr K-edge has been used to determine changes in various bond lengths in 3 mol% yttria-stabilized zirconia (YSZ) during zirconium carbide (ZrC) formation. The principal objective of this study was to determine if ZrC formation at the YSZ/carbon interface alters the zirconia structure. A mixed phase sample (YSZ and graphite) was carbothermally reduced to form ZrC. X-ray diffraction phase quantification by Rietveld analysis confirmed the formation of ~50% ZrC in the analyzed sample volume. EXAFS of ZrC and YSZ powders, and a sintered YSZ pellet (~96.7% density) were used as standards to compare with the carbothermally-reduced sample. Ab initio calculations of these spectra quantified various Zr-O, Zr-C and Zr-Zr bond distances in the system. Best fit results revealed Zr-O<sub>1</sub> and Zr-Zr bond length values of 2.13 Å and 3.62 Å, respectively, in the YSZ powder and sintered pellet, and Zr-C and Zr-Zr bond lengths of 2.32 Å and 3.33 Å, respectively, in the ZrC powder. Similar fitting procedures were carried out on the carbothermally reduced pellet with measured Zr-O, Zr-Zr (of YSZ), Zr-C and Zr-Zr (of ZrC) bond lengths of 2.13 Å, 3.63 Å, 2.34 Å and 3.28 Å, respectively. These bond lengths indicate that the formation of ZrC in YSZ matrix does not influence the local structure when compared to pure standards. Therefore, carbothermal reduction does not induce any apparent strain or thermally-induced effects on the first and second coordination shell of Zr as measured by the x-ray absorption spectra of the carbothermally reduced sample. Interestingly, results indicated that sintering of the YSZ powder into pellets did not result in any significant change the Zr – O and Zr – Zr distances tetragonal YSZ.

EXAFS analysis was conducted on the Zr-K edge of 3 mol% YSZ powder, pure ZrC powder, sintered and carbothermally reduced YSZ pellets. The magnitude of FT patterns from both powders and the sintered YSZ pellet served as standards to compare bond lengths to the carbothermally reduced pellet. It was determined that all the fitted bond length values are in excellent agreement when comparing the pure standards to the carbothermally reduced sample. These results also imply that ZrC formed does not affect the cation-oxygen and cation-cation bond lengths of the parent YSZ phase and the remaining yttria from the carbothermal reduction of YSZ does not diffuse into the zirconia grains. In addition, the Zr-C bond length remains unchanged from its standard value suggesting there is no apparent strain or thermally-induced effects on the near fine structure resulting from the carbothermal reduction process. This “null effect” of carbothermal reduction implies that the formation of ZrC within a YSZ/CCC composite will not likely deleteriously effect the viability of a YSZ thermal protective layer on carbon structures. In addition, the bond distance values in YSZ were found to be insignificantly different between powder and sintered samples. Thus, sintering did not affect the inter-atomic bond distances in the system. This is often assumed based on XRD data, but this result confirms that bond distances in powder structure do not change appreciably during densification. More details can be found in reference [Sondhi et.al. (2014)].

#### **4.3.3. Task C: Metal-Carbon Nanotube Hybrids**

##### *4.3.3.1. Nickel-Carbon Nanotube (CNT) hybrid materials:*

Two types of carbon nanotube reinforced nickel (CNT/Ni) nanocomposites were processed, both involving spark plasma sintering (SPS) of precursor powders consisting of nickel and carbon nanotubes. The first type involved simple mechanical dry milling (DM) of nickel and CNT powders, followed by sintering using SPS, resulting in nanocomposites exhibiting a tensile yield strength of 350 MPa (about two times that of SPS processed monolithic nickel with a strength of 160 MPa) and about 30% elongation to failure. In contrast, the nanocomposites processed by spark plasma sintering of powders prepared by molecular-level mixing (MLM) exhibited substantially higher tensile yield strength of 690 MPa but limited ductility with a 8% elongation to failure. While the former type of processing involving dry-milling is expected to be lower in cost as well as easy to scale-up, the latter processing technique involving molecular-level mixing leads to a more homogeneous distribution of nanotubes leading to extraordinarily high strength levels.

###### *4.3.3.1.1. Microstructure of CNT/Ni composites:*

SEM images of the SPS processed pure nickel and CNT/Ni nanocomposites (DM and MLM) are collected in back-scattered mode. Pure nickel exhibits a uniform grain structure without any porosity with an average grain size about 45  $\mu\text{m}$ . The full and rapid densification of powder compacts without any substantial grain growth is one of the major advantages of SPS processing that is a result of sintering by joule heating and the spark plasma generated by the pulsed high electric current passing through the compact. CNT/Ni (DM) nanocomposite shows a substantially refined grain structure as compared with the pure Ni, even though both samples

were prepared with the same initial size of Ni powder. Within the Ni matrix, there appears to be a uniformly distributed second phase or possibly porosity. However, a higher magnification SEM image confirms that the regions exhibiting a darker contrast are actually CNT bundles of 1-2  $\mu\text{m}$  in size, rather than porosity. Therefore, based on the comparison of microstructures of the SPS processed pure Ni and CNT/Ni composite (DM), it is apparent that addition of CNTs into the nickel matrix helps in grain refinement by possibly inhibiting grain growth and providing nucleation site for new grains during recrystallization. SEM images from the CNT/Ni (MLM) nanocomposites, that also exhibits a uniform grain structure. Previous investigations of such CNT/Ni nanocomposites processed via molecular level mixing and SPS have clearly shown that there is a uniform distribution of individual CNTs within the nickel matrix [Hwang et.al. (2013)].

#### *4.3.3.1.2. X-ray diffraction analysis:*

The XRD pattern for pure nickel shows peaks corresponding to the (111), (200), and (220) crystallographic planes of nickel. Both the dry-milled as well as molecular level mixed CNT/Ni nanocomposites show an additional (0002) carbon peak. Presence of carbon peak in both the CNT/Ni nanocomposites confirms the presence of carbon nanotubes. In all three cases, the maximum intensity peak is the Ni(111) peak. The Ni(111)/Ni(200) intensity ratio for SPS processed pure Ni is 2.17, while that for dry-milled and SPS processed is 2.45, and finally for molecular level mixed and SPS processed is 2.25. Comparing these three values with the standard ratio expected for randomly oriented Ni grains in the International Center for Diffraction Data (ICDD) files obtained from Joint Committee of Powder Diffraction Standards (JCPDS) of 2.38, it is apparent that there is no significant change in texture resulting from the introduction of CNT's in the nickel matrix. This is in contrast to previous publications on electro-deposited CNT/Ni nanocomposites where a clear increase in the Ni(200) peak intensity has been reported, indicating a change in texture due to the addition of CNTs [Borkar et.al. (2011)].

#### *4.3.3.1.3. Micro Raman spectroscopy studies:*

Raman spectroscopy was conducted to determine if any structural changes in the CNT occurred due to mechanical ball milling as well as during SPS due to heat, pressure and current. Figure 18 shows Raman spectra for raw CNT, CNT/Ni ball milled powder, and SPS CNT/Ni (MLM) and CNT/Ni (DM) nanocomposites. The raw CNT serves as a reference with primary peaks at  $\sim$ 1340,  $\sim$ 1572 and small shoulder peak at  $\sim$ 1611  $\text{cm}^{-1}$  wavenumbers, corresponding to the D, G and D' peaks of the CNT, respectively [Behler et.al. (2006) and Hwang et.al. (2008)]. The D peak origin is due to the breathing modes of  $\text{sp}^2$  bonded atoms in rings, the G peak is attributed to the in-plane bond stretching of all pairs of  $\text{sp}^2$  bonded atoms in both rings and chains, and the D' peak is double-resonance Raman band induced by defects [Behler et.al. (2006), Hwang et.al. (2008) and Ferrari et.al. (2007) ]. The disorder in CNT, in a qualitative sense, can be monitored via the D and D' peaks, their intensities, and the intensity ratio of the D to G peak ( $I_D/I_G$ ). These parameters are considered defect dependent, e.g. bond length and angle (curvature) disorder at the atomic scale. In comparing the raw CNT to the CNT/Ni ball milled powder in Fig. 3, the D and G peak positions and  $I_D/I_G$  ratio do not change suggesting structural integrity of the CNT is preserved after mechanical ball milling, i.e., no increase in CNT structural disorder. In contrast,

Raman spectra for SPS nanocomposites exhibit some minor peaks changes: 1) D peak increases from 1340 to 1357 (CNT/Ni DM) and 1348 (CNT/Ni MLM)  $\text{cm}^{-1}$ , 2) G peak increases from 1572 to 1582 (CNT/Ni DM) and 1591 (CNT/Ni MLM)  $\text{cm}^{-1}$ , and 3)  $I_D/I_G$  ratio increases from 1.2 to 1.9 (CNT/Ni DM) and 1.7 (CNT/Ni MLM).  $I_D/I_G$  ratios  $> 2$  indicate a highly disordered form of carbon [Tunistara et.al. (1970)]. While these trends in the Raman peak shifts and intensity ratios may imply a slight increase in structural disorder due to SPS, they are more indicative of residual compressive stress occurring during SPS, which has been observed for other SPS CNT composites. The Ni grains will effectively compress the CNT under the SPS pressure causing the D and G peaks to shift slightly to higher wavenumbers. Therefore, the structural stability of the CNT is relatively well maintained and the TEM studies presented below corroborate this.

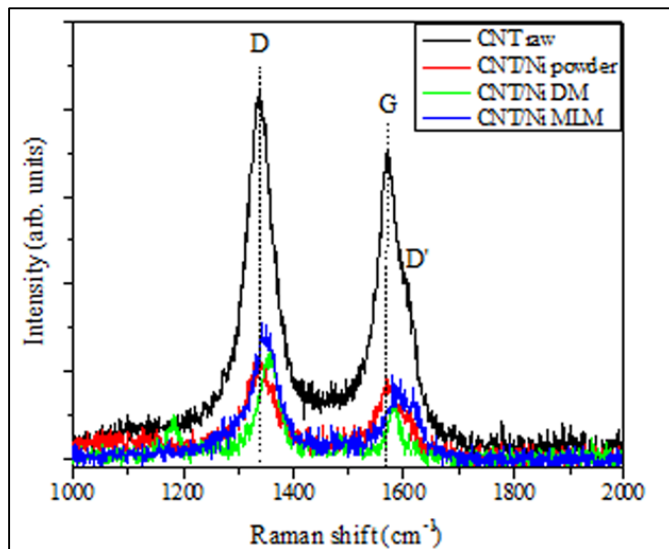


**Figure 18:** Raman spectra showing the D, G, and D' peaks from raw CNT, CNT/Ni ball milled powder, CNT/Ni Dry milled, and CNT/Ni molecular level mixed nanocomposites

#### 4.3.3.1.4. Microhardness and Tensile behavior of CNT/Ni composites

The Vickers microhardness of the CNT/Ni nanocomposites are shown in Table 6. There is a considerable enhancement in the microhardness with the addition of CNTs to the nickel matrix. The hardness of CNT/Ni (MLM) nanocomposites is 98.6 HV, and that of the CNT/Ni (DM) nanocomposite is 94.5 HV, both of these values are about 1.5 times higher than that of pure SPS processed nickel. The yield strength and elongation (tensile) properties of SPS processed pure nickel and both types of CNT/Ni nanocomposites are also listed in Table 6. The tensile yield strength of CNT/Ni (DM) nanocomposite is 350 MPa, which is about 2 times higher than that of pure nickel (160 MPa). Even more striking is that the tensile yield strength of the CNT/Ni (MLM) nanocomposite is 690 MPa, about 4 times that of pure Ni and 2 times that of CNT/Ni (DM) nanocomposite. However, comparing the ductility of all three types of nanocomposites, while pure Ni exhibits about 50% elongation to failure, the elongation values for the CNT/Ni

(DM) and CNT/Ni (MLM) are 30% and 8% respectively. Comparing the stress-strain behavior, it appears that while the CNT/Ni (DM) nanocomposite exhibits a modulus similar to that of SPS processed pure Ni, the CNT/Ni (MLM) nanocomposite exhibits a substantial higher modulus. Since the details of the deformation behavior of the CNT/Ni MLM nanocomposite have been discussed in a recent paper [Cha et.al. (2005)], these are not being repeated in the present paper. However, it is important to note the contrasting aspects of deformation between the two types of CNT/Ni nanocomposites being compared in the present study. While the CNT/Ni (DM) nanocomposite exhibits a classical strain-hardening behavior all the way from yield to failure, similar to pure Ni, the CNT/Ni (MLM) nanocomposite exhibits the sharper yield point accompanied by a drop in stress and subsequently strain-hardening to a limited degree before failure. Examination via secondary electron indicated that CNT/Ni (DM) nanocomposite exhibits ductile failure. This is indicative of a very ductile deformation behavior in agreement with the greater than 30% elongation observed for this nanocomposite. From an EDS carbon map, corresponding to the fracture surface, the location of the CNT bundles on the fracture surface can be determined. Contrastingly, the CNT/Ni (MLM) nanocomposite fracture surface exhibits much smaller dimples of the order of sub-micron to at most a micron. Additionally there is indicative of some strain localization and eventual failure at a lower level of strain. This is in agreement with the observed lower ductility of the CNT/Ni (MLM) nanocomposite as compared to the CNT/Ni (DM) nanocomposite. However, from the perspective of strength, the CNT/Ni (MLM) exhibits a yield strength that is almost twice that of the CNT/Ni (DM) nanocomposite. The enormous strengthening in case of CNT/Ni (MLM) nanocomposites arises mainly due to the homogeneous distribution of individual CNTs within the nickel matrix [Cha et.al. (2005)]. The strong interfacial bonding between the CNTs and the Ni matrix is effective to improve mechanical properties of CNT/metal nanocomposites. Despite the fact that the CNTs are in the form of sub-micron bundles in case of the CNT/Ni (DM) nanocomposite, a significant improvement in yield strength is observed and can be attributed in part due to grain size refinement. The experimental observations indicate that the uniform dispersion of CNT bundles is helping in grain refinement as well as possibly in load transfer between the metal matrix and the nanotube bundles.

Table 6 Summary of observed mechanical properties

Sample	Hardness (HV)	Yield Strength (MPa)	Ductility /Elongation (%)
Pure Nickel	77.52±3	160±5	50
CNT/Ni (DM)	94.5±6	350±4	30
CNT/Ni (MLM)	98.6±4	690±10	8

Therefore, comparing and contrasting the mechanical properties of these nanocomposites, it is evident that while the CNT/Ni (MLM) composite exhibits the highest tensile yield strength, the CNT/Ni (DM) composite exhibits a higher tensile ductility. The role of any residual stresses resulting from the SPS process should also be considered, especially since the graphite plungers being in contact with the sintered material during the cooling step can result in considerably high

cooling rates experienced by the sintered material. Such cooling during SPS ensures that heat does not unnecessarily stay retained in the sintered sample. However, when the sintering temperature is significantly low (800 °C) compared to the melting point of Ni (1455 °C), or  $T_{\text{sintering}} = 0.62 T_{\text{melting}}$ , the considerably high cooling rate is still unlikely to cause any significant residual stresses in the sintered composite.

Additionally, it is worthwhile to compare the deformation behavior of CNT/Ni MLM processed nanocomposites with ultra-fine grained (UFG) nickel samples. Very high tensile yield strengths about 990 MPa, have been reported in the literature for UFG nickel samples, processed via equal channel angular pressing (ECAP) plus cold-rolling [Krasilnikov et.al. (2005)]. These samples had grain sizes about 0.33  $\mu\text{m}$  and exhibited an elongation to failure about 7%. SEM images of the fracture surface of these UFG nickel samples appear to exhibit a typical ductile failure with relatively large dimple sizes (larger than the grain size) [Krasilnikov et.al. (2005)]. Comparing the reported images of the fracture surface in case of UFG nickel with the fracture surface for the CNT/Ni MLM nanocomposite in the present study, the dimple sizes appear to quite similar and in both cases exhibit extended edges. However, the grain size in case of the CNT/Ni MLM nanocomposite is substantially larger about 15-25  $\mu\text{m}$ , almost two orders of magnitude larger than that of the UFG nickel sample. Consequently, it can be concluded that the homogeneous distribution of CNT's in case of the MLM nanocomposite is primarily responsible for its very high yield strength (about 690 MPa).

#### *4.3.3.1.5. Summary and Conclusions:*

- Two types of CNT/Ni nanocomposites have been prepared using the spark plasma sintering (SPS) process, one using ball milled nickel and CNT precursors, referred to as CNT/Ni (DM) and the second one using molecular level mixed CNT/Ni composite powders as a precursor, referred to as CNT/Ni (MLM).
- While both types of nanocomposites exhibited a substantial enhancement in microhardness and tensile yield strength as compared to SPS processed pure Ni, the CNT/Ni (DM) nanocomposite exhibited much higher ductility while the CNT/Ni (MLM) nanocomposite exhibited much higher tensile yield strength.
- The improvement in mechanical properties of the CNT/Ni (DM) nanocomposite results from a combination of composite strengthening due to the nanotubes, coupled with grain refinement of the nickel matrix, both effects resulting from the homogeneous distribution of small bundles of CNTs.
- The microhardness and yield strength of CNT/Ni (MLM) nanocomposite was significantly higher as compared to both CNT/Ni (ball milled) as well as pure nickel.
- The high strength of CNT/Ni (MLM) nanocomposite is mainly achieved due to the homogeneous distribution of individual CNTs in the nickel matrix and high interfacial strength due to a well-bonded Ni/CNT interface, permitting excellent load transfer between the matrix and the nanotubes.

#### *4.3.3.2. Nickel-Graphite Nanoplatelet Hybrid Materials:*

While multiple recent reports have demonstrated enormous enhancements in yield strength in metal matrix nanocomposites reinforced with carbon nanotubes and graphite nanoplatelets (GNP),

such composites typically exhibit drastic reductions in tensile ductility. Mechanical mixing of nickel (Ni) powders and GNP powders, followed by spark plasma sintering (SPS), has been used to develop a new class of GNP/Ni nanocomposites that exhibit huge enhancements in tensile yield strength while preserving good ductility. Thus, a Ni-1GNP (1 vol.% GNP) nanocomposite exhibited a tensile yield strength of 370 MPa (about 2.5 times of SPS processed monolithic nickel ~ 160 MPa) and an elongation to failure ~ 40%. Interestingly, while a higher volume fraction of GNPs, such as Ni-2.5GNP (2.5 vol.% GNP) exhibited an enhancement in tensile yield strength due to grain refinement, there was a significant reduction in ductility ~ 10%, primarily due to agglomeration of GNPs. The enhancement in the tensile strength and ductility of the Ni-1GNP nanocomposite can be attributed to combined effect of homogeneous dispersion of GNPs and grain refinement, the relative influence of each of these effects has been quantitatively assessed in this paper. Additionally, the strong metal-GNP interfacial bonding helps effectively transfer load across the GNP/metal interface during tensile deformation.

#### *4.3.3.2.1. Scanning Electron Microscopy (SEM) Analysis of GNP/Ni nanocomposites*

Back-scattered SEM images of the SPS sintered pure nickel and GNP/Ni nanocomposites are obtained. Pure nickel exhibits a uniform grain structure without much porosity with an average grain size ~ 25  $\mu\text{m}$ . The full and rapid densification of powder compacts without any substantial grain growth is one of the major advantages of SPS processing that is a result of sintering by joule heating and the spark plasma generated by the pulsed high electric current passing through the compact. Ni-1GNP nanocomposite shows a substantially refined grain structure, as compared with the pure Ni, even though both samples were prepared with the same initial size of Ni powder. GNPs appear to be quite uniformly distributed along the grain boundaries within the nickel matrix. The initial ball milling followed by spark plasma sintering helps to obtain a refined grain structure due to homogeneous distribution of GNPs within the nickel matrix. The addition of GNPs into the nickel matrix assists in grain refinement by possibly inhibiting grain growth and providing nucleation sites for new grains during recrystallization. Similar results were observed in Ni/CNT (DM) nanocomposites sintered using SPS [Tunistara et.al. (1970)]. SEM images of the Ni-2.5GNP and Ni-5GNP nanocomposites show that also exhibit a refined grain structure, but additionally, coarse clusters of GNPs are observed within the nickel matrix. It is evident that as the volume fraction of GNPs increases in these nanocomposites, there is a marginal refinement of the matrix nickel grains but this is accompanied by substantial clustering of the GNPs into coarser bundles within the matrix. Also, cross-sectional view of these composites didn't show any change in the shape of these GNP clusters.

From pseudo-colored OIM<sup>TM</sup> map and texture maps of Ni-1GNP nanocomposite both pure nickel and Ni-1GNP nanocomposites exhibit random texture of the matrix nickel grains. This is the main advantage of SPS sintered alloys and metal-matrix composites wherein a refined grain structure can be retained without any substantial texturing effect. Also, it should be noted that there is no significant change in texture resulting from the addition of GNPs in the nickel matrix.

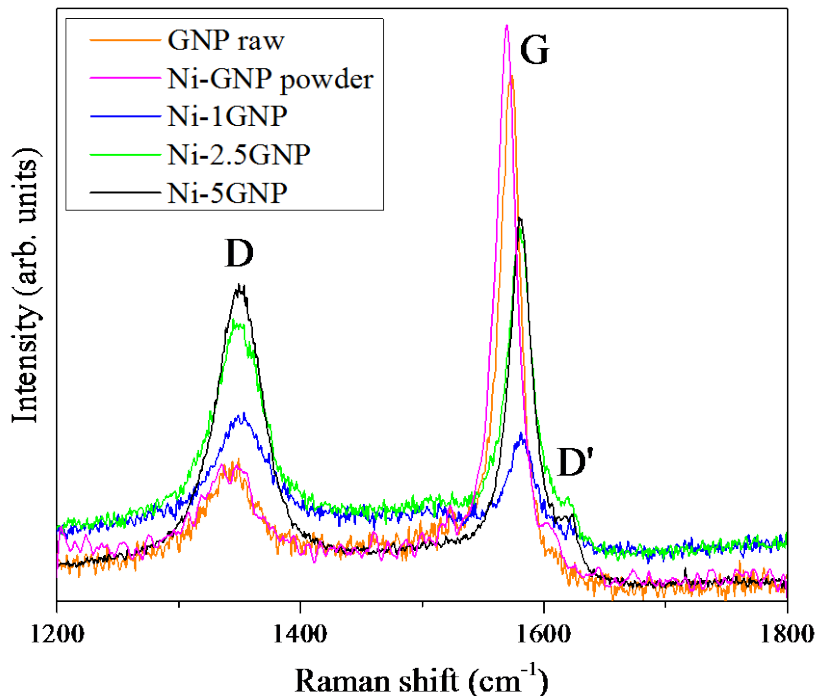


**Figure 19:** Micro-Raman spectra showing the D, G and D' peaks from raw GNP, ball milled Ni-GNP powder, and different content Ni-GNP nanocomposites.

#### 4.3.3.2.2. X-ray Diffraction (XRD) Analysis of GNP/Ni nanocomposites

The XRD pattern for pure nickel shows peaks corresponding to the (111), (200), and (220) crystallographic planes of nickel. The addition of GNPs leads to the presence of a new peak which is referred to (0002) carbon peak corresponding to  $2\theta=26.5^\circ$ . Presence of carbon peak in both the GNP/Ni nanocomposites confirms the presence of GNPs, without any other interfacial product/ carbide formation. With increasing volume fraction of GNPs, the intensity of the GNP peak/ (0002) carbon peak, systematically increases. In all three XRD patterns from the GNP/Ni nanocomposites, the maximum intensity peak corresponds to the Ni(111) peak. The Ni(111)/Ni(002) intensity ratio for SPS processed pure Ni is 2.35; while that for Ni-1GNP, 2.43; for Ni-2.5GNP, 2.21; and finally for Ni-5GNP, 2.25. These three ratio values are in good agreement with the standard ratio expected for randomly oriented Ni grains of 2.38 (based on the International Center for Diffraction Data (ICDD) files obtained from Joint Committee of Powder Diffraction Standards (JCPDS)). No significant change in texture results from the introduction of GNPs in the nickel matrix. Therefore, these XRD results substantiate the EBSD results indicating a random texture in these nanocomposites.

#### 4.3.3.2.3. Micro-Raman Spectroscopy Analysis of GNP/Ni nanocomposites

Micro-Raman spectroscopy was carried out to determine if any structural changes in the GNP occurred due to mechanical ball milling as well as during SPS due to heat, pressure and current. Fig. 19 shows Raman spectra for raw GNP, ball milled Ni-GNP powder before SPS, and different content Ni-GNP SPS nanocomposites. The Raman spectra showed carbon D, G, and D'

peaks with no additional peaks associated with interfacial metal carbide formation due to sintering, in corroboration with the XRD results. These C-C parameters often show changes in their peak location and intensity depending on the carbon structure. Most notable the substantially higher G peak intensities compared to the D peak for the raw GNP and ball milled Ni-GNP powders. Also, the intensity of the D' peak is very small and is seen as a shoulder to the primary G peak. The disorder of the samples, in a qualitative sense, can be monitored via the D and D' peaks and their intensities [Kim et.al. (2008)]. In comparing the raw GNP to the ball milled Ni-GNP powder, the D and G peak positions and  $I_D/I_G$  ratio do not significantly change suggesting structural integrity of the GNP is preserved after mechanical ball milling, i.e., no increase in GNP structural disorder. In contrast, the main features and trends in going from the starting GNP and ball milled powders to SPS nanocomposites are (a) G peak increases from 1569 to 1581  $\text{cm}^{-1}$ , (b) D' peak becomes more pronounced at 1620  $\text{cm}^{-1}$ , and (c)  $I_D/I_G$  increases. The Ni-1GNP nanocomposite exhibits the highest  $I_D/I_G$  ratio of 1.11 where ratios  $> 2$  indicate a highly disordered form of carbon [Inam et.al. (2010)]. Therefore, there is a slight change in C-C defect density (increasing  $I_D/I_G$  ratio) and degree of graphitization (increases with higher G peak shift) from starting powders to sintered nanocomposites. While these trends in the Raman peak shifts and intensity ratios may imply a slight increase in structural disorder due to SPS, they can also be attributed to a certain amount of residual compressive stresses resulting from the SPS process, which has been previously reported for other SPS carbon-based composites. The Ni grains will effectively compress the GNP under the SPS pressure causing the D and G peaks to shift slightly to higher wavenumbers. In the case of the Ni-1GNP nanocomposite, the highest Raman spectra  $I_D/I_G$  ratio of 1.11 implies that more GNP compression occurred during sintering, since the GNPs are more uniformly distributed compared to the higher content and more agglomerated GNP nanocomposites. Therefore, the GNP structure is relatively well maintained and the TEM studies presented below corroborate this structural stability.

#### *4.3.3.2.4. Tensile Properties of GNP/Ni nanocomposites*

The yield strength and elongation (tensile) properties of SPS processed pure nickel, processed under identical conditions as those used for the nanocomposites, and GNP/Ni nanocomposites are listed in Table 7.. The tensile yield strength of Ni-1GNP nanocomposite is 370 MPa, which is about 2.3 times higher than that of pure nickel (160 MPa), processed under the same SPS conditions. Also, Ni-1GNP nanocomposite exhibits about 40% elongation to failure/ductility, which is well comparable with that of pure nickel (i.e., 50% elongation to failure). With increasing volume fraction of GNPs for Ni-2.5GNP nanocomposite exhibits tensile yield strength of 390 MPa, which is about 2.4 times higher than that of pure nickel with a compromise in ductility / elongation to failure (i.e. about 10%). Therefore, while increasing the volume fraction of GNPs from 1 to 2.5-vol% is accompanied with a marginal increment in tensile yield strength, there is a significant reduction in ductility (i.e., from 40% to 10%). This reduction in ductility can be attributed to the agglomeration of GNPs into coarse bundles within the nickel matrix. These bundles fail to effectively transfer load/stress during tensile deformation. Even more striking is that, the tensile yield strength of the Ni-5GNP nanocomposite is 350 MPa, lower than that of both the Ni-1GNP and Ni-2.5GNP nanocomposites, due to more pronounced GNP clustering and coarser bundles within the nickel matrix. There are multiple previous reports

discussing similar observations with respect to the deterioration in mechanical properties of CNT/metal composites due to the agglomeration of CNTs into bundles, that fail to effectively transfer load/stress during tensile deformation.

**Table 7:** Microhardness, yield strength and elongation properties of pure nickel and GNP/Ni nanocomposites.

Sample	Hardness (HV)	Yield Strength (MPa)	Ductility/Elongation (%)
Ni (processed under the same conditions)	77.52±5	160±5	50
Ni-1GNP	165±10	370±3	43
Ni-2.5GNP	170±4	390±3.5	10
Ni-5GNP	150±3	350±6	10

Enhancement in the yield strength ( $\Delta\sigma_y$ ) of the SPS processed GNP/Ni composites as compared with that of the pure Ni sample, processed under identical conditions were noticed. However, it should be noted that the grain size of the nickel matrix was not the same in all these cases. A plot of the grain size of the nickel matrix as a function of the volume% of GNP in these composites, clearly exhibiting a trend of progressively decreasing grain size with increasing volume% of GNP. The grain size for the three GNP/Ni nanocomposites being investigated, the predicted yield strength for these grain sizes based on a Hall-Petch type relationship , and the experimentally measured yield strength of all these nanocomposites. The values of the Hall-Petch coefficient,  $\sigma_0$  and  $k$ , were obtained from a previously reported optimization study for pure nickel, SPS processed under different conditions. Varying the SPS processing parameters permitted a systematic variation in the grain size of the pure nickel samples from 5 to 45  $\mu$ m. The corresponding tensile properties of these pure nickel samples were measured and their yield strength values were plotted against  $d^{-1/2}$  (inverse square root of grain size) to determine the  $\sigma_0$  and  $k$  values in the classical Hall-Petch relationship,

$$\sigma_y = \sigma_0 + kd^{-1/2} \quad (23)$$

Thus, values of  $\sigma_0 = 77.7$  MPa and  $k = 434.5$  MPa. $\mu\text{m}^{1/2}$  were determined from this optimization study on SPS processed pure nickel. This relationship was used to predict the effective contribution of grain refinement in the nickel matrix to the yield strength of the GNP/Ni nanocomposites. Based on both the yield strengths of the Ni-1GNP and Ni-2.5GNP nanocomposites it is apparent that while the grain refinement in the nickel matrix contributes to the strength enhancement, this cannot be the sole factor for the high yield strength of these nanocomposites. Thus, in both cases there is at least an additional 60-70 MPa enhancement in the yield strength beyond the value predicted by the Hall-Petch relationship, which can be attributed to the GNP reinforcement. Therefore, the Ni-1GNP and Ni-2.5GNP nanocomposites exhibited a significant improvement in tensile yield strength due to the coupled effect of grain refinement as well as GNP reinforcement in the nickel matrix. Furthermore, the strengthening effect of the GNPs indicates that this reinforcement effectively transfers stress during tensile deformation. Typically, the effective yield strength of composites due to the presence of the reinforcement has often been modeled using a shear-lag model based on the load transfer theory as follows:

$$\sigma_c = \sigma_m (1 + S_{\text{eff}} V_f) \quad (24)$$

where  $\sigma_c$  is the effective yield strength of the composite,  $\sigma_m$  is the yield strength of the matrix without the reinforcement,  $S_{\text{eff}}$  is the effective aspect ratio of the reinforcement, and  $V_f$  is the volume fraction of the reinforcement. This model was originally developed for composites reinforced with randomly oriented short fibers assuming perfect bonding between the reinforcement and the matrix and predicts a linear increase in the effective yield strength of the composite with increasing volume fraction of the reinforcement. While in the present study, the experimentally measured yield strength for the Ni-2.5GNP exceeds that of the Ni-1GNP nanocomposite, this increase is a combined effect of grain refinement and reinforcement from the GNPs. Also, the grain size plotted as a function of volume % of GNPs clearly shows grain refinement due to the addition of GNPs in these composites. Therefore, in order to de-couple the effect of strengthening due to grain refinement from strengthening due to composite reinforcement from GNPs, the  $\Delta\sigma_y(\text{GNP}) = \sigma_y(\text{expt}) - \sigma_y(\text{matrix})$  has been plotted as a function of volume % of GNPs, in Fig. 6(d). Here the  $\sigma_y(\text{matrix})$  corresponds to the yield strength of SPS processed pure Ni with a similar grain size as that observed in the corresponding GNP/Ni nanocomposite. This plot appears to depict a functional relationship where the  $\Delta\sigma_y(\text{GNP})$  initially increases with increasing volume % of the GNPs, but after achieving a maximum value between 1 to 2 volume % GNPs, the  $\Delta\sigma_y(\text{GNP})$  decreases with further increase in the GNP content. This decrease in yield strength for higher volume % of GNPs can be largely attributed to the agglomeration of the GNPs into bundles within the nickel matrix as observed in case of the Ni-5GNP nanocomposite. Despite the more refined nickel grain size in this nanocomposite (~2  $\mu\text{m}$ ) its yield strength is only 350 MPa, lower than that of both Ni-1GNP and Ni-2.5GNP.

Comparing the ductility of the three GNP/Ni nanocomposites, it should be noted that the Ni-1GNP nanocomposite exhibits the largest elongation to failure ductility, ~40%, while the Ni-2.5GNP and Ni-5GNP exhibit elongations of only ~10%. Interestingly, the stress-strain behavior of the Ni-1GNP nanocomposite largely resembles that of pure Ni, with significant strain hardening reaching an ultimate tensile strength (UTS) of ~570MPa. While both the Ni-2.5GNP and Ni-5GNP nanocomposites exhibit the early stages of strain hardening, they abruptly fail

before achieving their ultimate tensile strengths. Such a well-behaved stress-strain curve, observed in case of the Ni-1GNP nanocomposite, coupled with its high yield and tensile strengths as well as excellent ductility, makes it a very promising material for engineering applications.

#### *4.3.3.2.5. Fractography Analysis of GNP/Ni nanocomposites*

From SEM images (secondary electron images) of the fracture surfaces of the pure nickel, Ni-1GNP, Ni-2.5GNP, and Ni-5GNP nanocomposites it is evident that while pure nickel and the Ni-1GNP nanocomposite exhibit similar fracture surfaces, the Ni-2.5GNP and Ni-5GNP nanocomposites exhibit somewhat different fracture surfaces. The Ni-1GNP nanocomposite fracture surface exhibits the typical cup and cone type failure features, with dimples of the order of few microns in size. This is indicative of a very ductile deformation behavior in agreement with the greater than 40% elongation observed for these nanocomposites, similar to that of pure nickel. Contrastingly, the fracture surfaces of the Ni-2.5GNP and Ni-5GNP nanocomposites exhibit much smaller dimples as well as GNP clusters. This is indicative of strain localization and eventual failure at a much lower level of strain. The significant enhancement of yield strength coupled with reasonable ductility, obtained in case of the Ni-1GNP nanocomposite, can be attributed to a coupled effect of grain refinement, homogeneous distribution of GNPs in the nickel matrix, and strong Ni-GNP interfacial bonding, leading to effective transfer of load across the metal/GNP interface during tensile deformation.

#### *4.3.3.2.6. Transmission Electron Microscopy (TEM) Analysis of GNP/Ni nanocomposites*

From TEM results from the Ni-1GNP nanocomposite, it can be seen that while the GNPs in this nanocomposite are homogeneously distributed, most of them are located at the boundaries or triple junctions of nickel grains. An enlarged bright-field view of a single GNP embedded in the nickel matrix at a triple junction. High-resolution TEM micrographs of the GNP/Ni interface in case of the Ni-1GNP nanocomposite show that the interface is relatively sharp, exhibits excellent bonding between the GNP and nickel grain, and is also contaminant-free. Furthermore, these high-resolution TEM images do not exhibit any interfacial reaction layer between the GNP and the Ni matrix in corroboration with XRD and Raman spectroscopy. Such a well-bonded GNP/Ni interface is expected to effectively transfer load between the matrix and the reinforcement, leading to a higher strength and ductility. TEM results from the Ni-2.5GNP nanocomposite show that both larger grains (order of microns) as well as nanocrystals of nickel, with an average diameter of 50 nm, that were surrounded by GNPs, 50 nm wide and 300 nm long. High-resolution TEM images of this microstructure clearly reveal the individual graphene sheets within platelets and their interface with the surrounding nickel grains. Additionally, a higher magnification view of a single GNP/Ni interface revealed the well bonded and sharp nature of this interface. The lattice planes of nickel as well as graphene on either sides of the interface are clearly visible in this image and confirm the absence of any interfacial reaction product.

#### 4.3.3.2.7. Summary and Conclusions

A new class of nanocomposites, exhibiting an excellent combination of strength and ductility, has been prepared by spark plasma sintering (SPS) of a mechanically mixed (ball-milled) mixture of elemental nickel powder with graphite nanoplatelets (GNP). The volume fraction of the GNP reinforcement has been varied from 1 to 5 vol% in these nanocomposites. All the GNP/Ni nanocomposites exhibited substantial enhancement in microhardness and tensile yield strength as compared to SPS processed pure nickel, under similar processing conditions. The Ni-1GNP nanocomposite exhibited the best combination of high yield strength (~350 MPa) and high ductility (~40% elongation to failure), while the Ni-2.5GNP nanocomposite exhibited marginally higher yield strength (~370 MPa) but substantially lower ductility (~10% elongation to failure). The yield strength enhancement in the GNP/Ni nanocomposites can be attributed to a synergistic effect of matrix grain coupled with the reinforcement effect resulting from a homogeneous distribution of GNPs with a strong interfacial bonding with the nickel matrix, which effectively transfers load across metal/GNP interface. While 1 vol% GNP appears to be an optimal level of reinforcement in the nickel matrix, higher levels of 2.5 or 5 vol% result in substantial agglomeration of the GNP's within the matrix leading to deterioration in mechanical properties primarily manifested by reduction in ductility. Furthermore, the substantial agglomeration of GNPs in case of the Ni-5GNP composite, results in less effective transfer of load from the metal matrix to the GNPs, leading to reduction in yield strength as compared to the Ni-1GNP and the Ni-2.5GNP nanocomposites. The yield strength of these nanocomposites has been modeled using a combined model incorporating the effects of composite reinforcement strengthening via load transfer with Hall-Petch type strengthening from grain refinement.

## 5. Conclusion

The tasks carried out under the three thrust areas of ISES, have led to a number of conclusions. Considering the diversity of the thrust areas and the tasks under these thrusts, these conclusions have been divided under the different thrust areas as follows:

### Thrust Area I: Lifetime prediction of turbine blades

#### Task A: Creep debit effect in Ni-base superalloy single-crystals

- a. A mechanistic model for the observed thickness debit effect in the creep response of Ni-based single crystal super alloys was proposed based on the experimental observations and detailed finite element calculations.
- b. The bulk damage mechanisms accounted for were the nucleation of cleavage-like cracks from preexisting voids and, at the higher temperature, void nucleation. The surface damage mechanisms modeled at the higher temperature were an oxidation layer, a  $\gamma'$ -precipitate free layer and a  $\gamma'$ -precipitate reduced layer.
- c. Model results for the creep response and for the thickness debit effect were in close quantitative agreement with the experimental results. In addition, the model predicted qualitative features of the failure process that were in good agreement with experimental observations. The simplicity of the model also allowed parametric studies to explore the relative roles of bulk and surface damage as well as the relative roles of cleavage-like cracking and void nucleation in the bulk.

### Thrust Area II: Influences of Microstructure and Chemistry on Mechanical Properties of Aerospace Materials

#### Task A: Structure and chemistry across $\gamma$ / $\gamma'$ interfaces in nickel-based superalloys

- a. Aberration-corrected high resolution scanning transmission electron microscopy (HRSTEM) coupled with three-dimensional atom probe (3DAP) tomography revealed the presence of two interfacial widths, one corresponding to an order-disorder transition, and the other to the compositional transition across the interface, raising fundamental questions regarding the definition of the interfacial width in such systems.
- b. Partially ordered  $\gamma$  /  $\gamma'$  interfaces could potentially act as a diffusion barrier for the coarsening of  $\gamma'$  precipitates resulting in trans-interface diffusion controlled (TIDC) coarsening.

#### Task B: Three-dimensional characterization of nanoscale $\gamma'$ precipitates in nickel-based superalloys

- a. The coupling of three characterization techniques spanning across multiple length scales, scanning electron microscopy (SEM), energy-filtered transmission electron microscopy (EFTEM), and 3D atom probe tomography (3DAP) techniques, has permitted characterizing and quantifying the multimodal size distribution of different generations of  $\gamma'$  precipitates formed during continuous cooling, followed by aging, in a commercial nickel-based superalloy, Rene 88 DT.
- b. The size distributions of first, second, and third generation of  $\gamma'$  precipitates, in the same heat-treated condition, have been plotted as a function of equivalent diameter. The presence of tails in the precipitate size distribution suggests that the nucleation events occur over a range of temperatures within each nucleation burst, corresponding to each generation of  $\gamma'$  precipitates.

The same techniques were applied to other nickel base alloys, including model Ni-Al-Cr and Ni-Al-Cr-Co alloys.

**Task C: Lattice parameters of  $\gamma$  and  $\gamma'$  phases and site occupancies in ordered  $\gamma'$  phase**

- a. Coupling atom probe tomography (APT) with synchrotron-based x-ray diffraction, a methodology for determining the preferred site occupancy of various alloying elements within ordered  $\gamma'$  precipitates was developed and applied to the Rene88 alloy as well as model Ni-Al-Cr and Ni-Al-Cr-Co alloys.
- b. The results indicate that Nb prefers to reside on the Al sublattice site in the  $\gamma'$  phase. Additionally, the results indicate that Cr prefers the Ni sublattice sites, while Co is likely to occupy both the Al and Ni sublattice sites. These experimental results were also coupled with first-principle computations based on the density functional theory (DFT).

**Task D: Mechanisms of refined scale intra-granular precipitation in titanium alloys**

- a. A novel non-classical intra-granular  $\gamma'$  precipitation mechanism in titanium alloys was discovered. This novel mechanism involves compositional fluctuations, based on the pseudo-spinodal concept. For a given alloy composition, the decomposition mechanism is strongly temperature dependent which would be expected for homogeneous precipitation via the compositional fluctuation-mediated mechanism but not necessarily for one based on classical nucleation theory. The applicability of this mechanism to phase transformations in general was noted.
- b. Detailed investigation of the  $\gamma'$  -assisted mechanism of intra-granular  $\gamma'$  precipitation in titanium alloys led to some clear insights regarding the role of the precursory  $\gamma'$  precipitates in terms of their compositional and stress influence on  $\gamma'$  nucleation.

**Task E: Evaluation of the oxidation behavior of titanium alloys**

- a. Coupling multiple experimental techniques, the mechanism of a surface oxide layer along with  $\alpha$  precipitation in the subsurface oxygen-enriched zone, during the oxidation of the TIMETAL 21S or  $\beta$ -21S alloy, was developed.
- b. The role of oxygen ingress on the scale and morphology of  $\alpha$  precipitation, and the change in the sub-surface  $\alpha$  and  $\beta$  lattice parameters, has been rationalized.

**Task F: Development of models of nucleation associated with solid-solid phase transformations in titanium and nickel base alloys**

*Nucleation of second phases in Titanium Alloys*

- a. A mixed-model coupled displacive-diffusional mechanism of transformation for isothermal  $\gamma$  precipitation in titanium alloys has been discovered. This task led to direct experimental evidence of the formation of embryonic omega from competing compositional and structural instabilities arising in the body-centered cubic (bcc) lattice of titanium-molybdenum alloys during rapid quenching.

*Nucleation of  $\gamma'$  in Nickel Base Alloys*

- a. The mechanism underlying multiple nucleation bursts leading to the formation of multiple generations (or populations) of  $\gamma'$  precipitates with different size distributions, during the continuous cooling of a commercially used nickel base superalloy was conclusively

established, by coupling direct observation of the multiple nucleation bursts during in situ x-ray diffraction studies in the synchrotron, and characterization of the size distributions associated with the different populations of  $\gamma'$  precipitates by coupling multiple imaging techniques at the appropriate length scale, and detailed compositional analysis of the  $\gamma'$  precipitates as well as the  $\gamma$  matrix using atom probe tomography (APT).

- b. While local compositional equilibrium appears to have been achieved near the  $\gamma'/\gamma$  interface for the first-generation of precipitates, a non-equilibrium long range diffusion profile in the  $\gamma$  matrix is retained during the process of continuous cooling which is largely responsible for the subsequent nucleation bursts at larger undercooling (or lower temperatures) leading to the second and third generations of precipitates.
- c. Under extremely rapid cooling conditions,  $\gamma'$  precipitation occurs under far-from equilibrium conditions. The long-standing controversy due to the competing roles of chemical clustering (or phase separation) and chemical ordering was resolved through the coupled use of aberration-corrected high-resolution scanning transmission electron microscopy and atom probe tomography. Thus, the experimental results, obtained at atomic resolution, can only be interpreted satisfactorily on the basis of phase separation via spinodal decomposition followed by chemical ordering.

**Task G: Growth and coarsening of L1<sub>2</sub> precipitates in new generation Co based alloys**

- a. Detailed coarsening studies on a model ternary Co-10Al-10W(at%) alloy at 800°C and 900°C established that the temporal evolution of average size of the  $\gamma'$  precipitates follows classical matrix diffusion limited LSW coarsening at both temperatures.
- b. The  $\gamma'$  coarsening rate constants have been determined using a modified coarsening rate equation for non-dilute solutions.
- c. Coupling this with the Cahn-Hilliard formulation for interfacial energy, the  $\gamma/\gamma'$  interfacial energies at the respective annealing temperatures have been correlated to the concentration profile across the interface that has been experimentally determined using atom probe tomography (APT). The calculated interfacial energies are comparable with those typically observed in Nickel base superalloys.
- d. For the first time, these coupled experimental-computational approach resulted in the determination of the gradient energy coefficient for  $\gamma/\gamma'$  interfaces in Co-base alloys, a critical input for phase-field and other simulation models for microstructural evolution.

**Task H: Mechanism of nano-scale precipitation in soft magnetic alloys**

- a. The role of the solute elements, copper and niobium, on the different stages of de-vitrification or crystallization of two amorphous soft magnetic alloys, Fe<sub>73.5</sub>Si<sub>13.5</sub>B<sub>9</sub>Nb<sub>3</sub>Cu<sub>1</sub>, also referred to as FINEMET, and a Fe<sub>76.5</sub>Si<sub>13.5</sub>B<sub>9</sub>Cu<sub>1</sub> alloy, a model composition without Nb, was clearly established by coupling atom probe tomography (APT) and transmission electron microscopy (TEM).
- b. Cu clusters forming in the amorphous Fe-Si-B based matrix act as heterogeneous nucleation sites and Nb pile-up at the nanocrystal/amorphous interface acts as a growth retardant during the formation of primary  $\alpha$ -Fe<sub>3</sub>Si nanocrystals.

**Thrust Area III: Three-dimensional (3D) Functionally-graded Hybrid Materials for Aerospace Structural Applications**

## Task A: Metal-Ceramic Hybrids

### Nickel-TiC-Graphite Hybrids

- a. A new class of Ni-Ti-C based metal matrix composites has been developed using the laser engineered net shaping (LENS<sup>TM</sup>) process. These composites consist of an in situ formed and homogeneously distributed titanium carbide (TiC) phase, reinforcing the nickel matrix, together with a third graphitic phase that acts as an in situ repository for solid state lubrication of this hybrid material exhibiting an extremely low coefficient of friction while maintaining a relatively high hardness.
- b. Serial-sectioning followed by three-dimensional reconstruction of the microstructure in these composites, reveals homogeneously distributed primary and eutectic titanium carbide precipitates as well as a graphitic phase encompassing the primary carbides, within the nickel matrix.

## Task B: Ceramic-Ceramic Hybrids

### Ceramic coating infiltrated Carbon-Carbon Composites

- a. Thermodynamically stable protective oxide nanolaminates (ZnO/Al<sub>2</sub>O<sub>3</sub>/ZrO<sub>2</sub>) have been deposited by atomic layer deposition (ALD) to infiltrate porous CCC and graphite foams in order to improve their thermal stability and sliding wear resistance. The results indicate carbothermal reduction to be C driven as CO would be expected to be orders of magnitude faster than C and cause unlocalized diffusion (within the sample pores). Based on the above, carbothermal reduction of zirconia is more dependent on solid-solid reaction than gas-solid reaction, which is in disagreement with previous research findings that suggest carbothermal reduction of zirconia to be only a CO driven reaction mechanism.

## Task C: Metal-Carbon Nanotube Hybrids

### Nickel-Carbon Nanotube (CNT) hybrid materials:

- a. Two novel types of carbon nanotube reinforced nickel (CNT/Ni) nanocomposites were processed, both involving spark plasma sintering (SPS) of precursor powders consisting of nickel and carbon nanotubes. The first type involved simple mechanical dry milling (DM) of nickel and CNT powders, followed by sintering using SPS, resulting in nanocomposites exhibiting a tensile yield strength of 350 MPa (about two times that of SPS processed monolithic nickel with a strength of 160 MPa) and about 30% elongation to failure.
- b. The nanocomposites processed by spark plasma sintering of powders prepared by molecular-level mixing (MLM) exhibited substantially higher tensile yield strength of 690 MPa but limited ductility with a 8% elongation to failure. While the former type of processing involving dry-milling is expected to be lower in cost as well as easy to scale-up, the latter processing technique involving molecular-level mixing leads to a more homogeneous distribution of nanotubes leading to extraordinarily high strength levels.

### Nickel-Graphite Nanoplatelet Hybrid Materials:

- a. Mechanical mixing of nickel (Ni) powders and GNP powders, followed by spark plasma sintering (SPS), has been used to develop a new class of GNP/Ni nanocomposites (or hybrid materials) that exhibit huge enhancements in tensile yield strength while preserving good

ductility. Thus, a Ni-1GNP (1vol.% GNP) nanocomposite exhibited a tensile yield strength of 370 MPa (about 2.5 times of SPS processed monolithic nickel ~ 160 MPa) and an elongation to failure ~ 40%. The enhancement in the tensile strength and ductility of the Ni-1GNP nanocomposite can be attributed to combined effect of homogeneous dispersion of GNPs and grain refinement, the relative influence of each of these effects has been quantitatively assessed in this paper. Additionally, the strong metal-GNP interfacial bonding helps effectively transfer load across the GNP/metal interface during tensile deformation.

## 6. References

Ansara, COST 507: Thermochemical Database for Light Metal Alloys, European Commission, Directorate-General XII, Science, Research and Development, 1995.

Ardell A.J., Ozolins V., *Nature Materials* **4**, 309 (2005).

Ardell A.J.. *Scripta Mater.* 66(2012)423

Ayers J.D., Harris V.G., Sprague J.A., Elam W.T., Jones H.N., *Acta Mater.*, 46 (1998), p. 1861.

Babu S.S., Miller M.K., Vitak J.M., David S.A. *Acta Materialia* 49:4149-4160 (2001)

Babu S.S., Miller M.K., Vitek J.M., David S.A., *Acta Mater.*, 2001; 49: 4149

Balluffi R. W., Allen S. M., Carter W. C., Kinetics of Materials, 1st ed., Wiley-Interscience, 2005.

Banerjee S. and Mukhopadhyay P, Pergamon Press, Oxford, UK (2004).

Behler K., Osswald S., Ye H., Dimovski S., and Gogotsi Y.: *J. Nanopart. Res.* 8(5), 615 (2006). 35.

Bhattacharyya D., Viswanathan G.B., Denkenberger R., Furrer D. and Fraser H.L., *Acta Met* 2003; 4679: 51.

Booth-Morrison C., Mao Z., Noebe R. D. and Seidman D. N., *Appl. Phys. Lett.*, 93 033103-1-033103-3 (2008)

Booth-Morrison C., Weninger J., Sudbrack C., Mao Z., Noebe R., Seidman D.N., *Acta mat.* 56 (2008)3422

Borkar T. and Harimkar S.: *Surf. Eng.* 27, 524 (2011).

Borkar T., Sosa J., Hwang J-Y., Scharf T.W., Tiley J., Fraser H.L., and Banerjee R., 66 (2014) 935

Boyer R., Welsch G. and Collings E.W., “Materials Properties Handbook: Titanium Alloys”, ASM Handbook; 1994.

Boyer R., Welsch G., Collings E.W. (Eds.), Materials Properties Handbook: Titanium Alloys, ASM Intl, Materials Park, OH, 1994

Burgers W. , On the process of transition of the cubic-body-centered modification into the hexagonal-close-packed modification of zirconium, *Physica* 1 (7) (1934) 561—586.

Cahn J.W., Hilliard J.E., *J. Chem. Phys.* 28 (1958) 258.

Cahn J.W., Hilliard J.E., *J. Chem. Phys.* 31 (1959) 688.

Cahn J.W., Hilliard J.E., *J. Chem. Phys.*, 1959; 31: 688

Calderon H.A., Voorhees P.W., Murray J.L., Gkostorz G., *Acta Metall.*, 42, 991(1994)

Cantor, B., and Cahn R. W., 1983, in *Amorphous Metallic Alloys*, edited by F. E. Luborsky (Butterworth, London), p. 487.

Cao W., Chen S.-L., Zhang F., Wu K., Yang Y., Chang Y. A., Schmid-Fetzer R., and Oates W. A., “PANDAT Software with PanEngine, PanOptimizer and PanPrecipitation for Multi-Component Phase Diagram Calculation and Materials Property Simulation”, *CALPHAD: Computer Modeling of Phase Diagrams and Thermochemistry* 2009; 328: 33.

Caron P, *Superalloys 2000*, TMS, Warrendale, PA 737–746.

Cha S., Kim K., Arshad S., Mo C., and Hong S.: *Adv. Mater.* 17, 1377 (2005).

Chaudhari M., Singh A., Gopal P., Nag S., Viswanathan G. B., Tiley J., Banerjee R. and Du J., *Philosophical Magazine Letters*, 1-12(2012)

Chaudhari M., Tiley J., Banerjee R., and Du J., *Modeling and Simulation* 21,055006 (2013)

Chaze A.M., Coddet C., *Journal of Mater. Sci.* 22 1206-1214(1987)

Defense Advanced Research Projects Agency, Defense Sciences Office (DSO), Engine Systems Prognosis, Contract # HR0011-04-C-0001, HR0011-04-C-0002.

Dorner, W., and H. Mehrer, 1991, *Phys. Rev. B* 44, 101

Dupin N, Ansara I, Sundman B (2001) Thermodynamic re-assessment of the ternary system Al-Cr-Ni. *CALPHAD* 25:279-298.

Ferrari A.C.: *Solid State Commun.* 143(1), 47 (2007)

Flinn F.A., *Trans. AIME* 218 (1960) 145

Fontaine D. De and Buck O., *Phil. Mag.*, 27(4), (1973) 967.

Fontaine D. De, *Acta Met.*, 18, (1970) 275.

Fontaine D. De, Paton N.E. and Williams J.C., *Acta Met*, **19** (1971) 1153.

Furuhsara T. , Makino T. , Idei Y. , Ishigaki H. , Takada A. , Maki T. , *Materials transactions - JIM* **39** (1) 31—39(1998)

Gopagoni S., Scharf T., Banerjee R., and Tiley J., U.S. Patent Application 13/769,787 (2013).

Guangjun X., Gaiying Y. and Jing Z., , *Rare Metals* Vol. 18 No. 3(1999)

Hellman O.C., Vandenbroucke J.A., Rusing J., Isheim D., Seidman D.N. (2000), *Microsc Micro-anal* **6**:437-444

Hill S.A. and Ralph B., *Acta Metallurgica*, 1982; **30**: 2219

Hono K., Ping D.H., Ohnuma M., H. Onodera, *Acta mater.*, **47** (1999), p. 997.

Horva' th, J., 1990, in *Diffusion in Solid Metals and Alloys*, Landolt-Bornstein, New Series, Group III, Vol. 26, edited by H. Mehrer (Springer, Berlin), p. 437

Horvath, J., K. Pfahler, W. Ulfert, W. Frank, and H. Mehrer, 1985, *J. Phys.(Paris)* **46**, C8–645

Hwang J.Y., Banerjee R., Tiley J., Srinivassan R., Vishwanathan G.B., Fraser H.L., *Metall. Mater. Trans A* **40**, 24-35 (2009).

Hwang J.Y., Lim B., Tiley J., Banerjee R., and Hong S.: *Carbon* **57**, 282 (2013).

Hwang J.Y., Neira A., Scharf T.W., Tiley J., and Banerjee R.: *Laser-deposited carbon nanotube reinforced nickel matrix composites*. *Scr. Mater.* **59**(5), 487 (2008).

Ikematsu Y. , Doi M. , Miyazaki T. , *Journal of Materials Science* **26** (8) 2071—2075(1991)

Imam M.A. and Feng C.R. , *Advances in the science and technology of titanium alloy processing*, The Minerals, Metals & Materials society, 1997.

Inam F., Yan H., Reece M.J., and Peijs T.: *Adv. Appl. Ceram.* **109**(4), 240 (2010)

Jiang C. and Gleeson B., *Scr. Mater.*, **55** 433-436(2006)

Jiang C., Sordelet D. J. and Gleeson B., *Acta Materialia*, **54** 1147-1154(2006)

Kaufman L. , Nesor H. , *Calphad* **2** (4) 295—318(1978)

Khachaturyan A., *Theory of Structural Transformations in Solids*, John Wiley & Sons, New York, 1983.

Kim K., Eckert J., Menzel S., Gemming T. and Hong S.: *Appl. Phys. Lett.* 92, 121901 (2008).

Krasilnikov N., Lojkowski W., Pakiela Z., and Valiev R.: *Mater. Sci. Eng., A* 397, 330 (2005)

Krueger D.D., Kissinger, R.D. Menzies, C.S. Wukusick, U. S. Patent 4,957,567 (1990).

Krueger, R.D. Kissinger, R.D. Menzies, in *Superalloys 1992*, edited by S.D. Antolovich et al., TMS-AIME, Warrendale, PA, 277 (1992).

Landau L. D. and Lifshitz E. M., *Statistical Physics*, Third Edition, Part 1: 5, 3rd ed. Butterworth-Heinemann; 1980.

Laughlin D.E., *Acta Metallurgica*, 1976; 24: 53.

Li X., Saunders N., Miodownik A.P., *Metall. and Met. Trans A* 33A(2002)

Li Y.G., Blenkinsop P.A., Loretto M.H., Rugg D. and Voice W., *Acta. Mater.*, 47(10), 2889 (1999).

Lifshitz I.M., Slyozov V.V., *J. Phys. Chem. Solids* 19(1961) 35.

Lukas H., Fries S.G. and Sundman B., “Computational Thermodynamics: The Calphad Method”, Cambridge University Press; 2007.

Malinov S., *Materials characterization* 48 (2002) 279-295

McLean D, *Metal Sci* 1984;18:249.

Meher S., Yan H.Y., Nag S., Dye D. Banerjee R., *Scripta Mater.* 67(2012)850

Menon E.K., Aaronson H.I., *Acta Metall.*, 34 (1986), pp. 1963–1973

Menon E.S.K. and Aaronson H.I., *Acta Metall.* 1963: 34(1986).

Mishin Y, *Acta Mater.* **52**, 1451 (2004).

Mohseni H. and Scharf T.W., *Journal of Vacuum Science and Technology A*, **30**(1) 01A149-1 - 01A149-12 (2012).

Murray J. L. (ed.), *Phase Diagrams of Binary Titanium Alloys*, ASM Intl, 1987

Nag S. , Zheng Y. , Williams R. , Devaraj A. , Boyne A. , Wang Y. , Collins P. , Viswanathan G.W., Tiley J. , Muddle B. , Banerjee R. , Fraser H. L., *Acta Mat.* 60, 6247 (2012)

Ni Y. and Khachaturyan A.G., "From chessboard tweed to chessboard nanowire structure during pseudospinodal decomposition", *Nature Materials* ,410,8(2009)

Ni Y. and Khachaturyan A.G., *Acta Met.* 4498, 56(2008)

Payton E.J., Phillips P.J., Mills M.J. *Materials Science and Engineering A* 527:2684-2692(2010)

Plapp M. , *Philosophical Magazine* 91 (1) 25—44(2010)

Porter D.A. and Easterling K.E., "Phase Transformations in Metals and Alloys", Chapman and Hall 1981; 268.

Prasad R. , Greer A. , *Journal of Alloys and Compounds* 194 (2) 263—272(1993)

Radis R., Schaff er M., Albu M, Kothleitner G., Polt P., Kozeschnik E., *Acta Mater.* 2009; 57: 5739.

Radis R., Schaffer M., Albu M., Kothleitner G., Polt P., Kozeschnik E. (2009) *Acta Materialia* 57: 5739-5747.

Ravi R., Paul A., *Intermetallics* 19 (2011) 426

Rogers T. M., Elder K. R., Desai R. C., *Physical Review B* 37 (16) (1988) 9638—9649.

Santhy K. , Hari Kumar K. , *Intermetallics* 18 (9) 1713—1721(2010)

Sarosi P. M., Viswanathan G. B., Whitis D., and, Mills M. J., *Ultramicroscopy*, 103, 83 (2005).

Sarosi P.M. Wang B., Simmons J.P., Wang Y., and, Mills M.J., *Scripta Mater.*, 2007; 57: 767.

Sarosi P.M., Viswanathan G.B., Whitis D., and, Mills M.J., *Ultramicroscopy*, 2005; 103: 83.

Sato J., Omori T., Oikawa K., Ohnuma I. , Kainuma R., Ishida K. , *Science* 312 (2006) 90.

Saunders N (1996) Phase diagram calculations for Ni-based superalloys. *Proc Int Symp Super* 101-110.

Scharf T.W., Mohseni H., and Tiley J.. US Patent: "Anti-fretting Wear Coating for Substrates," Patent Number US 9,228,145. Date of Patent January 5, 2016.

Shim J. , Oh C. , Lee D. , *Metallurgical and Materials Transactions B* 27 (6) 955—966(1996)

Shim J. H., Oh C. S. and Lee D.N., *Met. Mat. Trans. B* 1996; 955: 27.

Simmons J. P., Shen C. , Wang Y. , *Scripta materialia* 43 (10) 935—942 (2000)

Singh A.R.P., Nag S., Hwang J.Y., Viswanathan G.B., Tiley J., Srinivasan R., Fraser H.L. and Banerjee R., Mater. Char., 2011; 62(9): 878.

Soffa W.A. and Laughlin D.E., Acta Metallurgica, 1989; 37: 3019

Sondhi, C. Morandi, R.F. Reidy, and T.W. Scharf, Ceramics International **39**, 4489–4497 (2013).

Sondhi, O. Okobiah, S. Chattopadhyay, T. Shibata, T.W. Scharf, R. F. Reidy, **47**, 1512 (2014).

Suzuki A. , Pollock TM, Acta Mater. 56 (2008) 1288

Tiley J., Srinivasan R., Banerjee R., Viswanathan G.B., Toby B. and Fraser H.L., Mat. Sci. Tech., 2009; 25(11): 1369.

Tiley J., Viswanathan G.B., Srinivasan R, Banerjee R, Fraser HL, Acta Mat. 57(2009) 2538

Titus M., Suzuki A., Pollock T.M., Scripta Mater. 66 (2012) 574

Tuinstra F. and Koenig J.L.: Raman spectrum of graphite. J. Chem. Phys. 53, 1126 (1970).

Uchic M.D., Groeber M., Dimiduk D., and J.P. Simmons, Scr. Mater. 55, 23 (2006).

Vaithyanathan V., Chen L.Q., Acta Mat. 50 (2002) 4061

Viswanathan G.B., Banerjee R., Singh A. Nag S., Tiley J., and Fraser H.L., Scripta Mater, 2011; 65: 485.

Wagner C., Z. Elektrochem. 65 (1961) 581.

Wallace T.A., Wiedemann K.E. and Clark R.K., Titanium 92, Science and Technology, 1993.

Wang Y.J., Wang C.Y., Appl. Phys. Lett. 94 (2009) 261909.

Wen Y.H., Simmons J.P., Shen C., Woodward C., and, Wang Y., Acta Mater., 2003; 51: 1123.

Wen Y.H., Simmons J.P., Shen C., Woodward C., Wang Y., Acta Materialia 51:1123-1132(2003)

Wen Y.H., Simmons J.P., Shen C., Woodward C., and, Wang Y., Acta Mater., 2003; 51: 1123.

Wen Y.H., Wang B., Simmons J.P., and, Wang Y., Acta Mater., 2006; 54: 2087.

Wen Y.H., Wang B., Simmons J.P., Wang Y. Acta Materialia 54:2087-2099(2006)

Williams J.C., Fontaine D. De and Patton N.E., Metall. Trans. A, **4** (1973) 2701

Wlodek S.T., Kelly M., Alden D.A., in Superalloys 1996, edited by R.D. Kissinger, et al, TMS, Warrendale, PA, 129-136 (1996).

Wu Q. and Li S., Computational Materials Science, 53 436-443(2012)

Yan H.Y., Vorontsov V.A., Coakley J., Jones N.G., Stone H.J., Dye D., Superalloys 2012, 705

Yoo Y.S., Yoon D.Y., Hery M.F., metals and mat. 1(1995), 47

Zhang Y.R., Ramanujan R.V., Journal of Alloys and Compounds, 403 (2005), pp. 197-205.

## LIST OF ACRONYMS, ABBREVIATIONS, AND SYMBOLS

3DAP	Three-dimensional atom probe
ALD	Atomic layer deposition
APT	Atom probe tomography
AFRL	Air Force Research Laboratory
BSED	Back-scattered electron detection
CART	Center for Advanced Research and Technology
CASCaM	Center for Advanced Scientific Computing and Modeling
CCC	Carbon-carbon composites
CNT/Ni	Carbon nanotube reinforced nickel
DOD	Department of Defense
DFT	Density functional theory
ECAP	Equal channel angular pressing
EFTEM	Energy-filtered transmission electron microscopy
FIB	Focused ion beam
GGA	Generalized gradient approximation
GNP	Graphite nanoplatelets
HAADF	High Angle Annular Dark Field
HRSTEM	High resolution scanning transmission electron microscopy
ISES	Institute for Science and Engineering Simulation
LENS	Laser engineered net shaping
LSW	Lifshitz, Slyozov and Wagner (model)
MIPAR	Materials Image Processing and Automated Reconstruction
MLM	Molecular-level mixing
OSU	Ohio State University
PAW	Projected Augmented Wave
PBE	Perdew-Burke-Ernzerhof
RXCM	Metals Branch, Structural Materials Division, Materials and Manufacturing Directorate
SE	Secondary electron
SEM	Scanning electron microscopy
SPS	Spark plasma sintering
TIDC	Trans-interface diffusion controlled
UFG	Ultra-fine grained
UNT	University of North Texas
VASP	Vienna ab initio Simulation Package
WPAFB	Wright-Patterson Air Force Base
XRD	X-ray diffraction
YSZ	Yttria-stabilized zirconia

All other acronyms, abbreviations and symbols have been defined in the portion of “results and discussion” where they are used.

